APPLICATION OF DIAMOND THIN-FILM ELECTRODES FOR THE ELECTROCHEMICAL DETECTION OF TRACE METAL IONS

By

Prerna Virendra Sonthalia

A DISSERTATION

Submitted to
Michigan State University
in partial fulfillment of the requirements
for the degree of

DOCTOR OF PHILOSOPHY

Department of Chemistry

2004

ABSTRACT

APPLICATION OF DIAMOND THIN-FILM ELECTRODES FOR THE ELECTROCHEMICAL DETECTION OF TRACE METAL IONS

By

Prerna Virendra Sonthalia

Determination of trace metal ion contamination using anodic stripping voltammetry (ASV) is an established method. The use of boron-doped diamond (BDD) thin-film electrodes as alternates to Hg based electrodes for use in ASV was investigated. This is mainly because of the toxicity of Hg. High-quality conductive diamond is attractive for the detection of trace metal ions due to the material's (i) wide working potential window, (ii) stable surface chemistry and microstructure, (iii) chemically inert surface, and (iv) good activity for metal deposition and stripping reactions. The application of boron-doped microcrystalline and nanocrystalline diamond thin-film electrodes for the analysis of Ag(I), Cu(II), Pb(II), Cd(II), and Zn(II) yielded analytical detection figures of merit comparable and better than those obtained for Hg-coated GC and bare GC, respectively. Limits of quantitation in the low ppb range, good sensitivity, excellent response precision (< 4 %) and long-term stability (> 96 %) were obtained.

Nanocrystalline diamond has been found to perform slightly better than the more conventional microcrystalline form of diamond in this application. It was used in conjunction with differential pulse voltammetry (DPASV) to detect these metal ions in lake water, well water, tap water, wastewater treatment sludge, and soil. The electrochemical results were comparable (< 10% difference in most cases) with data from

inductively coupled plasma mass spectrometric (ICP-MS) and or atomic absorption spectrometric (AAS) measurements of the same samples.

A research goal was to determine how factors such as the diamond surface morphology and chemistry affected the nucleation and growth of metal phases. Scanning electron micrographs of the metal deposits are presented. In general, the fraction of the surface area of the diamond covered by metal deposits was larger for nanocrystalline diamond. This indicates that a larger amount of metal phase formation occurs on nanocrystalline diamond during the preconcentration step, yielding greater sensitivity and lower limits of quantitation in the DPASV measurements.

The quality of the DPASV measurement could be improved if the relatively large peak widths seen in most of our presented data were reduced. We demonstrate the use of pulsed galvanostatic deposition to produce Cu deposits that are nominally smaller in size and more uniformly dispersed over the diamond surface than what is achieved using constant potential or constant current. This in turn leads to relatively sharp and narrow stripping peaks at 40% of the effective deposition time. We also found a possibility of intermetallic formation between Cu and Zn during their simultaneous measurement on diamond. Initial results from the investigation of pulsed galvanostatic deposition as a means to reduce the intermetallic complex formation of the Cu-Zn compound proved promising. The hypothesis was that if the probability of a physical/chemical interaction of the surface ad-atoms were reduced, it would help reduce intermetallic complex formation.

ACKNOWLEDGEMENTS

I would like to begin by thanking a man whose influence on my life is just beginning. He is my adviser Dr. Greg Swain. His guidance, patience and support have seen me through to this day. I deeply admire his personality, character, love for science and value for family life. There was never a time in these four years that I have known him when I could not approach him with an idea or a problem. His ability for hard work, quest for excellence, vast knowledge of analytical chemistry, patience, attention to detail and congenial nature amazes me. Thank you Greg!

I would like to thank my committee members – Dr. Simon Garrett, Dr. Vicki Mcguffin, Dr. Merlin Bruening and Dr. Dave Long. Their input and support has been valuable to my development as a scientist. I am very grateful to Dr. Kathy Severin, she has been my mentor and through her own example inspired me to make contributions to science outreach. Appreciation is also due to Ewa Danielewicz (SEM facility) and Dr. Lina Patino (ICP-MS facility) who helped a great deal in my research efforts.

The Swain group has been like an extended family. Dr. Jian Wang, Dr. Malgorzata Witek, Dr. Mateuz Hupert and Dr. Shannon Haymond welcomed me into the group, I got to learn a great deal from them. Visiting post-docs and scholars Dr. Josef Cvačka, Zuzana Cvačková, Veronika Quaiserová, Karolina Pecková, Dr. Jesse Seegmiller and Dr. Yoshiyuki Show added a lot to my understanding of science. I thank them all for their friendships and their contribution. Dr. Yoshiyuki Show's help with all the diamond film growth and his advice is deeply appreciated. Jason Stotter and Grace Muna, who joined the group the same year as me shared my pains and joys. Graces "go girl" always helped me to carry on. Sanjeev Dalavoy, Jinwoo Park, Anne Fischer "Fish",

Gloria Pimienta, Doug Knigge, Jason Bennett "JB", Audrey Martin, Shihua Wang, Yang Song, Pushwinder Kaur and Elizabeth McGaw have been very supportive. Thanks guys! Elizabeth McGaw has collected some of the data presented in this thesis. I thank her for all her help and wish her lots of success with the project. JB developed the pulse deposition setup, thanks JB! JB and Fish also helped with the rehydrogenation of the diamond thin-films. Jesse Seegmiller and Shihua Wang assisted in the SECM work. As I fly the "nest" I cannot help but feel a sense of sorrow at leaving the company of all these wonderful people.

My family has been a constant source of encouragement, their sacrifices and love cannot be emphasized enough. My grandmother who literally let go in her words her "walking stick," when she so selflessly supported my decision to undertake higher education. My mother who silently suffered great hardships to see her children succeed. My father who is a scientist at heart, although not one of his "inventions" has seen the light of day! I would like to thank my brother Aayush and bhabhi Rakhee for their unconditional love and support. I also thank mamaji and mamiji my "home away from home" here in Lansing. I thank my friend Amit Goradia for his encouragement. I also thank Lavanya Parthasarathy, Kiran Misra, Freddy Kharoliwala, Bhaskar Patham, Priya Heerwani and all the others for their support.

Funding from the U.S. Department of Agriculture (2001-35102-10045) and NASA (NA69-1481; Advanced Environmental Monitoring and Control) is gratefully acknowledged.

TABLE OF CONTENTS

THIN-FILM ELECTRODES AND SOME COMMONLY USED ELECTRODE MATERIALS

CHAPTER 5
TRACE METAL ANALYSIS IN CONTAMINATED WATER SAMPLES USING ANODIC STRIPPING VOLTAMMETRY AND A NANOCRYSTALLINE DIAMOND THIN-FILM ELECTRODE

CHAPTER 6
CHALLENGES AND SOLUTIONS: TOWARDS GAINING BETTER SELECTIVITY AND RESOLUTION DURING THE ANODIC STRIPPING VOLTAMMETRY OF METAL IONS USING BORON-DOPED DIAMOND THIN-FILM ELECTRODES

CHAPTER 7

LIST OF TABLES

LIST OF FIGURES

CHAPTER 1

INTRODUCTION

There is an increasing demand for the development of sensitive, reproducible, low-cost, and field-deployable methods for the detection of trace metal ions in water supplies. Determination of trace metal ion contamination in the environment using anodic stripping voltammetry (ASV) has all the above listed advantages. ASV involves a two step measurement: preconcentration or metal deposition followed by an anodic potential scan to selectively oxidize each deposited metal phase. Historically, Hg drop (HMDE) and Hg-film-coated (MFE) electrodes have been used in ASV; however, there is a need to develop Hg-free "alternate" electrodes. This is mainly because of the toxicity of Hg. The use of boron-doped diamond (BDD) thin-film electrode as an alternate to Hg for this application is the focus of this work.

Diamond thin-film electrode shows promise for this electroanalytical application, as the material possesses many of the same attributes as Hg. For example, high-quality diamond exhibits (i) large overpotentials for hydrogen evolution and oxygen reduction, (ii) a large overpotential for oxygen evolution (large positive window), (iii) low background current, (iv) resistance to electrode fouling, (v) rapid electrode reaction kinetics for metal deposition and stripping reactions, and (vi) no chemical interaction with metal deposits. Diamond consists of an sp^3-bonded carbon network. Its structural robustness and chemical inertness result from high atomic density and strong, directional covalent bonding.[1]

The unique properties of boron-doped diamond make it ideally suited for ASV, as our group has demonstrated for Ag(I), Cu(II), Pb(II), Cd(II) and Zn(II).[2-4] Work in our laboratory has helped to establish the feasibility of electrodepositing metal phases on diamond surfaces.[5,6] Diamond electrodes provide improvements over other alternate electrodes, in terms of several electroanalytical features of merit: linear dynamic range, sensitivity, detection limit, response variability and response stability.

This research sought to answer several key questions.

1. Is diamond a viable electrode material for trace metal ion analysis?

2. How does the performance of microcrystalline and nanocrystalline diamond thin-films compare, given their differences in surface morphology and microstructure, for the detection of several priority metal ions? What type of analytical detection figures of merit are possible for real and simulated contaminated water samples?

3. How do factors, such as the diamond surface morphology and chemistry, affect the nucleation and growth of metal phases? Where do the metal phases form on the surface and what particle size and distribution do they possess?

4. Is intermetallic compound formation on diamond a major issue and, if so, can formation be minimized through the use of pulsed galvanostatic deposition rather than conventional constant potential or current deposition?

1.1 The Need for Monitoring Metal Ions

Metals differ from other toxic substances in that they are neither created nor destroyed by humans. Their utilization has ramifications for human health in at least two major ways: anthropogenic contributions to air, water, soil and food, and altering the speciation or biochemical form of the element.[7]

Accurate determination of metal ion concentrations in water supplies is critical because of their potential for causing adverse health effects in humans.[8] An interference of the metal contaminant with an essential metal may occur when the metabolism of the two are similar.[9] For instance, Pb(II) competes with Ca(II) in several ways: (i) inhibiting the release of neurotransmitters and interfering with the regulation of cell metabolism by binding to second-messenger calcium receptors, (ii) blocking ion transport by calcium channels and calcium-sodium ATP pumps, and (iii) by competing for calcium-binding protein sites and uptake by mitochondria. Dietary deficiencies of Ca(II), Fe(II)/(III) and Zn(II) enhance the effects of Pb(II) on cognitive and behavioral development. Iron deficiency increases the gastrointestinal absorption of cadmium, and cadmium competes with zinc for binding sites on metallothionein, which is important in the storage and transport of zinc during development. The EPA regulates the maximum allowed levels of these metals in potable water (National Primary Drinking Water Standards: Cd – 5 ppb, Cu – 1.3 ppm, Pb- 15 ppb; Secondary Maximum Contaminant Levels: Ag – 100 ppb, Zn –5 ppm). Therefore, they are analytes of importance.[10]

The toxicity of a particular metal depends on several factors with the important ones listed in Table 1.1.[11] A critical determinant of metal retention is its biological half-life, that is, the time it takes for the body or organ to excrete half of an accumulated amount. The half-life varies according to the metal as well as the organ or tissue. For example, the biological half-lives of Cd(II) in the kidney and Pb(II) in bone are 20 to 30 years, in contrast to As(III, IV) or Li(I) which are only a few hours or days.[11] This means that some metal ions have a tendency to bio-accumulate in specific organs of the human body.

Table 1.1 Factors affecting the toxicity of metals

Interactions with essential metals
Formation of metal-protein complexes
Age and stage of development of the person
Lifestyle factors
Chemical form or speciation of the metal ion
Immune status of the host

A brief review of the sources, degree of toxicity and exposure routes of these five priority ions (Ag(I), Cu(II), Cd(II), Pb(II) and Zn(II)) is given below.[11]

Ag (Ag(I)): The principal use of Ag is as a halide in the manufacture of photographic plates. Other uses are for jewelry, coins and eating utensils. Ag salts are known to have medicinal uses as antiseptics and astringents. Ag compounds can be absorbed orally, by inhalation, and through damaged skin. The major effect of excessive absorption of Ag(I) is local or generalized impregnation of the tissues, where it remains as silver sulfide. This forms an insoluble complex in elastic fibers, resulting in agyria. Chronic bronchitis has also been reported to result from medicinal use of colloidal Ag.

Cu (Cu(II)): Cu is widely distributed in nature and is a nutritionally essential element. Ambient air levels are generally low in the United States. For the general population, food, beverages, and drinking water are potential sources of excess exposure. Experimental studies in humans suggested that ingestion of drinking water greater than 3 ppm of Cu produced gastrointestinal symptoms including nausea, vomiting and diarrhea. Ingestion of large amounts of Cu salts, most frequently $CuSO_4$, could result in hepatic necrosis and death.

Cd (Cd(II)): A modern toxic metal. It was discovered as an element only in 1817, however, it has many current applications. Because of its non-corrosive properties, its main use is in electroplating or galvanizing. It is also used as a color pigment for paints and batteries and as a cathode material for nickel-cadmium batteries. Cd is a by-product of Zn and Pb mining and smelting, which are important sources of environmental pollution. For the general population, the major source of Cd is food. Gastrointestinal absorption of Cd(II) is about 5 to 8 percent. A major non-occupational source of respirable Cd(II) is cigarettes, although workplace exposure to Cd(II) has been known to be particularly hazardous.

Pb (Pb(II)): Pb is toxic to most living things at high exposure levels and there is no demonstrated biological need for it. The major risk is toxicity to the nervous system and the most susceptible populations are children. The principle route of exposure for people in the general population is food. Other sources include Pb-based indoor paint, Pb(II) in air from combustion of lead containing industrial emissions and Pb(II) in contaminated water.

Zinc (Zn(II)): Zn is a nutritionally essential metal, and a deficiency results in severe health consequences. More than 200 metalloenzymes require Zn as a cofactor. Adverse health effects from excessive exposure to Zn(II) are relatively uncommon, but gastrointestinal distress and diarrhea have been reported following ingestion of beverages standing in galvanized cans or from the use of galvanized utensils. With regard to industrial exposure, metal fume fever resulting from inhalation of freshly formed fumes of Zn(II) presents the most significant effect.

1.2 The Differential Pulse Anodic Stripping Voltammetry (DPASV) Technique

Several analytical techniques are routinely used for the detection of heavy metal ions including atomic absorption, plasma emission, x-ray fluorescence spectroscopy, anodic stripping voltammetry (ASV), and neutron activation.[12] However, none of these methods offer all the advantages of ASV. Voltammetry refers to a class of electroanalytical techniques in which the current at a working electrode is measured as a function of a potential waveform applied to the it.[12] The working electrode is the electrode at which the reaction of interest occurs. ASV is a type of voltammetric technique that utilizes a bulk electrolytic step to preconcentrate the analyte from the sample solution into or onto the working electrode. The preconcentration step, which can be thought of as an electrochemical extraction step, yields very favorable signal-to-noise ratios of the recorded voltammetric i-E curves. In fact, the detection limits are lowered by 2 to 3 orders compared to solution-phase voltammetric measurements.[13] In summary, ASV is a sensitive detection method for many metal ions and possesses multielement analysis capability, low instrumental and maintenance costs, field deployability and low power demand with no need for cooling and or ventilation.[12]

As depicted pictorially in Figure 1.1, ASV involves a two-step measurement sequence: (i) electroreduction of the metal ions at a negative potential to form metal phases on the electrode surface (the preconcentrating step), and (ii) electrooxidation of each metal during a slow potential scan toward positive potentials (the stripping step). In theory, each metal is selectively oxidized near its standard reduction potential, $E^{o'}$, and the oxidation current or charge is recorded and used for quantitative purposes. One voltammetric method commonly used is differential pulse voltammetry. In this method, a series of pulses of equal amplitude are superimposed on a potential ramp. As shown in Figure 1.1, each pulse has parameters of amplitude, width, period and step height that can be controlled to increase the magnitude of the current. The currents are sampled twice, once just prior to the pulse application and again at the end of the pulse period. The first measured current is subtracted from the second one and the current difference is plotted versus potential. The technique is useful for discriminating the faradaic current from the background current. When the potential pulse is applied, the total current in the system increases because of the resultant increase in both the faradaic and double layer charging currents. The charging current decays rapidly in comparison to the diffusion-controlled faradaic current ($i_c \sim e^{-t/R_uC_d}$ versus $i_f \sim t^{-1/2}$, where t is the time (s), R_u the uncompensated solution resistance (Ω) and C_d the double layer capacitance (F)).

Some researchers are also of the opinion that an overall improvement in the signal-to-background ratio occurs because some of the metal ions that are stripped off from the electrode surface during the application of the pulse are replated onto the electrode during the waiting time between pulses.[12] The use of the differential pulse voltammetry with a Hg thin-film deposited on glassy carbon (GC) gave detection limits 3-5 times lower than those achieved with linear scan voltammetry.[14] The same authors noted that the differential pulse peak currents are more susceptible to interference by surface-active substances than linear scan measurements, with undetected absorption effects causing greater errors.[14] This can be explained by the fact that potential step-based techniques tend to depend heavily on the electron-transfer rate constant of the reaction.[15] If the system has slow charge-transfer kinetics (high activation energy) for the reaction of interest, contaminants in solution would manifest themselves in the voltammetric i-E curves.

Two small-amplitude controlled-potential techniques, differential pulse voltammetry and square-wave voltammetry have been tested for use in the stripping step. Square-wave voltammetry is a differential technique in which a waveform composed of a symmetrical square-wave is superimposed on a base staircase potential. Although both techniques yielded very favorable signal-to-background ratios, the peak widths of the voltammetric i-E curves in the differential pulse method were narrower. An advantage of the differential pulse method is the improved resolution between two species with similar redox potentials due to its peak-shaped response. In various situations, peaks separated by only 50 mV could be measured.[13]

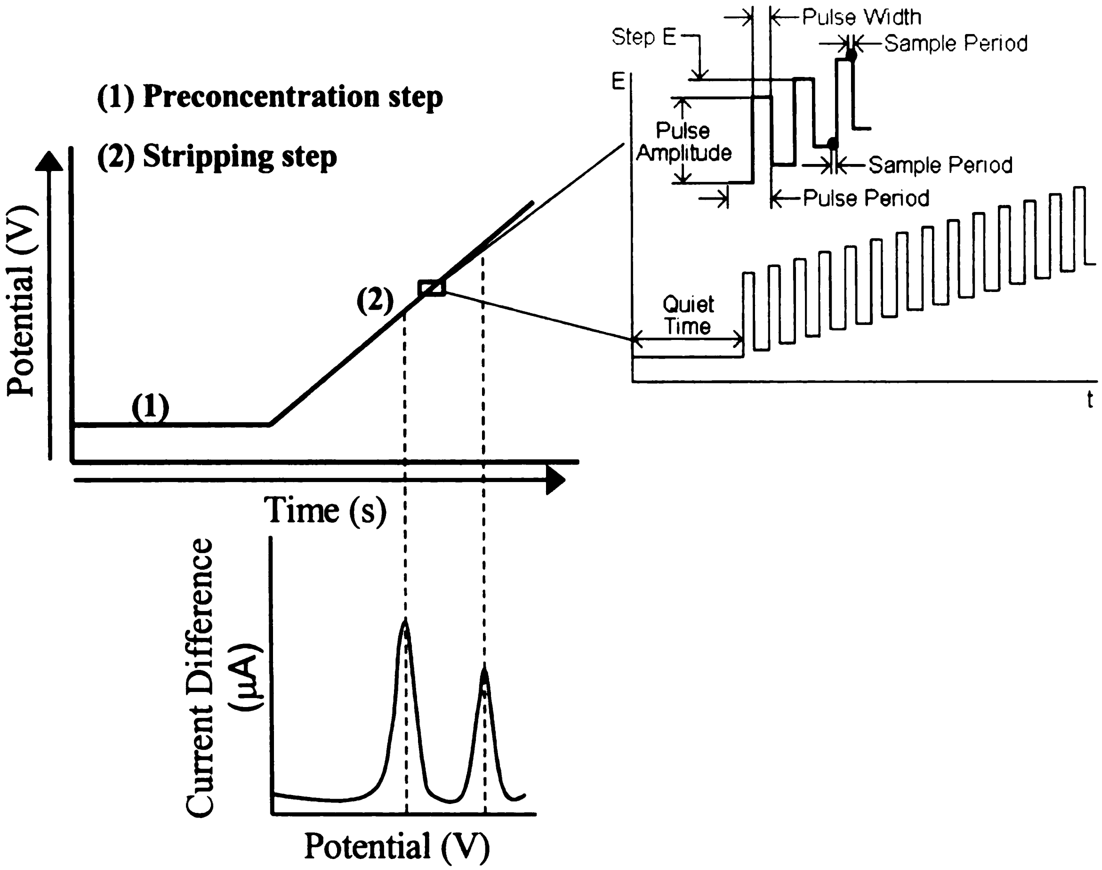

Figure 1.1 The differential pulse anodic stripping voltammetric (DPASV) potential waveform and resulting current response. (1) The preconcentration step involves a cathodic potential-step of some magnitude and duration and (2) the oxidation step involves a potential scan in the positive direction to selectively oxidize each metal phase formed. An enlarged view of the applied pulse program depicting the various parameters is shown to the right. The resulting voltammetric i-E curve is constructed by plotting the current difference for each pulse as a function of the potential.

Several researchers such as R.L. Birke, R.A. Osteryoung, J. Osteryoung, K.W. Hanck and K.B. Oldham developed the theory of differential pulse voltammetry in the period from the mid-1960s to late 1970s.[16-22] However, the concept of pulse polarography was originally developed in England by G.C. Barker as an out-growth of his work on square wave polarography.[23, 24] The equation representing the maximum current difference (Δi_{max}) obtained is given by:[21]

$$\Delta i_{max} = \frac{n^2 F^2 \Delta E A Do^{1/2} Co}{4RT\pi^{1/2} t^{1/2}} \tag{1.1}$$

Δi is the difference in current (A) recorded at potentials E_1 and E_2, C_o is the concentration of the reactant (mol/cm^3), t is the step width (s), D_o is the diffusion coefficient (cm^2/s), A is the area of the electrode (cm^2), F is the Faraday constant (C/mol e$^-$), R is the gas constant (Jmol^{-1}K^{-1}) and n is the stoichiometric number of electrons involved in the electrode reaction (mol e$^-$). The above expression however applies when the pulse amplitude ΔE (V), $\Delta E = E_2 - E_1$, is smaller than RT/nF. When a large pulse is used, the expression for the maximum current becomes:

$$\Delta i_{max} = \frac{nFACoDo^{1/2}(\sigma - 1)}{\pi^{1/2} t^{1/2}(\sigma + 1)} \tag{1.2}$$

$$\text{and, } \sigma = \exp\left(\frac{E_2 - E_1}{2} - E_{1/2}\right)\frac{nF}{RT} \tag{1.3}$$

When $\Delta E/2$ becomes very large with respect to RT/nF, equation 1.3 is simply the Cottrell equation. The above expressions should apply for the case of planar solid electrodes because the effect of electrode sphericity or capillary parameters in case of the HMDE has not been taken into consideration. The expressions hold for mass-transfer limited conditions.

To determine the effect of pulse amplitude on peak height, the term $(\sigma-1)/(\sigma+1)$ can be evaluated at various pulse amplitudes and for various values of n. This term is unity at maximum height and the values obtained represent the fraction of maximum peak height under the conditions listed. Although, increasing the pulse amplitude would give increased sensitivity of the measurements, it would also result in decreased resolution.

Barker also gives an expression for peak half width, $W_{1/2}$

$$W_{1/2} = 3.52 \frac{RT}{nF} \tag{1.4}$$

Again, this expression is valid only for small pulse amplitudes. The equation gives peak half widths of 90.4, 45.2 and 30.1 mV, for 1, 2 and 3 electrons, respectively.

To derive the expression for half width, which is valid for any pulse amplitude, the terms P and A are derived:

$$P^2 + P\frac{(A^3+3A^2-3A-1)}{(A-A^2)} + 1 = 0 \tag{1.5}$$

$$\text{Where, } A = \exp\frac{\Delta E}{2}\left(\frac{nF}{RT}\right) \tag{1.6}$$

$$\text{Also, } P = \exp\left(\frac{E_1+E_2}{2} - E_{1/2}\right)\frac{nF}{RT} \tag{1.7}$$

From P, two values of E are obtained and the difference between these values gives the peak half width.

In summary, the selection of the pulse amplitude and potential scan rate usually involves a trade-off among sensitivity, resolution, and speed.[13] Our initial efforts with the project involved the optimization of the differential pulse parameters to yield the maximum analytical signal.

1.3 "Alternate" Electrodes and Their Limitations

Historically, Hg drop (HMDE) and Hg film-coated (MFE) electrodes have been used in ASV. However, there is much interest in finding non-toxic, "alternate" electrodes that function as well as Hg does.[25, 26] Hg can exist in three forms: elemental, inorganic and organic. All three forms are toxic, however, their biological uptake mechanisms are different. Hg in forms such as methyl mercury is extremely toxic and mainly affects the central nervous system (CNS). Elemental Hg readily passes across the blood-brain barrier into the central nervous system and also into the fetus. Mercuric chloride salts ($HgCl_2$ and Hg_2Cl_2) are known to cause corrosive ulceration, bleeding and necrosis of the gastrointestinal tract accompanied by shock and circulatory collapse.

There are also other reasons for seeking alternate electrodes. Hg cannot be used for the detection of metal ions having more positive standard reduction potentials than it (e.g., Ag(I) and Au(II)) or which are insoluble in it (e.g., As(III)).[26] Hg is a fine electrode material for ASV because the liquid environment provides a medium into which the deposited metals can dissolve and form amalgams. The oxidation of a metal ion from its amalgam is a much better understood and easily controlled process than the metal nucleation and growth and subsequent oxidation from solid electrode surfaces. Relatively intense and narrow peak currents are normally seen for the oxidation of metal ions from amalgams. There seems to be minimal interference between co-deposited metals whereas it is still an open challenge to get the same/better response from solid electrodes. A comparison of the properties of Hg-based electrodes and diamond, pertinent to their use in ASV detection of trace metal ions, is given in Table 1.2. Clearly, diamond possesses many of the same attributes as Hg.

Table 1.2 Characteristics and attributes of Hg and diamond electrodes for ASV.

Hg-based electrodes	Diamond electrodes
Potential window limited by self-oxidation in the positive range (~ -1.2 V to 0.2 V)	Large working potential window (~ -1.2 V to 1.5 V)
Surface can be renewed by depositing a fresh film of Hg	Surface is stable with no need for renewal
Uniform surface, stripping peaks are narrow	Surface of heterogeneous conductivity and microstructure, leads to broader peaks
Cannot be used for the stripping analysis of metals with relatively positive $E^{o'}$ values (e.g., Au, Hg) or for metals insoluble in Hg (e.g., As)	Can be used for the assay of metal ions having relatively positive $E^{o'}$ values.
Highly toxic, volatile and unstable	Non-toxic and chemically inert
Foreign metals deposit within the Hg volume forming their amalgams	Foreign metals deposit as a solid phase, dependent on electrode surface morphology and microstructure
Higher background currents	Very low background currents
Formation of intermetallic compounds is reduced due to low surface area to volume ratio of the Hg drops	Methods such as pulsed deposition are being researched to yield low surface area to volume ratio of metal deposits

Proper choice of the working electrode is crucial for the success of any ASV measurement. The ideal electrode must meet the requirements of high electrical conductivity, electrochemical inertness over the potential region of interest and chemical inertness. Alternate electrodes being investigated are Ir[26], Bi[27], Au[28], Ag[29] and graphite[30]. However, the overall response of most of these alternates has not approached that of Hg. Some of the reasons for this include the heterogeneous surface structure of solid electrodes and the higher background current compared to Hg electrodes.[6,7] Alternate electrodes like "noble" metals[31] and glassy carbon, can be intrinsically limited in terms of sensitivity because of surface oxidation and reduction processes.

The practical utility of any electrode is determined by its effectiveness at determining metal ions in real water samples. Kounaves et al. reported on the use of microfabricated Au ultra-microelectrode arrays for the on-site analysis of As(III) in groundwater.[28] Limits of detection were investigated, and 0.05 ppb As(III) could be measured while maintaining a S/N of 3/1. The same group reported on the use of a microfabricated array of Ir micro-disks for Cu(II) analysis in tap and spring water samples, and good agreement was obtained with conventional methods.[26] An unexplained effect of Cl^- on the Ir surface was noted. Further investigation by atomic force microscopy revealed that changes on the surface occurred but could be eliminated when Cl^- leakage from the reference electrode was minimized. Wang and coworkers reported the use of Bi-coated, screen-printed carbon electrodes for ASV.[32] These electrodes were successfully used for the determination of Pb(II) in drinking water samples.[32] Of all the possible "alternate" electrodes, Bi appears to exhibit performance closest to that of Hg, and it is environmentally friendly. However, the potential window of Bi is between -1.2 and -0.2 V vs. Ag/AgCl, and this limits its usefulness to the determination of metal ions with standard potentials more negative than – 0.2 V.

Carbon electrodes have also been investigated for ASV. Recently, the simultaneous determination of Cd(II) and Pb(II) at a glassy carbon electrode modified with multi-wall carbon nanotubes was reported.[33] Compared with bare glassy carbon, the modified electrode exhibited improved sensitivity for these metal ions. A reason for this observation could be the fact that multi-walled carbon nanotubes are chemically stable and possess excellent electrical conductivity.[34] The linear dynamic range for the detection of Cd(II) and Pb(II) was reported to be from 2.5×10^{-8} to 1×10^{-5} M (2.8 ppb to 1.1 ppm) and from 2×10^{-8} to 1×10^{-5} M (4.1 ppb to 2.1 ppm), respectively, for deposition or preconcentration times of 5 minutes.

1.4 Diamond Thin-Film as an "Alternate" Electrode

As will be shown in this dissertation, electrically conducting diamond is an electrode material that shows great promise for application in ASV. Diamond is normally a superb electrical insulator, but when doped with boron, the material possesses semi-metallic electronic properties.[1] For example, a doping level of $\sim 10^{20}$ cm^{-3} results in an in-plane resistivity of ca. 0.01 Ω·cm, or less. Such a low resistivity is sufficiently adequate to allow the material to be used in electroanalysis.[35]

In this relatively new area of research, it has been shown that diamond is useful for the detection of Hg(II), Pb(II), Mn(II), Cd(II), Cu(II) and Ag(I).[36-42] The properties of diamond are compared with those of Hg in Table 1.2. Clearly, diamond possesses many of the same attributes as Hg. Boron-doped diamond electrodes have been employed for the detection of Pb(II) in river sediments.[39, 43] It has also been successfully employed for the detection of Mn(II) in tea samples.[44] Prado et al. reported the simultaneous electrochemical detection and determination of Pb(II) and Cu(II) at boron-doped diamond electrodes.[45] Independent detection of Cu(II) and Pb(II) via conventional standard addition procedures was accomplished with diamond. The use of nitrogen-doped, diamond-like carbon film electrodes for the analysis of Pb (II), Cu (II), and Cd(II) was also recently described.[46] A linear dependence of the Pb(II) stripping peak current with concentration from 5×10^{-7} to 2×10^{-6} M (100 to 400 ppb) was observed for a deposition time of 2 minutes (with stirring).

Very recently, Kruusma and co-workers reported the electroanalytical determination of Pb(II) by ASV using a Bi-modified, boron-doped diamond electrode. Detection limits of 1.1×10^{-8} M (0.2 ppb) and 9.6×10^{-8} M (2.3 ppb) were obtained after 5 and 1 min deposition times, respectively.[47] Babyak and Smart described the detection of Cd(II) and Pb(II) at boron-doped diamond electrodes. The lowest concentrations detected within the linear dynamic range (5 min deposition time) for Cd(II) were 10 ppb and 50 ppb in KCl and KNO_3, respectively, and 10 ppb for Pb(II) in KNO_3.[48]

In summary, a few groups have recently reported on the use of conducting diamond in ASV and shown that it is a viable electrode material for the detection of metal ions. We recently reported the detection and quantification of Ag (I), Cu (II), Pb (II), Cd (II), and Zn (II) in several contaminated water samples using DPASV and a nanocrystalline diamond thin-film electrode.[4] Diamond was shown to function well in this electroanalytical application, providing a wide linear dynamic range, limits of quantitation in the low ppb range, excellent response precision, and good response accuracy.[3] For the analysis of Pb(II), bare diamond provided a response nearly identical to that obtained with a Hg-coated GC electrode.

1.5 Outline of the Dissertation

Overall, the research effort sought to answer the key questions enumerated in the first section. The dissertation is organized as follows. In Chapter 2, the experimental aspects of this work are described. Information about the diamond film synthesis and subsequent characterization by atomic force microscopy, visible-Raman spectroscopy, cyclic voltammetry and scanning electrochemical microscopy is given. In Chapter 3, the theory of metal phase formation (nucleation and growth) on solid electrodes is described. The characteristic voltammetric responses for the metal ions studied are presented. Results from the in-situ atomic force microscopic and chronoamperometric studies of Cu deposition on diamond thin-films are also described.

Boron-doped diamond thin films of different morphologies (microcrystalline and nanocrystalline) were used to assay for Ag(I), Pb(II), Cd(II), Cu(II), and Zn(II), individually and in mixtures, using DPASV. A performance comparison of the two diamond film types with bare and Hg-coated GC is given in Chapter 4.

Chapter 5 reports on the detailed analysis of Ag(I), Cu(II), Pb(II), Cd(II), and Zn(II) in contaminated water samples by DPASV using a boron-doped nanocrystalline diamond thin-film electrode. Data for the detection of these metal ions in four sample types are presented: lake water, tap water, wastewater treatment sludge, and soil. The data are validated through comparison measurements using ICP-MS and or AAS.

Intermetallic compound formation can be a complicating factor in ASV. A series of anodic stripping voltammetric i-E curves, obtained by the oxidation of metal deposits formed from binary solutions of Cu(II) and Zn(II) in varying ratios, were studied to learn how much of a factor intermetallic compound formation is on diamond. Results and discussion of these experiments is presented in Chapter 6. Our initial efforts using pulsed galvanostatic deposition instead of constant potential deposition, to minimize intermetallic compound formation are also reported in chapter 6. The co-deposition of Cu and Zn was used to evaluate the effectiveness of the pulsed current approach.

1.6 References

(1) Swain, G. M.; Anderson, A. B.; Angus, J. C. *MRS Bulletin* **1998**, *23*, 56-60.

(2) Granger, M. C.; Xu, J.; Strojek, J. W.; Swain, G. M. *Analytica Chimica Acta* **1999**, *397*, 145-161.

(3) Show, Y.; Witek, M. A.; Sonthalia, P.; Swain, G. M. *Chemistry of Materials* **2003**, *15*, 879-888.

(4) Sonthalia, P.; McGaw, E.; Show, Y.; Swain, G. M. *Analytica Chimica Acta* **2004**, *522*, 35-44.

(5) Awada, M.; Strojek, J. W.; Swain, G. M. *Journal of the Electrochemical Society* **1995**, *142*, L42-L45.

(6) Wang, J.; Swain, G. M.; Tachibana, T.; Kobashi, K. *Journal of New Materials for Electrochemical Systems* **2000**, *3*, 75-82.

(7) Friberg, L.; Nordberg, G. F.; Vouk, V. B.; Editors, Eds. *Handbook on the Toxicology of Metals*, 1979

(8) Anon, Ed. *Principles of biochemical toxicology, edited by John Timbrell*, 2000

(9) Goyer, R. A. *American journal of clinical nutrition*, *61*, 646S-650S.

(10) Online *http://www.epa.gov/safewater/mcl.html*. (Accessed June 2004)

(11) Klaassen, C. D.; Editor, Eds. *Casarett and Doull's Toxicology: The Basic Science of Poisons. 6th Ed*; McGraw-Hill, 2001

(12) Wang, J., Ed. *Stripping Analysis: Principles, Instrumentation, and Applications*; VCH Publishers, Inc., 1985

(13) Wang, J., Ed. *Analytical Electrochemistry*; John Wiley and Sons, Inc.: New York, 2000

(14) Florence, T. M. *Analytica Chimica Acta* **1980**, *119*, 217-223.

(15) Kissinger, P. T.; Heineman, W. R.; Editors, Eds. *Monographs in Electroanalytical Chemistry and Electrochemistry, Vol. 5: Laboratory Techniques in Electroanalytical Chemistry*, 1984

(16) Birke, R. L. *Analytical Chemistry* **1978**, *50*, 1489-1496.

(17) Dillard, J. W.; Hanck, K. W. *Analytical Chemistry* **1976**, *48*, 218-222.

(18) Dillard, J. W.; Turner, J. A.; Osteryoung, R. A. *Analytical Chemistry* **1977**, *49*, 1246-1250.

(19) Keller, H. E.; Osteryoung, R. A. *Analytical Chemistry* **1971**, *43*, 342-348.

(20) Oldham, K. B. *Analytical Chemistry* **1968**, *40*, 1024-1031.

(21) Osteryoung, R. A.; Parry, E. P. *Journal of Electroanalytical Chemistry (1959-1966)* **1965**, *9*, 299-304.

(22) Osteryoung, R. A.; Christie, J. H. *Analytical Chemistry* **1974**, *46*, 351-355.

(23) Barker, G. C.; Gardner, A. W. *At. Energy Research Estab. (Gt. Brit.) Rept.* **1961**, *AERE C/R-2297*, 12 pp.

(24) Barker, G. C.; Gardner, A. W. *Zeitschrift fuer Analytische Chemie* **1960**, *173*, 79-83.

(25) Wang, J.; Tian, B. *Analytical chemistry*, *65*, 1529-1532.

(26) Nolan, M. A.; Kounaves, S. P. *Analytical Chemistry* **1999**, *71*, 3567-3573.

(27) Hutton, E. A.; Ogorevc, B.; Hocevar, S. B.; Weldon, F.; Smyth, M. R.; Wang, J. *Electrochemistry Communications* **2001**, *3*, 707-711.

(28) Feeney, R.; Kounaves, S. P. *Analytical Chemistry* **2000**, *72*, 2222-2228.

(29) Bonfil, Y.; Kirowa-Eisner, E. *Analytica Chimica Acta* **2002**, *457*, 285-296.

(30) Brainina, K. Z.; Malakhova, N. A.; Ivanova, A. V. *NATO ASI Series, Series 2: Environment* **1997**, *38*, 255-269.

(31) Laitinen, H. A.; Watkins, N. H. *Analytical Chemistry* **1975**, *47*, 1352-1358.

(32) Wang, J.; Lu, J.; Hocevar, S. B.; Ogorevc, B. *Electroanalysis* **2001**, *13*, 13-16.

(33) Wu, K.; Hu, S.; Fei, J.; Bai, W. *Analytica Chimica Acta* **2003**, *489*, 215-221.

(34) Kwok, K.; Chiu, W. K. S. *Carbon* **2005**, *43*, 437-446.

(35) Xu, J.; Granger, M. C.; Chen, Q.; Strojek, J. W.; Lister, T. E.; Swain, G. M. *Analytical Chemistry* **1997**, *69*, 591A-597A.

(36) Saterlay, A. J.; Tibbetts, D. F.; Compton, R. G. *Analytical Sciences* **2000**, *16*, 1055-1060.

(37) Manivannan, A.; Seehra, M. S.; Tryk, D. A.; Fujishima, A. *Analytical Letters* **2002**, *35*, 355-368.

(38) Manivannan, A.; Tryk, D. A.; Fujishima, A. *Electrochemical and Solid-State Letters* **1999**, *2*, 455-456.

(39) Saterlay, A. J.; Agra-Gutierrez, C.; Taylor, M. P.; Marken, F.; Compton, R. G. *Electroanalysis* **1999**, *11*, 1083-1088.

(40) Ramesham, R. *Journal of Materials Science* **1999**, *34*, 1439-1445.

(41) Rychen, P.; Perret, A.; Gobet, J.; Madore, C.; Haenni, W. *Proceedings - Electrochemical Society* **2001**, *2001-23*, 97-107.

(42) Peilin, Z.; Jianzhong, Z.; Shenzhong, Y.; Xikang, Z.; Guoxiong, Z. *Fresenius' Journal of Analytical Chemistry* **1995**, *353*, 171-173.

(43) Tsai, Y.-C.; Coles, B. A.; Holt, K.; Foord, J. S.; Marken, F.; Compton, R. G. *Electroanalysis* **2001**, *13*, 831-835.

(44) Saterlay, A. J.; Foord, J. S.; Compton, R. G. *Analyst*, *124*, 1791-1796.

(45) Prado, C.; Wilkins, S. J.; Marken, F.; Compton, R. G. *Electroanalysis* **2002**, *14*, 262-272.

(46) Zeng, A.; Liu, E.; Tan, S. N.; Zhang, S.; Gao, J. *Electroanalysis* **2002**, *14*, 1294-1298.

(47) Kruusma, J.; Banks, C. E.; Compton, R. G. *Analytical and Bioanalytical Chemistry* **2004**, *379*, 700-706.

(48) Babyak, C.; Smart, R. B. *Electroanalysis* **2004**, *16*, 175-182.

CHAPTER 2

THE PHYSICAL CHARACTERIZATION AND ELECTROCHEMICAL PROPERTIES OF BORON-DOPED DIAMOND THIN-FILM ELECTRODES

2.1 Introduction

The structural and electrochemical characterization data for diamond thin-film electrodes deposited using microwave assisted plasma chemical vapor deposition (CVD) are reported. Two types of conducting diamond with different surface morphologies and microstructures were investigated and compared, microcrystalline and nanocrystalline films. The motivation for studying these two types of diamond stems from the fact that the different morphology and microstructure of each could significantly influence the nucleation site density, particle density and particle size of the metal deposits. This could, in turn, affect the electrode response for the metal ions.

Table 2.1 lists the instrumental techniques used in our laboratory for characterizing of the physical, chemical and electronic properties of diamond thin-films along with the information gained from each.[1, 2] Results from the characterization by atomic force microscopy, visible Raman spectroscopy, x-ray diffraction and cyclic voltammetry, using $Fe(CN)_6^{-3/-4}$, $Ru(NH_3)_6^{+3/+2}$, $IrCl_6^{-2/-3}$ and methyl viologen as redox test probes, are presented in this Chapter. Scanning electrochemical microscopy (SECM) was also used to characterize the spatial electrochemical activity of the diamond electrodes using probe approach curves in the positive feedback mode.[3, 4]

Table 2.1 Instrumental Techniques used for characterization.

Technique	*Information*
SEM	Morphology
AFM	Morphology
Raman	Microstructure
XRD	Crystallinity
4-pt probe	Resistivity
SECM	Local Electrochemical Activity

2.2 Experimental

Film Growth and Characterization. The diamond thin films were deposited on p-type Si(100) substrates (~10^{-3} Ω-cm, Virginia Semiconductor Inc., Fredricksburg, VA), using a commercial microwave-assisted chemical vapor deposition (CVD) system (1.5 kW, Astex, Inc., Lowell, MA). The Si surface was prepared for diamond growth by mechanically scratching the surface on a felt pad with 1 μm diameter diamond powder (GE Superabrasives, Worthington, OH). The scratched substrate was then sequentially washed with ultrapure water, isopropyl alcohol (IPA), acetone, IPA, and ultrapure water. Finally, it was ultrasonicated for 5 min each in acetone and ultrapure water. The cleaned substrate was placed in the CVD reactor.

The microcrystalline films were grown using a $CH_4/H_2/B_2H_6$ source gas mixture at a CH_4/H_2 volumetric ratio of 0.50%, a total gas flow of 200 sccm, a microwave power of 1000 W, a growth pressure of 45 torr, an estimated substrate temperature of 800°C, and a growth time of ca. 10 h. Ultrahigh purity (99.999%) CH_4, at a flow rate of 1 sccm, and H_2 at a flow rate of 197 sccm were used. B_2H_6, diluted in H_2 (0.1%) was used for boron doping at a flow rate of 2 sccm. The concentration of B_2H_6 in the source gas mixture was 10 ppm (1×10^{-3}%). After growth, the CH_4 and B_2H_6 flows were stopped and the films remained exposed to the hydrogen plasma (atomic hydrogen) for an additional 10 min. Next, the microwave power was gradually reduced over a 15 min period down to 400 W in order to cool the samples in the presence of atomic hydrogen. Post growth annealing in atomic hydrogen is necessary for full hydrogen surface termination and ensuring the removal of adventitious non-diamond sp^2 carbon impurity.

For the nanocrystalline films, ultrahigh purity CH_4, Ar, and H_2 (99.999 %) were used as the source gas mixture. The gas flow rates were 1, 94, and 5 sccm, respectively, for CH_4 (1%), Ar (94%), and H_2 (5%). B_2H_6 was used for doping at a flow rate of 0.001 sccm (10 ppm). The microwave power and deposition pressure were maintained at 800 W and 140 torr, respectively. The substrate temperature was estimated to be about 800 °C using an optical pyrometer. The deposition time was 2 h. The plasma was ignited and deposition initiated with all the gases flowing into the reactor. At the end of the deposition period, the CH_4 and B_2H_6 flows were stopped, and the Ar and H_2 flows continued. The film was exposed to H_2/Ar plasma for 10 min. The substrate was then cooled in the presence of hydrogen to an estimated temperature of less than 300 °C by slowly reducing the power and pressure over a 4 min period.

The resulting diamond thin films were approximately 4-6 μm thick, as estimated from cross sectional SEM images. The nominal resistivity was found to be 0.01 Ω-cm, or less, for the microcrystalline and 0.1 Ω-cm, or less, for the nanocrystalline films using the four-point probe method.

The surface morphology of the boron-doped diamond thin-films was investigated by the atomic force microscopy (Nanoscope IIIa, Digital instruments, Santa Barbara, CA). The crystalline structure was characterized by Raman spectroscopy.[5] The turn key instrument consisted of a diode-pumped, frequency-doubled CW Nd: yttrium aluminium garnet (YAG) excitation laser of 523 nm and objective lens of x 20 (Raman 2000, Chromex, Inc Albuquerque, NM). Spectra were collected with an incident power density of ~ 500 kW/cm^2, a 10 s integration time and spectral resolution of about 2 cm^{-1}. A white light spectrum collected under the same conditions was used for background correction. X-ray diffraction (XRD) was employed to characterize the bulk crystallinity of the diamond thin films. A Rigaku Rotaflex diffractometer equipped with a rotating anode and a Cu K-α radiation source was used to obtain the XRD patterns. The thin film rotates by an angle, θ, with respect to a fixed x-ray source, and the detector rotates by 2θ to measure the reflected light. The measurements were made from 2θ of 30° to 100°.

Electrochemistry. A single-compartment glass cell was used for all the electrochemical measurements, along with a computer-controlled potentiostat (Model 650a CH Instruments Inc., Austin, TX).[6] The diamond thin-film working electrode was pressed against a Viton® o-ring and clamped to the bottom of the cell. The backside of the Si substrate was scratched with a carbon rod to ensure good ohmic contact with the current-collector plate. A graphite rod was used as the counter electrode, and a commercial Ag/AgCl electrode (saturated KCl) served as the reference ($E^0_{Ag/AgCl}$ = -0.045 V vs. SCE). The geometric area of the working electrode was ca. 0.163 cm^2. All measurements were made in solutions deoxygenated with N_2 for at least 5 min initially. The solutions were blanketed with the gas during all measurements. The reference electrode was placed inside a cracked-glass capillary (double junction) that was filled with 1 M KCl. All measurements were performed at room temperature, ~ 25 ^{0}C. The supporting electrolyte was 1 M KCl. The concentrations of $Fe(CN)_6^{-3/-4}$, $Ru(NH_3)_6^{+2/+3}$, $IrCl_6^{-2/-3}$ and methyl viologen were 1 mM.

SECM experiments were conducted using a CHI 900 SECM (CH Instruments, Austin, TX). The tip could be moved in the x,y and z directions using an inch-worm controller. The x,y plane is along the substrate surface and the z plane is perpendicular to this plane. For approach curves, the tip was moved towards the substrate surface in 0.2 µm increments (along the –z axis). The approach was terminated when the tip current reached 115% (positive feedback) and 75% (negative feedback) of its initial value. The initial value of the current, $i_{T,\infty}$, is defined as the current when the tip was "infinitely" far from the surface.

Pt probe tips were obtained from CH Instruments (Austin, TX). They were 2 μm diam. Pt wire sealed into glass. The SECM cell was made of Teflon. Pt wire was used as a counter electrode and an Ag/AgCl electrode served as the reference for all measurements. Prior to use the tips were cleaned by potential cycling in 0.5 M H_2SO_4[7] between -0.3 V and 0.9 V at 100 mV/s for 12.5 cycles. The resulting cyclic voltammetric i-E curves showed some/all the features for Pt, Pt oxide formation, oxygen evolution, Pt oxide reduction, hydrogen adsorption and desorption and hydrogen evolution. The voltammetric i-E curves for $Ru(NH_3)_6^{+3/+2}$, at the ultra-microelectrode tips, showed classical sigmoidal shapes. $Ru(NH_3)_6^{+3/+2}$ was chosen as a mediator because its kinetics for electron transfer are mainly dependent on the density of electronic states and would indicate the charge carrier density at the formal potential of the material being examined. 1 mM $Ru(NH_3)_6{}^{+2/+3}$ in 1 M KCl was used as the redox mediator for all the probe-approach measurements. The solution was degassed using N_2 for 5 minutes prior to introduction into the cell. For all the probe approach measurements, the tip was poised at a potential of -0.3 V and the substrate at a potential of 0.05 V.

2.3 Results and Discussion

2.3.1 Structural Characterization.

Atomic force microscopy (AFM) provides information about the film morphology, while Raman spectroscopy is useful for evaluating the film microstructure and for detecting the presence of any localized non-diamond sp^2-bonded carbon impurity. Figure 2.1. shows 5×5 μm^2 AFM images (height mode, ex-situ) of microcrystalline and nanocrystalline thin-film electrodes. The microcrystalline film is polycrystalline and well-faceted with randomly-oriented crystallites having lateral dimensions of 0.5 to 4 μm at the base. The nanocrystalline film is also polycrystalline but much smoother with feature sizes of ca. 100 nm in lateral dimension. These features are actually clusters of randomly-oriented diamond grains that are approximately 15 nm in diameter, as revealed by transmission electron microscopy (TEM).[8] As a consequence of the much smaller grain size, the nanocrystalline film contains a much higher fraction of grain boundary. The abrupt grain boundaries consist of π - bonded carbon atoms.[9]

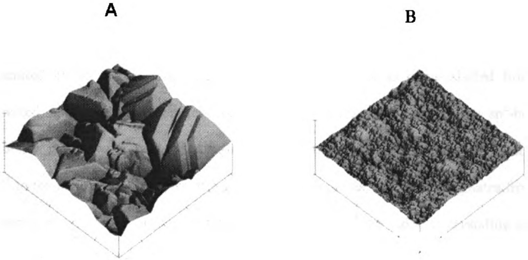

Figure 2.1 5×5 μm^2 AFM images (height mode) of boron-doped (A) microcrystalline and (B) nanocrystalline diamond films.

Figures 2.2.A and 2.2.B show macro-Raman spectra for the microcrystalline and nanocrystalline diamond thin-film electrodes, respectively. Raman spectroscopy is a nondestructive technique often used to determine the nanostructure of carbon thin-films due to its ability to discriminate between the sp^2 and sp^3-bonded carbon as well as the local bonding environment of carbon.[10] The first-order diamond phonon line is observed at 1332 cm^{-1} for the microcrystalline film, which originates from the sp^3-bonded carbon microstructure.[9] For the microcrystalline diamond film, weak asymmetry and broadening appears in the one phonon band and also an appearance of a new band centered at around 1200 cm^{-1} is observed. This has been attributed to the high boron doping effect.[11] As diamond thin-films undergo a transition from a microcrystalline to nanocrystalline morphology, the Raman spectra become dominated by scattering from the sp^2-bonded carbon located at the grain boundaries.[12] Due to resonance effects, the Raman cross-section scattering coefficient (visible excitation) is larger (50×) than that for the sp^3-bonded diamond.[13] At the nanocrystalline diamond, there are peaks observed at 1332 cm^{-1} and near 1500 cm^{-1}. These peaks are the D-band and G-band routinely observed in sp^2-bonded carbon.[12] The diamond peak at 1332 cm^{-1} is not visible above the signal generated by the sp^2-bonded carbon. The 1550 cm^{-1} peak is down shifted from the expected 1580 cm^{-1} position for graphite. This shift results because the sp^2-bonded carbon is mixed with sp^3-bonded carbon. Further there is also a peak observed at 1140 cm^{-1} in the nanocrystalline film. It was widely believed that this peak originates from the presence of confined phonon modes in diamond, due to the reduced crystallite size of nanocrystalline diamond.[14] However, Ferrari et al. suggested that these features may have their origin in sp^2-bonded carbon.[15] More recently this peak has been reported to be specifically caused by carbon-hydrogen bonds in the grain boundaries.[12]

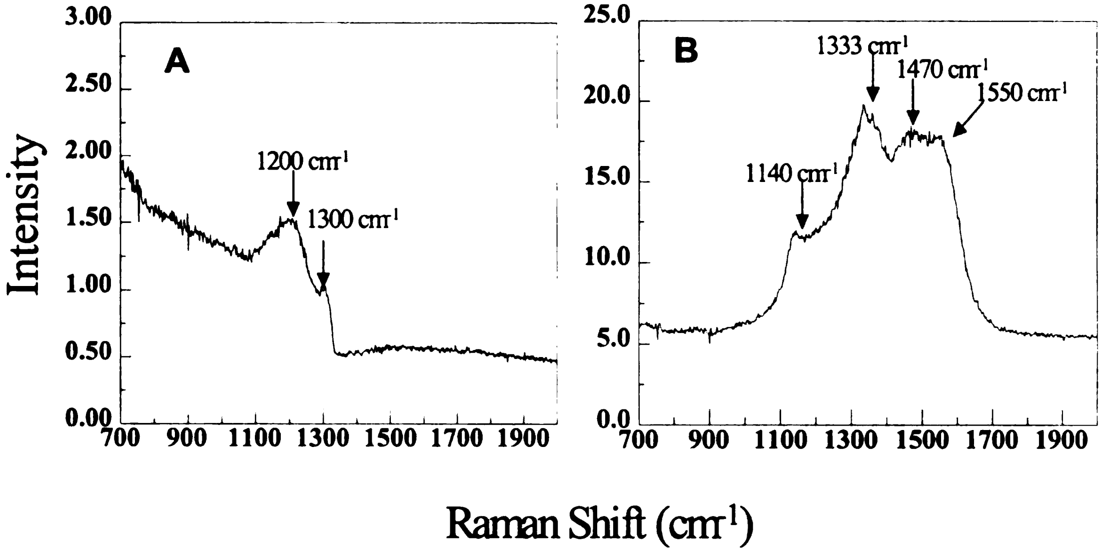

Figure 2.2 Visible macro-Raman spectra of (A) microcrystalline and (B) nanocrystalline diamond films

X-ray diffraction (XRD) was employed to characterize the bulk crystallinity of the diamond thin-films.[8] Figure 2.3 shows the XRD spectra for a (A) microcrystalline and (B) nanocrystalline diamond thin film. For both films, three reflections are observed at 2θ values of 44°, 76°, and 92°, and are assigned to the (111), (220), and (311) planes of cubic diamond, respectively.[8, 16] Well-defined and sharp (111) peaks indicate high quality of the diamond films. The peaks for the nanocrystalline film are broader than those for the microcrystalline film due to the smaller grain size. This result confirms that both film types possess a crystalline diamond structure.

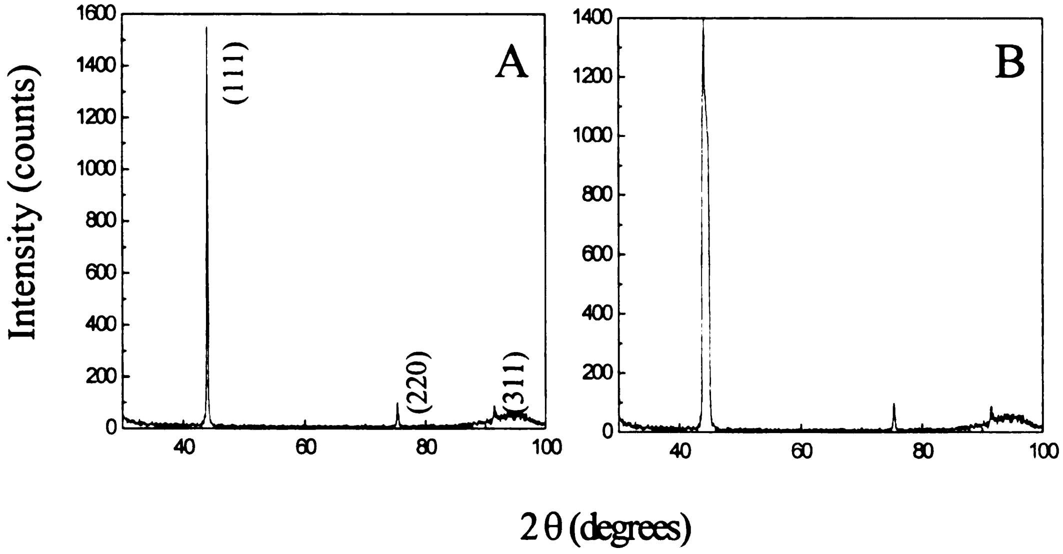

Figure 2.3 XRD patterns of (A) microcrystalline and (B) nanocrystalline diamond films

2.3.2 Electrochemical Characterization

Figure 2.4 shows background cyclic voltammetric i-E curves for boron-doped (A) microcrystalline and (B) nanocrystalline diamond thin films at 100 mV/s in 1.0 M KCl. The curves shown are for the tenth scan, and are flat and featureless over much of the potential range. The working potential window is about 2.7 V (± 100 μA) with a featureless response between the working potential limits. The anodic current flowing at 1150 mV is due to the oxidation of chloride to chlorine. The cathodic current flowing at –1400 mV is due to the reduction of water to hydrogen.

At 500 mV, the anodic current for the nanocrystalline film is 1.4 μA (7 μA/cm^2) and the anodic current for the microcrystalline film is 1.5 μA (8 μA/cm^2). The current for both diamond electrodes, however, is less than that for freshly polished glassy carbon (GC), 7-10 μA (35–50 μA/cm^2). A low background current and wide working potential window (3 to 4 V) are characteristic features of high quality, boron-doped diamond.[17] This leads to improved S/N ratios in electroanalytical measurements.[18] The lower potential window seen for the two diamond films is due to the fact that KCl was used as the supporting electrolyte rather than acid ($HClO_4$) and chlorine evolution occurs on diamond with relatively low overpotential.

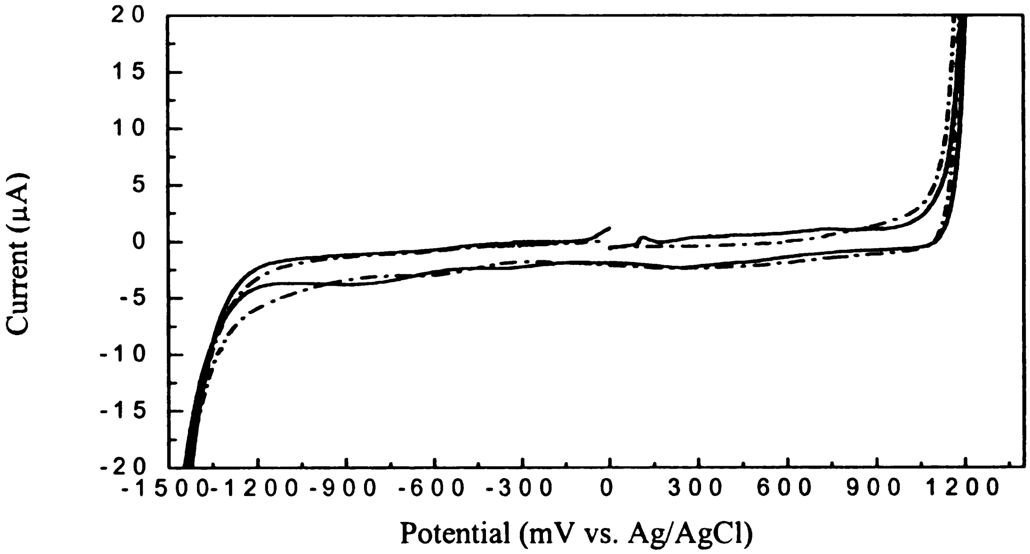

Figure 2.4 Background cyclic voltammetric i-E curves in 1 M KCl for (A) microcrystalline diamond (——) and (B) nanocrystalline diamond (-·-·-·-) thin-film electrodes.

The electrochemical responsiveness of the boron-doped microcrystalline and nanocrystalline diamond thin films towards four different redox systems was investigated using cyclic voltammetry. The physical, chemical and electronic properties of the diamond influence the electrode kinetics and reaction mechanism for these systems.[1, 8, 19, 20] Figure 2.5 shows representative cyclic voltammetric i-E curves for (A) $Fe(CN)_6^{-3/-4}$, (B) $Ru(NH_3)_6^{+2/+3}$, (C) $IrCl_6^{-2/-3}$, (D) methyl viologen ($MV^{+2/+}$) at a microcrystalline diamond thin-film electrode. The electrolyte was 1 M KCl and the potential sweep rate ranged from 50 to 2000 mV/s. $E_{½}$ for these redox systems ranges from approximately 800 to -1100 mV, so they are useful for probing the film's electronic properties over a wide potential (i.e., energy) range.

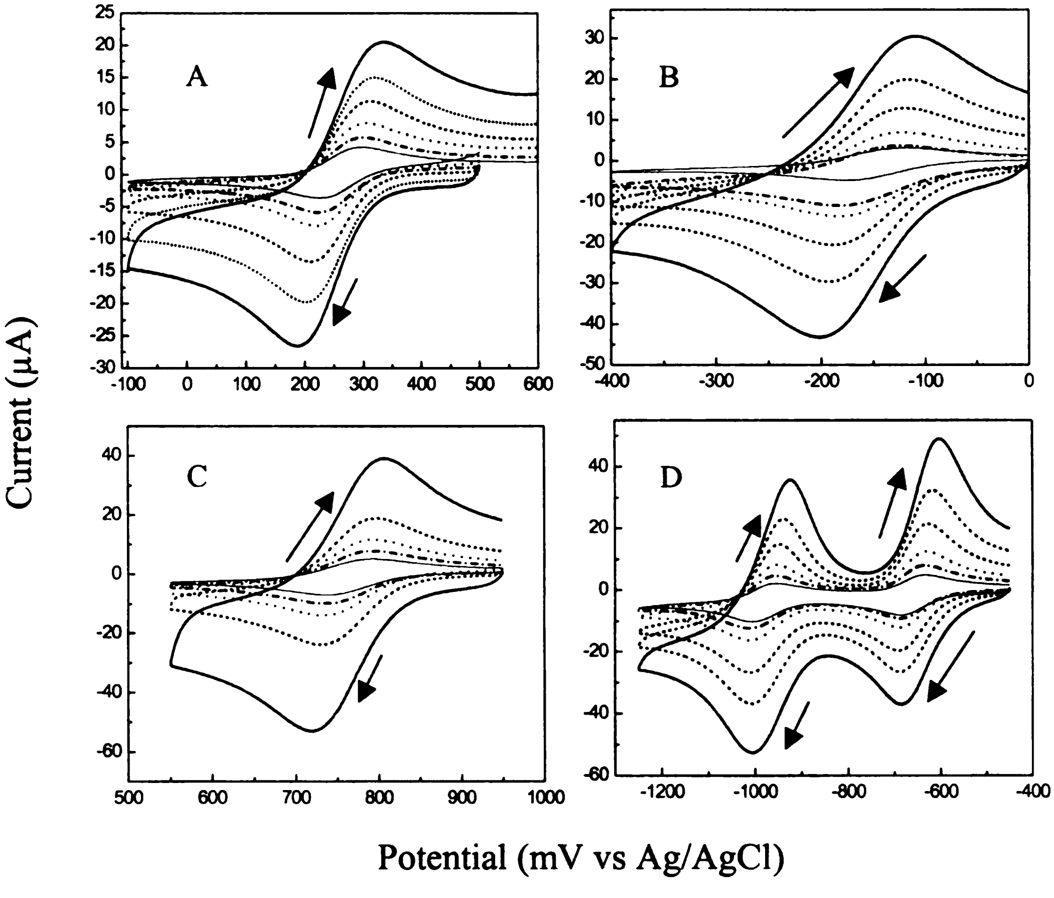

Figure 2.5 Cyclic voltammetric i-E curves for (A) $Fe(CN)_6^{-3/-4}$, (B) $Ru(NH_3)_6^{+2/+3}$, (C) $IrCl_6^{-2/-3}$, and (D) methyl viologen ($MV^{+2/+}$) at increasing scan rates of 50, 100, 200, 500, 1000 and 2000 mV/s.

A nearly reversible response is observed for $Fe(CN)_6^{-3/-4}$ with a ΔE_p of 69 mV at 100 mV/s and an i_p^{ox}/i_p^{red} of 1.0. $Fe(CN)_6^{-3/-4}$ is a surface-sensitive redox system at both glassy carbon and boron-doped microcrystalline diamond.[20] The electrode reaction kinetics for this couple is strongly influenced by the amount of exposed edge plane on sp^2–bonded carbon as well as the surface cleanliness.[21] Granger and co-workers showed that surface carbon-oxygen functionalities on microcrystalline diamond significantly influence ΔE_p with increasing oxygen content causing a proportional increase in ΔE_p. The small ΔE_p seen for the boron-doped microcrystalline diamond film is indicative of a high level of surface cleanliness and a low surface oxide coverage.[22]

A nearly reversible response is also seen for $Ru(NH_3)_6^{+2/+3}$ with a ΔE_p of 71 mV at 100 mV/s and an i_p^{ox}/i_p^{red} of 1.0. A nearly reversible response is also seen for $IrCl_6^{-2/-3}$ at 100 mV/s with a ΔE_p of 69 mV and an i_p^{ox}/i_p^{red} of 1.0. The electrode reaction kinetics for both of these redox systems are not as sensitive to the physicochemical properties of both sp^2-bonded carbon and diamond electrodes as is $Fe(CN)_6^{-3/-4}$.[9, 20] The kinetics are mainly influenced by the density of electronic states at the potentials where the electrolysis occurs (i.e., near the $E^{o\prime}$). In other words, the diamond electrode is sufficiently conductive at both –200 mV, a potential negative of the flatband potential (ca. 0.5 V vs. Ag/AgCl) for p-type semiconducting diamond, and 800 mV, a potential positive of the flatband potential.[17]

A reversible response is seen for $MV^{+2/+1}$ with a ΔE_p of 62 mV and an i_p^{ox}/i_p^{red} of 1.0. Like $Ru(NH_3)_6^{+2/+3}$ and $IrCl_6^{-2/-3}$, the electrode reaction kinetics for $MV^{+2/+1}$ are relatively insensitive to the physicochemical properties of both sp^2-bonded carbon and diamond electrodes.[20] The kinetics are mainly influenced by the density of electronic states at the potential where the electrolysis occurs. MV undergoes two redox processes. Good responsiveness was also observed for the other redox couple, $MV^{+1/0}$. The cathodic peak at –990 mV is associated with the reduction of $MV^{+\bullet}$ to MV^0. The peak shape is consistent with a diffusion-limited reaction. Plots of i_p^{ox} versus scan rate$^{1/2}$ ($\nu^{1/2}$) were constructed for the four redox couples in question at the various scan rates studied. It was observed that the oxidation peak current for each redox system varied linearly with the $\nu^{1/2}$, with a near-zero y-axis intercept, indicative of reactions limited by semi-infinite linear diffusion of reactants to the electrode surface. Similar cyclic voltammetric results for the four couples were observed on the nanocrystalline diamond. The quasi-reversible voltammetry for all the couples indicates that both the kinds of diamond have a sufficient charge carrier density over the wide potential range to support relatively rapid electron transfer.

2.3.3 Electrochemical Activity as Studied by the Scanning Electrochemical Microscopy (SECM)

Probe Approach Curves. SECM can be used to study the spatial electrochemical activity of an electrode and distinguish between conducting and insulating regions on a substrate through probe-approach curves. In the feedback mode, an ultra-microlectrode (UME) tip is perturbed from its value in bulk solution by a much larger substrate in close proximity.[23] For example, if an oxidizing species "O" in the bulk solution is reduced at the UME tip, and the substrate is conductive and is held at a sufficiently positive potential, then the tip-generated reduced species "R" is oxidized back to "O" at the substrate and the tip current becomes larger than its magnitude when it is "infinitely" far from the substrate, as denoted by $i_{T,\infty}$. This is called the positive feedback mode. At insulating substrates, no oxidation of "R" occurs and the tip current decreases from $i_{T,\infty}$ due to blockage of the diffusional flux of "R" to the tip (negative feedback). For all the probe approach measurements, the tip was poised at a potential of -0.3 V and the substrate at a potential of 0.05 V. In Figure 2.6, an example of negative feedback is shown. As the tip, set at a reducing potential, approaches the substrate $i_{T,\infty}$ decreases because the flux of reactant to the tip is inhibited when the tip is in close proximity to the substrate. All tip current values are normalized to $i_{T,\infty}$. L is the normalized tip-substrate distance (d/a), where d is the distance traveled by the tip and a is the tip electrode radius.

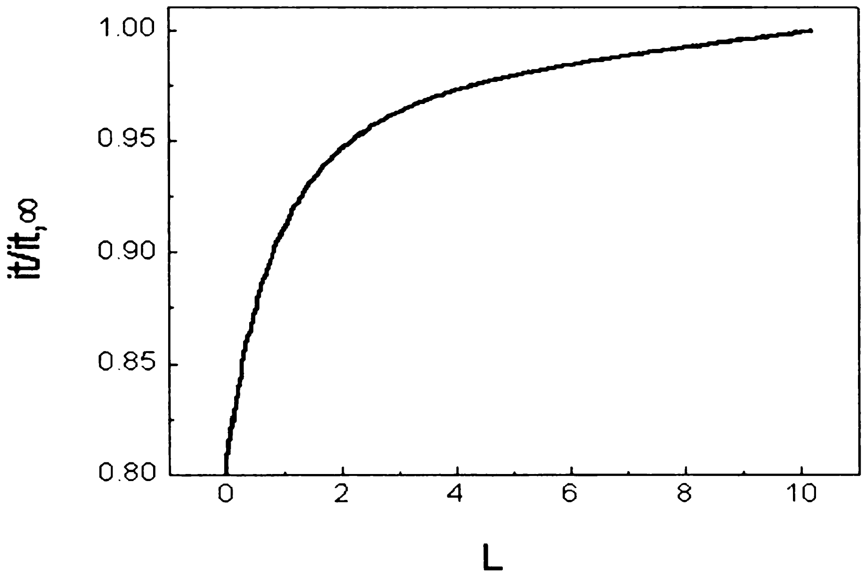

Figure 2.6 Tip-approach curve at a polycarbonate substrate. The data were acquired in a 1 mM solution of $Ru(NH_3)_6^{3+}$ in 1 M KCl. The tip is a 10 μm-radius Pt disk. The tip was biased at -0.3 V.

Figure 2.7 shows representative positive feedback current-distance approach curves obtained using boron-doped microcrystalline and nanocrystalline diamond and a Pt film as substrates and a 2 μm Pt tip as the probe. Five to six spots on the diamond surface were probed. Positive feedback was observed at all the locations and the pattern of the curves and magnitude of the current enhancement was similar. To facilitate comparison between approach curves, the tip currents were normalized to the steady-state values obtained at infinite distance. The theoretical curve for a uniformly active substrate has also been shown in the Figure. The data for the diamond films indicate that these electrodes are electrically conducting with fast heterogeneous kinetics for $Ru(NH3)_6^{+3/+2}$ at this potential. The activity is comparable to Pt. Furthermore, probe-approach curves recorded for the microcrystalline diamond were reproducible for multiple spots whereas those on nanocrystalline diamond varied slightly, possibly indicating that this surface was more heterogeneous in conductivity. Microcrystalline diamond electrodes have fewer grain boundaries separating the individual crystallites. The grain boundaries are known to be rich in sp^2-bonded carbon while the grains predominantly contain sp^3-bonded carbon. The microcrystalline diamond is thus expected to be microstructurally homogeneous compared to the nanocrystalline variety. However the sp^2-bonded carbon grain boundaries are known to be more electrically conductive. The behavior of the nanocrystalline diamond was observed to be closer to the theoretical curve indicating that this diamond type has a higher overall surface conductivity than the microcrystalline variety.

According to Amphlett and Denault, an equation for a current-distance curve controlled by a positive feedback is given below.[24] They showed how the four coefficients, k_1, k_2, k_3 and k_4, change with RG (ratio of the insulating glass sheath radius to that of the electroactive disk) values.

$$i_{tip}/i_{tip,\infty} = k_1 + (k_2/L) + k_3 \exp(k_4/L) \qquad (2.1)$$

The theoretical curve depicted in Figure 2.7 has been constructed using the above equation and values of the constants interpolated to an RG ratio of 6.5. The values of the four coefficients k_1, k_2, k_3 and k_4 were 0.7220, 0.7555, 0.2647 and 1.5640, respectively. The current values were plotted upto a limit of 115% of the $i_{T,\infty}$, to facilitate comparison to the experimental curves. The theoretical curve has a current increase further away from zero than the experimental curves, either due to a different true RG value or due to the fact that the experimental substrates may not be uniformly reactive. Various RG values ranging from 1.5 to 7.5 were tested, however, the experimental and theoretical curves did not coincide. To explain this data, the theory of finite heterogeneous electron-transfer kinetics and arbitrary substrate size has been discussed next.

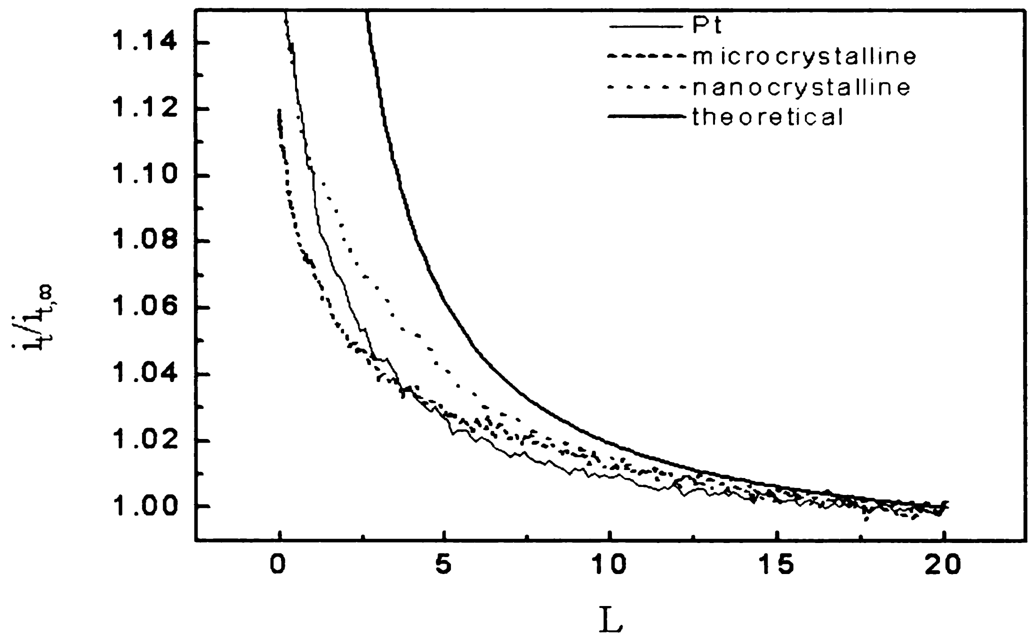

Figure 2.7 Tip approach-curves for the different electrode materials: platinum, microcrystalline and nanocrystalline diamond. The simulated current-distance data for a tip with an RG ratio 6.5 is also shown. Experimental curves were acquired in a 1 mM solution of $Ru(NH_3)_6^{3+}$ in 1 M KCl. The tip is a 2 μm-radius Pt disk of RG ratio between 6 and 7. The tip was biased at -0.3 V and the substrate at 0.05 V.

The theoretical curve in the previous section was calculated based on the assumption of a macroscopic (i.e., infinitely large compared to the tip), uniformly active substrate. This assumption may not be accurate when the substrate contains three-dimensional features, or consists of regions of different electrical conductivity or electrochemical activity. A schematic model showing SECM in the feedback mode with substrate of finite dimensions is shown in Figure 2.8. Only a portion of the substrate is active in terms of the regeneration of O from R. Very recently, the electrical conductivity and electrochemical activity at the surfaces of hydrogen-terminated boron-doped diamond electrodes, with different boron doping levels, was measured using conductive-probe atomic force microscopy (CP-AFM) and scanning electrochemical microscopy

(SECM).[25] SECM approach curves obtained using $Ru(NH_3)_6^{3+/2+}$ as the redox mediator were characteristic of those obtained at partially blocked electrodes of non-uniform activity or a microelectrode array. The active area of the electrode was related to the boron-doping level, however, even the heavily doped (10 ppm source gas B_2H_6) diamond electrode showed the behavior of partially blocked electrodes.

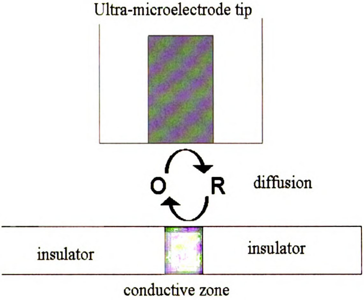

Figure 2.8 Schematic illustration of the SECM feedback mode with a finite substrate (Adapted from reference 26). The heterogeneous redox reactions occur at a diffusion-controlled rate at the ultra-microelectrode and conductive portion of the tip.

Further, Bard et al. studied the effect of finite substrate size by simulating current-distance curves over various sizes of microdisk substrates using two methods, multidimensional integral equations and the finite difference method.[26] The working curves, for various substrate sizes, representing the dependence of the steady-state diffusion-controlled current on the dimensionless distance between the tip and substrate are presented in Figure 2.9. Parameter, h, has been defined as:

$h = a_s/a$ where: a_s is the active substrate radius and a is the tip electrode radius.

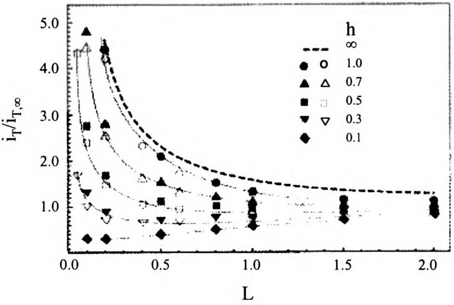

Figure 2.9 Simulated $i/i_{T,\infty}$ vs. L curves for finite disk-shaped substrates: (filled symbols) multidimensional integral equations simulations; (open symbols) finite difference method simulation. The h values are indicated. (Figure adapted from reference 26)

Bard et al. found that with decreasing h, the current-distance curves have a shallow slope and a sharp current rise close to L = 0. Comparing the two figures 2.7 and 2.9, it seems that the microcrystalline diamond has a slightly smaller "h" parameter (i.e., smaller conducting substrate features) than nanocrystalline diamond. This is again explained by the fact that the nanocrystalline diamond has a higher fraction of exposed grain boundary compared to the microcrystalline variety. As mentioned, the grain boundaries are more conductive than the grains.[8] The resolution of the instrument is a limiting factor. It is only possible to identify particles 10-20 times smaller than the tip by SECM.[26] With a tip 2 µm in diameter, this corresponds to 100-200 nm in size. The influence of the grains of the nanocrystalline diamond which are only 10-15 nm on the probe-approach curve may not have been resolvable. The curve for the Pt substrate also did not trace the theoretical curve, probably due to non-uniform conductivity caused by the presence of Pt surface oxides. Overall, it can concluded that since the current-distance curves obtained for diamond electrodes of both morphologies are similar to the one obtained for Pt macroelectrode, it seems that at this doping level, the diamond substrate can be treated as sufficiently conductive.

2.4 Conclusions

The physical characterization and electrochemical properties of diamond thin-film electrodes was reported on. Two types of conducting diamond with different surface morphologies and microstructures were investigated and compared, microcrystalline and nanocrystalline thin-films. Based on the electrochemical results, it is clear that both diamond types have a sufficient charge carrier density over a wide potential range to support relatively rapid electron transfer for several analytes. This evidence suggests that both types of diamond films are electrically conductive and electrochemically active electrodes. From the SECM approach curve measurements, it was demonstrated that diamond electrodes of both morphologies showed a positive feedback response that was comparable to a Pt macro-electrode. Probe-approach curves recorded for the microcrystalline diamond were reproducible for multiple spots whereas those on nanocrystalline diamond varied slightly, possibly indicating that this surface was more electrically heterogeneous. However, since the nanocrystalline diamond has a higher fraction of grain boundary than does microcrystalline diamond, a larger fraction of the former surface was determined to be electrically conducting (i.e., electrochemically active). Sufficient understanding of how the growth conditions of the diamond films affect the efficiency of stripping will enable development of even superior electrodes in the future. For instance, previous studies in our group, have shown that the copper nucleation mechanism on boron doped diamond film strongly depends on boron doping level of diamond film.[27]

2.5 References

(1) Xu, J.; Granger, M. C.; Chen, Q.; Strojek, J. W.; Lister, T. E.; Swain, G. M. *Analytical Chemistry* **1997**, *69*, 591A-597A.

(2) Hupert, M.; Muck, A.; Wang, J.; Stotter, J.; Cvackova, Z.; Haymond, S.; Show, Y.; Swain, G. M. *Diamond and Related Materials* **2003**, *12*, 1940-1949.

(3) Bard, A. J.; Mirkin, M. V.; Editors, Eds. *Scanning Electrochemical Microscopy*; Marcel Dekker, Inc., 2001

(4) Bard, A. J.; Fan, F.-R.; Mirkin, M. *Physical Electrochemistry* **1995**, 209-242.

(5) Dennison, J. R.; Holtz, M.; Swain, G. *Spectroscopy (Eugene, Oregon)* **1996**, *11*, 38-46.

(6) Xu, J.; Chen, Q.; Swain, G. M. *Analytical Chemistry* **1998**, *70*, 3146-3154.

(7) Seegmiller, J. C.; Buttry, D. A. *Journal of the Electrochemical Society* **2003**, *150*, B413-B418.

(8) Show, Y.; Witek, M. A.; Sonthalia, P.; Swain, G. M. *Chemistry of Materials* **2003**, *15*, 879-888.

(9) Granger, M. C.; Xu, J.; Strojek, J. W.; Swain, G. M. *Analytica Chimica Acta* **1999**, *397*, 145-161.

(10) Solin, S. A.; Ramdas, A. K. *Physical Review B: Solid State* **1970**, *[3] 1*, 1687-1698.

(11) Ushizawa, K.; Watanabe, K.; Ando, T.; Sakaguchi, I.; Nishitani-Gamo, M.; Sato, Y.; Kanda, H. *Diamond and Related Materials* **1998**, *7*, 1719-1722.

(12) Birrell, J.; Gerbi, J. E.; Auciello, O.; Gibson, J. M.; Johnson, J.; Carlisle, J. A. *Diamond and Related Materials* **2005**, *14*, 86-92.

(13) Knight, D. S.; White, W. B. *Journal of Materials Research* **1989**, *4*, 385-393.

(14) Nemanich, R. J.; Glass, J. T.; Lucovsky, G.; Shroder, R. E. *Journal of Vacuum Science & Technology, A: Vacuum, Surfaces, and Films* **1988**, *6*, 1783-1787.

(15) Ferrari, A. C.; Robertson, J. *Physical Review B: Condensed Matter and Materials Physics* **2001**, *63*, 1214051-1214054.

(16) Sharda, T.; Misra, D. S.; Seibt, E. W.; Selvam, P. *Journal of Vacuum Science & Technology, A: Vacuum, Surfaces, and Films* **1998**, *16*, 413-418.

(17) Swain, G. M.; Anderson, A. B.; Angus, J. C. *MRS Bulletin* **1998**, *23*, 56-60.

(18) Strojek, J. W.; Granger, M. C.; Swain, G. M.; Dallas, T.; Holtz, M. W. *Analytical Chemistry* **1996**, *68*, 2031-2037.

(19) Witek, M.; Wang, J.; Stotter, J.; Hupert, M.; Haymond, S.; Sonthalia, P.; Swain, G. M.; Zak, J. K.; Chen, Q.; Gruen, D. M.; Butler, J. E.; Kobashi, K.; Tachibana, T. *Journal of Wide Bandgap Materials* **2002**, *8*, 171-188.

(20) Granger, M. C.; Witek, M.; Xu, J.; Wang, J.; Hupert, M.; Hanks, A.; Koppang, M. D.; Butler, J. E.; Lucazeau, G.; Mermoux, M.; Strojek, J. W.; Swain, G. M. *Analytical Chemistry* **2000**, *72*, 3793-3804.

(21) Kneten, K. R.; McCreery, R. L. *Analytical Chemistry* **1992**, *64*, 2518-2524.

(22) Granger, M. C.; Swain, G. M. *Journal of the Electrochemical Society* **1999**, *146*, 4551-4558.

(23) Kwak, J.; Bard, A. J. *Analytical Chemistry* **1989**, *61*, 1794-1799.

(24) Amphlett, J. L.; Denuault, G. *Journal of Physical Chemistry B* **1998**, *102*, 9946-9951.

(25) Holt, K. B.; Bard, A. J.; Show, Y.; Swain, G. M. *Journal of Physical Chemistry B* **2004**, *108*, 15117-15127.

(26) Bard, A. J.; Mirkin, M. V.; Unwin, P. R.; Wipf, D. O. *Journal of Physical Chemistry* **1992**, *96*, 1861-1868.

(27) Wang, J.; Swain, G.M; *Unpublished research* **1999**.

CHAPTER 3

ELECTROCHEMICAL AND ATOMIC FORCE MICROSCOPY STUDIES OF METAL PHASE NUCLEATION AND GROWTH ON BORON-DOPED DIAMOND THIN-FILM ELECTRODES

3.1 Introduction

Electrochemical metal phase formation is a surface sensitive redox process which generally follows a nucleation-and-growth mechanism.[1] The shape, coverage and location of the initial metal deposits are influenced by the inherent rate of electron transfer and also by the physical, chemical and electronic properties of the electrode material.[2-4] Previous work in our laboratory has established the feasibility of electrodepositing metals on the diamond.[5-7] In this Chapter, a review of some of the theoretical aspects of metal nucleation and growth is given along with some preliminary studies of metal phase formation on boron-doped diamond thin-film electrodes.

3.2. Theory of Metal Nucleation and Growth

Electrodeposition occurs by a process of nucleation and growth. Nuclei form at active sites on the electrode according to a nucleation rate law, and then grow via the incorporation of additional ions from the surrounding solution.[8] Metal electrodeposition takes place at electrode/electrolyte interfaces under the influence of an electric field and involves solid phase formation.[9] Derek Pletcher in his book, "A First Course in Electrode Processes," explains the steps involved in the deposition of a metal onto an inert cathode.[10] These are depicted in Figure 3.1 (adapted from his book) and are: (i) transport of solvated metal ions through the solution to the electrode surface; (ii) electron transfer; (iii) partial or complete loss of the solvation sheath to form an adatom; (iv) surface diffusion of adatoms; (v) clustering of the adatoms to form a nucleus of sufficient size for it to be stable; and (vi) growth of the nucleus by incorporation of adatoms at favorable sites in the lattice structure of the metal.

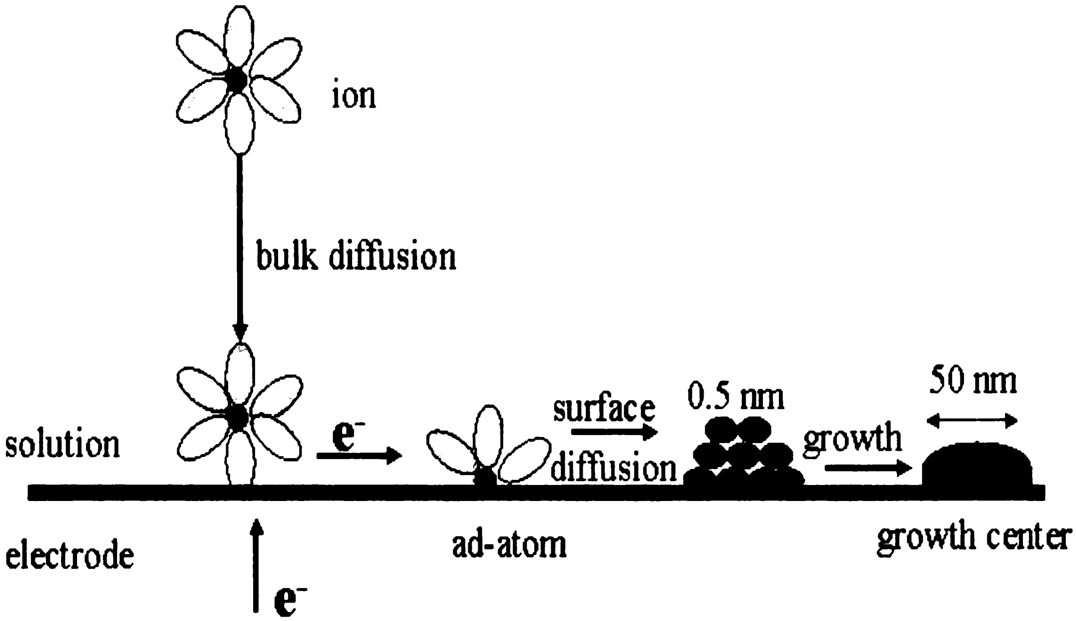

Figure 3.1 The stages in the formation of a stable, growing nucleus of a metal on a substrate of a different material such as carbon. (Adapted from reference 10)

Pletcher also explains the various stages in the deposition of a thick metal layer on an inert cathode. These have been pictorially described in Figure 3.2, for the case of progressive nucleation and three-dimensional growth. In the "progressive" nucleation model, new nuclei are formed with time at a given overpotential. Growth from these nuclei occurs and eventually the metal particles coalesce to form a continuous film.[11] As depicted in Figure 3.2, the deposition of a thick layer of metal is a multistep process and each of the processes could be the rate-determining step. An understanding of the metal nucleation and growth phenomenon on diamond is important for determination of the optimum experimental parameters for preconcentration in the ASV method, such as the overpotential and deposition time. Optimizing these parameters is important for improving the selectivity and sensitivity of the ASV method.

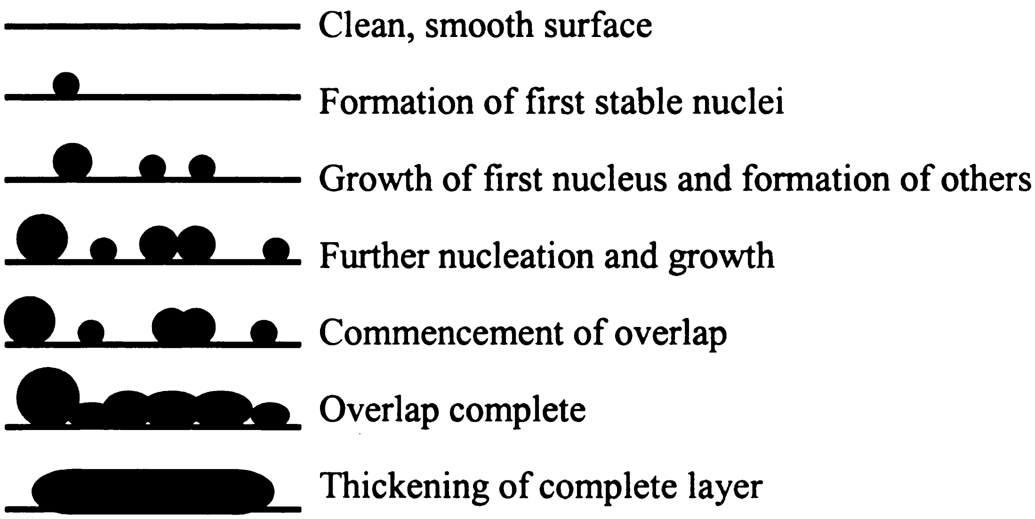

Figure 3.2 Deposition of a thick metal layer of metal on an inert cathode via a progressive nucleation and growth mechanism. (Adapted from reference 10)

Budevski, Staikov and Lorenz in their book, "Electrochemical Phase Formation and Growth," give a very nice introduction to the processes governing the initial stages of metal deposition.[12] Important factors which determine the mechanism of metal phase formation on a foreign substrate are the metal-substrate binding energy and the crystallographic misfit between the substrate and the 3D metal bulk deposit. They present two different growth models, which are illustrated in Figure 3.3. In the first case (Fig 3.3.A), the binding energy of the metal on a foreign substrate (Ψ_{Mads-S}) is lower than that of the metal on the native metal substrate (Ψ_{Mads-M}). In this case the overpotential deposition of 3D metal bulk phase takes place on an unmodified substrate surface according to the "Volmer-Weber" or 3D island growth mode, independent of crystallographic metal-substrate misfit.

In the second case, the binding energy of the metal on the foreign substrate ($\Psi_{Mads\text{-}S}$) is higher than that of the metal on the native metal substrate ($\Psi_{Mads\text{-}M}$). In this case, 2D metal phases can form in the underpotential range (i.e., potentials more positive of the $E^{o'}$) and the surface concentration of the adsorbed metal at $E_{M/M}{}^{Z+}$ can reach one or more monolayers depending upon $\Psi_{Mads\text{-}S}$. They describe two different sub-cases: (i) substances with negligibly small crystallographic misfit; 2D metal (underpotential deposition) and 3D metal crystallites are epitaxially oriented following a "layer-by-layer" growth mode (crystallographic misfit is characterized by the interatomic distances $d_{o,Me}$ and $d_{o,S}$ of 3D metal and substrate bulk phases, respectively, as shown in the Figure); and (ii) systems with significant crystallographic metal-substrate misfit; the formation and growth of unstrained 3D metal crystallites (islands) on top of strained 2D metal overlayers is energetically favored.

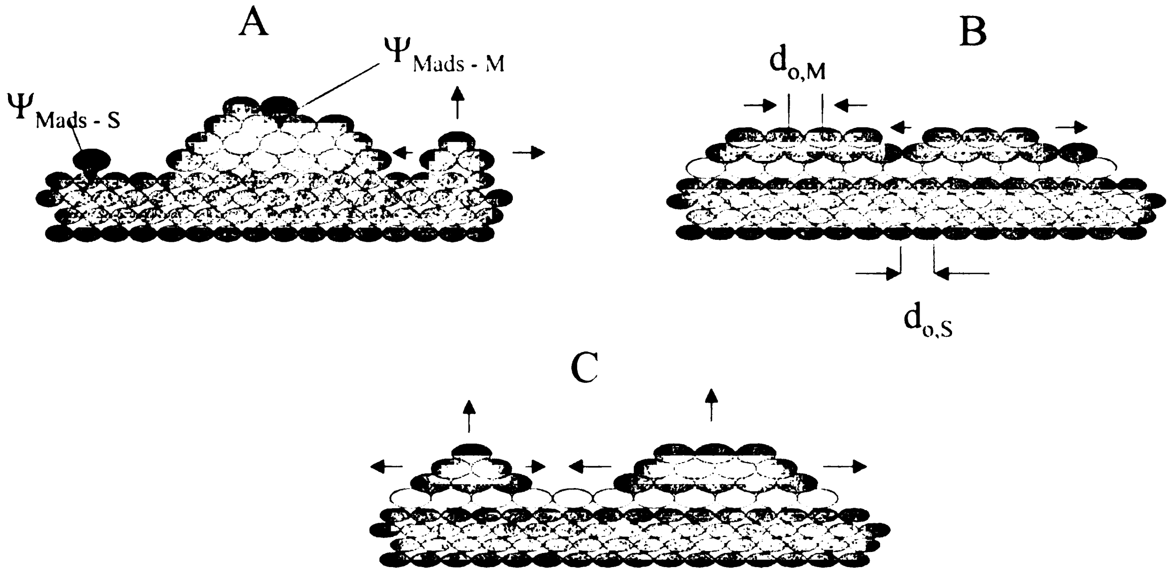

Figure 3.3 Schematic representation of different growth modes of metal deposition on foreign substrate (A) 3-D metal island formation (Volmer-Weber growth mode) $\Psi_{Mads} - S << \Psi_{Mads} - M$ (B) Metal layer by layer formation, $\Psi_{Mads} - S >> \Psi_{Mads} - M$ and ratio $d_{o,M} - d_{o,S} / d_{o,S} \approx 0$, (C) 3-D metal island formation on top of predeposited 2D metal overlayers on substrate, $\Psi_{Mads} - S >> \Psi M_{ads} - M$ and ratio $d_{o,M} - d_{o,S} / d_{o,S} > 0$ (positive misfit) or $d_{o,M} - d_{o,S} / d_{o,S} < 0$ (negative misfit). (Adapted from reference 12)

Apparent from experimental data presented in the remainder of the Chapter, the deposition of metal phases on boron-doped diamond electrodes occurs by the Volmer-Weber growth mode. The binding energy of the metal on diamond (Ψ_{Mads}-S) seems to be lower than that of the metal on the native metal substrate (Ψ_{Mads}-M). No underpotential deposition of any metal has been seen for diamond surfaces, consistent with weak deposit substrate interaction.[13] Similar observations were made by other researchers. For instance, Pitter et al. observed that the interaction of Ag with single-crystal boron-doped diamond was rather weak.[14] In fact, a procedure to entrap the metal particles into the surface microstructure is often needed to stabilize electrodeposited metal catalyst particles on diamond.[15]

3.3 Experimental

Chronoamperometric and Voltammetric Measurements. Most of the electrochemical measurements were made using a CHI 650a computerized potentiostat (CH Instruments Inc., Austin, TX) and a single compartment, three-electrode glass cell placed inside a Faraday cage for shielding. The electrolyte solution was 0.1 M acetate buffer, pH 4.5, unless otherwise specified. The other electrochemical parameters were as described in Chapter 2.

Chemicals. All solutions were prepared with ultrapure water (>17 MΩ-distilled, deionized and passed over activated carbon) from an E-pure water purification system (Barnstead). Silver nitrate (Fisher), cadmium nitrate (Aldrich), zinc acetate (Aldrich), cupric nitrate (Aldrich), and lead nitrate (Aldrich) were all reagent grade quality used without additional purification. 0.1 M acetate buffer was prepared by mixing appropriate amounts of 99% sodium acetate (Aldrich) and acetic acid (Aldrich) solutions. All glassware was cleaned by a three-step procedure: ethanol/ KOH bath, alconox/ ultrapure water solution, and ultrapure water rinse. The $CuSO_4 \cdot 5H_2O$ and H_2SO_4 used in the ECAFM measurements were ultrahigh purity grade (99.999%) (Aldrich). The electrochemical fluid cell was cleaned by a two-step sonication procedure that involved soaking in dilute alconox and in ultrapure water.

Electrochemical Atomic Force Microscopy (ECAFM). Experiments were conducted with a Nanoscope IIIa atomic force microscope (Digital Instruments Inc. and Veeco Metrology Group, Santa Barbara, CA) equipped with a 16 μm scanning head. The measurements were made in the contact mode. A standard AFM fluid cell equipped with a gold-coated spring clip and a pyramidal Si_3N_4 tip formed on a gold-coated 100 μm v-shaped silicon nitride cantilever (0.38 N/m spring constant) were used. The tip was held in an optically transparent holder in the fluid cell. The fluid cell was sealed with a special o-ring, obtained from the manufacturer, designed to minimize leaks due to its special concave shape. The exposed area of the electrode was 0.38 cm^2. The cell had tapered channels allowing for the injection of the solution and also placement of auxiliary and reference electrodes. Pt wire was used as the counter electrode and a piece of Ag wire was used as the quasi-reference electrode (QRE). All the images were obtained with 512 × 512 pixels. ECAFM images were obtained in either the constant force mode in which the tip height was adjusted via a feedback mechanism so as to maintain the force constant and or the constant height mode in which the tip height is constant so as to measure the force. A potentiostat was used to control the electrode potential during potential sweep or potential step measurements. The potential difference between the Ag QRE and an SCE reference electrode was – 27 mV in 1 M KCl. For convenience, all potentials are reported after being converted to the Ag/AgCl reference scale. A complete AFM image took approximately ca. 60 s to record. All measurements were made at room temperature, ~ 25 °C.

3.4 Results and Discussion

Cyclic voltammetry and chronoamperometry are useful for studying the nucleation and growth of metal phases. Potentiostatic transients at different potentials give experimental "current-time" relationships which can form the basis of evaluation of nucleation rate constants and particle number.

3.4.1 Metal Ion Voltammetry. Figure 3.4 shows a cyclic voltammetric i-E curve for 1 mM $CuSO_4$ in 50 mM H_2SO_4 at 100 mV/s. The curve for the last scan (total of five scans) is shown. Curves were recorded from potential sweep rates of 50 to 500 mV/s. A summary of the peak currents, peak potentials and the peak separations at these scan rates is given in Table 3.1. The difference in current magnitude between the current maximum and a baseline have been denoted by "i_p", peak currents. A baseline was manually drawn by extending the part of the curve before the current increase/decrease.

In Figure 3.4, the potential scan was begun at 400 mV and scanned in the negative direction, in this case at 100 mV/s. The recorded voltammetric i-E curve shows a cathodic current flow due to the reduction of the metal ion to the metal, beginning at – 96 mV. The cathodic current gradually increases due to the formation and growth of metal nuclei, as depicted in Figure 1.1, and finally reaches a maximum before decaying at more negative potentials due to a reduced flux of reactant species diffusing to the electrode surface. After reversal at – 500 mV, cathodic current continues to flow with a current crossover at -110 mV. This crossover is indicative of an overpotential for nucleation and growth on the bare diamond surface. In other words, it is energetically more favorable to form metal phases on existing metal than on the bare diamond surface. In summary, the voltammetric i-E curve exhibits the characteristic features of metal phase nucleation and growth, i.e., the large negative shift of the reduction peak potential and the current crossover during the reverse scan.

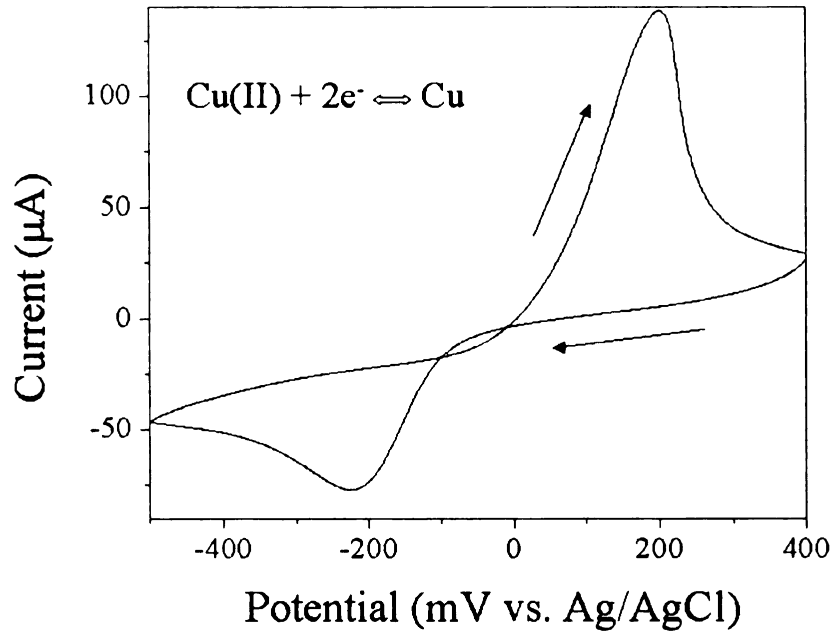

Figure 3.4 Cyclic voltammetric i-E curves for the reduction of 1 mM Cu(II) and subsequent oxidation at a microcrystalline diamond thin-film electrode. Scan rate = 100 mV/s. The redox reaction for the Cu/Cu(II) system is shown.

Table 3.1 Summary of the cyclic voltammetric peak currents, peak potentials and peak potential separations for the Cu(II)/Cu redox system at various scan rates for a microcrystalline diamond thin-film electrode.

	Onset reduction potential (mV)	I_p^{red} (μA)	I_p^{ox} (μA)	E_p^{red} (mV)	E_p^{ox} (mV)	ΔE_p (mV)
50 mV/s	-80	40	120	-193	178	413
100 mV/s	- 96	44	126	-229	203	432
200 mV/s	-110	47	135	-276	206	473
400 mV/s	-119	56	150	-296	214	510
500 mV/s	-121	58	158	-310	229	539

The overall reaction for the Cu(II) system has been cited as;[16]

$$\mathrm{Cu(II)} + 2e^- \Leftrightarrow \mathrm{Cu},\ E^o = 53\ \mathrm{mV\ vs.\ Ag/AgCl}$$

The reduction peak current for each electrode increased linearly with the square root of scan rate (Levich plot) over the range, $r^2 = 0.991$, suggestive of a diffusion controlled process. In contrast, the oxidation peak current increased rather linearly with scan rate indicative of a surface confined process ($r^2 = 0.994$). The onset reduction potential shifted negative with increasing scan rate indicating that the electron-transfer rate for metal ion reduction was less than the rate of the potential sweep.

Figure 3.5 shows the cyclic voltammetric i-E curves for 10 μm solutions of Pb(II), Zn(II), Cu(II) and Cd(II) in 0.1 M acetate buffer, pH 4.5, at 100 mV/s at a microcrystalline diamond thin-film electrode. The voltammograms exhibit features characteristic of metal nucleation and growth. Listed near each i-E curve is the experimental observed oxidation peak potential, E_p^{ox}, and the standard potential, $E^{o'}$, for the reaction. The standard potentials listed have been corrected for concentration (10 μm solutions) and are reported with respect to the Ag/AgCl reference electrode. Little overpotential is seen for the oxidation of the metal phases. This means that the oxidation reaction rate for each of the metal species is relatively fast. On the other hand, the onset potentials for metal phase formation are shifted more negative of the $E^{o'}$. The overpotential for the reduction reaction was, in general, larger than the overpotential for the oxidation reaction. In reality however, the oxidation potentials are observed to be within 100 - 150 mV of the theoretical potential. Diamond consists of certain defect sites and grain boundaries where the nucleation of the metal is favored. Further as shown in

Chapter 2, the surface of diamond consists of regions of different electrical conductivity or electrochemical activity. The non uniform conductivity of the surface and the difficult nucleation can both contribute to the initial deposition overpotentials.[13] Microscopy revealed the metal phases form in isolated islands of 3-D growth. Overall, the fact that good activity for metal deposition and oxidation (stripping) reactions is observed with modest overpotentials (ca. 100 mV) for diamond electrodes demonstrates its potential for use in metal analysis.

Berzins and Delahay derived equations for the voltammograms in the case of reversible metal deposition on a solid electrode.[17] The peak current was given as:

$$i_p^{ox} = 367\ n^{3/2} A D_o^{1/2} \upsilon^{1/2} C_o^* \qquad (3.1)$$

where, n is the number of electrons transferred in the reaction, A is the electrode surface area, D_o is the diffusion coefficient of the ion, υ is the scan rate and C_o^* is the bulk solution concentration of the metal ion. The experimental correlations of the values of i_p^{ox} with the above equation tended to be relatively poor (> 20% error) for Ag(I) and Cd(II). This could be due to a disparity in the value of D (literature values were used), uncertainty about the area term in the expression and or surface phenomenon at the electrode.

An example of a surface phenomenon could be the incomplete stripping of deposited metal from the surface of the electrode. Vinokur et al. and also Hyde et al. observed the incomplete stripping of Ag from the surface of boron-doped diamond electrodes.[13, 18] One possible reason cited by the Vinokur group was the model of "undercutting", initially proposed by Adzic and co-workers.[19] "Undercutting" is the phenomenon of faster dissolution of metal grains closer to the electrode surface, cutting off electrical contact with the rest of the deposited Ag, which would therefore not contribute to the oxidation current.

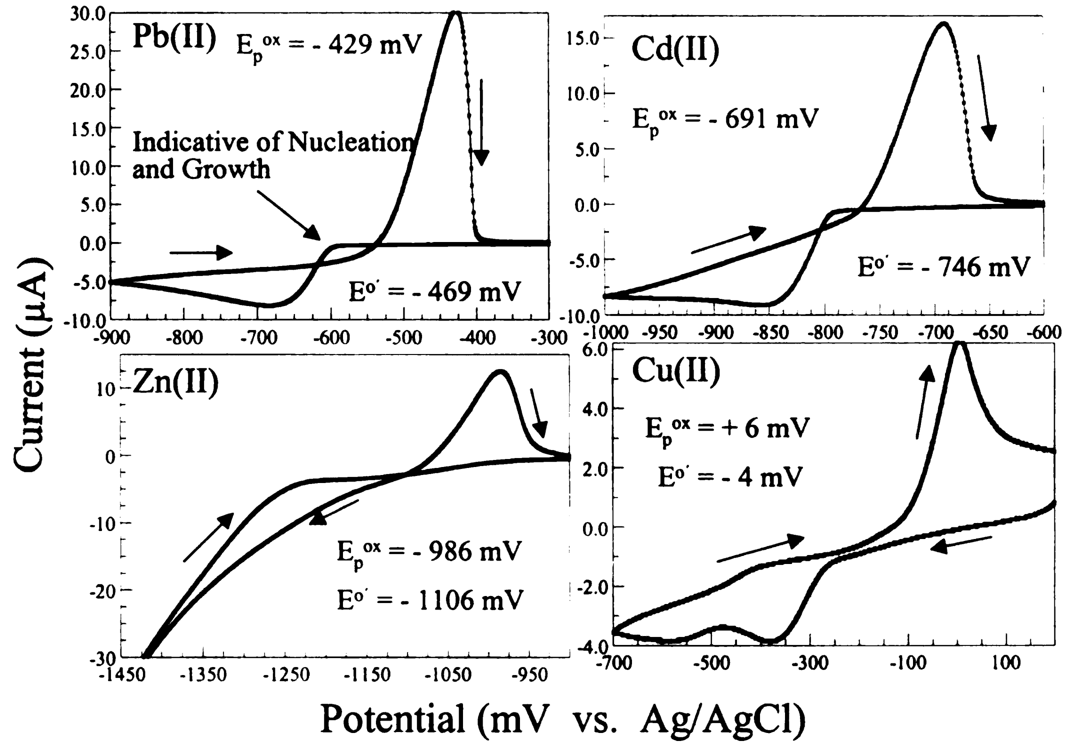

Figure 3.5 Cyclic voltammetric i-E curves for 10 µm solutions of Pb(II), Cu(II), Cd(II) and Zn(II) at a microcrystalline thin-film diamond thin-film electrode. The metals deposit and oxidize off near their standard reduction potentials. Scan rate = 100 mV/s, supporting electrolyte = 0.1 M acetate buffer, pH 4.5.

3.4.2 Chronocoulometric Measurements.

Double potential-step chronocoulometric measurements were conducted to determine if complete oxidation (stripping) of deposited Ag occurred from the electrode surface. 50, 250 and 1000 ppb of Ag(I) solutions in 0.1 M acetate buffer were studied. The potential at the working electrode was held for 5 s each, at 0 V to deposit the Ag from solution and then at 0.6 V to oxidize the metal deposit. Summary of the results for both types of diamond have been presented in Table 3.2. The ratio of background corrected charge for oxidation (Q_p^{ox}) and reduction (Q_p^{red}) are presented. It is observed that in all cases Q_p^{ox} is less than Q_p^{red} with an average ratio of 0.76 ± 0.05. This indicates incomplete stripping of Ag from the surface of the diamond. Vinokur et al. and also Hyde et al. have observed the incomplete stripping of Ag from the surface of boron-doped diamond electrodes.[13, 18] One possible reason attributed for this observation by the Vinokur group was the model of "undercutting" as discussed in Section 3.4.1. Another reason for incomplete stripping is speculated to be the non-uniformity of the electrode surface, due to which metal nuclei preferentially localize to active sites such as grain boundaries.[20] During the positive potential step, dissolution from these sites may be occurring at lower applied electrical field.

A clear trend of dependence of stripping efficiency on the concentration of the metal ions in solution was not observed, although the stripping efficiency at the nanocrystalline diamond was slightly higher at the lower concentration. Further, the efficiency of oxidation of the metal from the electrode surface was slightly higher on the microcrystalline diamond. This could have resulted from the greater microstructural homogeneity (as discussed in Chapter 2) of the microcrystalline diamond.

Table 3.2 Chronocoulometric charge data for the deposition and stripping of Ag from a Ag(I) solution in 0.1 M acetate buffer, pH 4.5. Potential steps from 0.6 to 0 to 0.6 V were applied for 5 s each to diamond electrodes of two different morphologies.

	Ratio: Q_p^{ox}/ Q_p^{red}	
Ag(I) Concentration	Microcrystalline diamond	Nanocrystalline diamond
50 ppb	0.81 ± 0.11	0.77 ± 0.10
250 ppb	0.76 ± 0.09	0.70 ± 0.08
1000 ppb	0.80 ± 0.09	0.70 ± 0.05

3.4.3 Metal Ion Chronoamperometric Measurements.

As discussed above, the early stages of electrochemical phase transformations often involve a 3-D nucleation process on boron-doped diamond electrodes. The rate of formation and the number of nuclei formed are dependent on the overpotential applied. Due to the fast charge-transfer step, the rates of growth of mature nuclei can be subsequently described in terms of control by mass-transfer of reactant metal to the growth centers. Three-dimensional nucleation/growth processes have been described in different theoretical models.[21, 22] The nucleation kinetic parameters, A (nucleation rate constant per site) and N_0 (number density of active sites over the substrate surface), can be estimated. The growth is best described in terms of localized diffusion to small spheres of (assumed to be so) nuclei. At early times in the nucleation event, hemispherical diffusion zones develop around and extend outward from each nuclei. The thickness of the diffusion zone is given by:

$$\delta_t=(kDt)^{1/2} \qquad (3.1)$$

Where δ_t (cm) is the diffusion zone thickness; k is a constant; and D is the diffusion coefficient (cm^2/s) of the reacting species. As the radius of the growth centers increase, the hemispherical diffusion zones for the nuclei begin to overlap. Therefore, the flux of reactant decreases and eventually the primary direction of reactant flux is normal to the surface. The corresponding diffusion path can then be expressed in terms of semi-infinite linear diffusion toward a fraction of the electrode surface. These relationships have been pictorially depicted in Figure 3.6. Such three-dimensional nucleation and growth has been described by different theoretical models as proposed by Hills et al., and Scharifker and Mostany.

Hills et al., classify nucleation as either "instantaneous" in which rapid nucleation takes place on a fix number of active sites, or "progressive" in which the number of nuclei increases with time and the number of active sites available for nucleation are considered to be virtually infinite. It should be noted that these are limiting cases. In the present work, these two limiting models were used to analyze the experimental results.

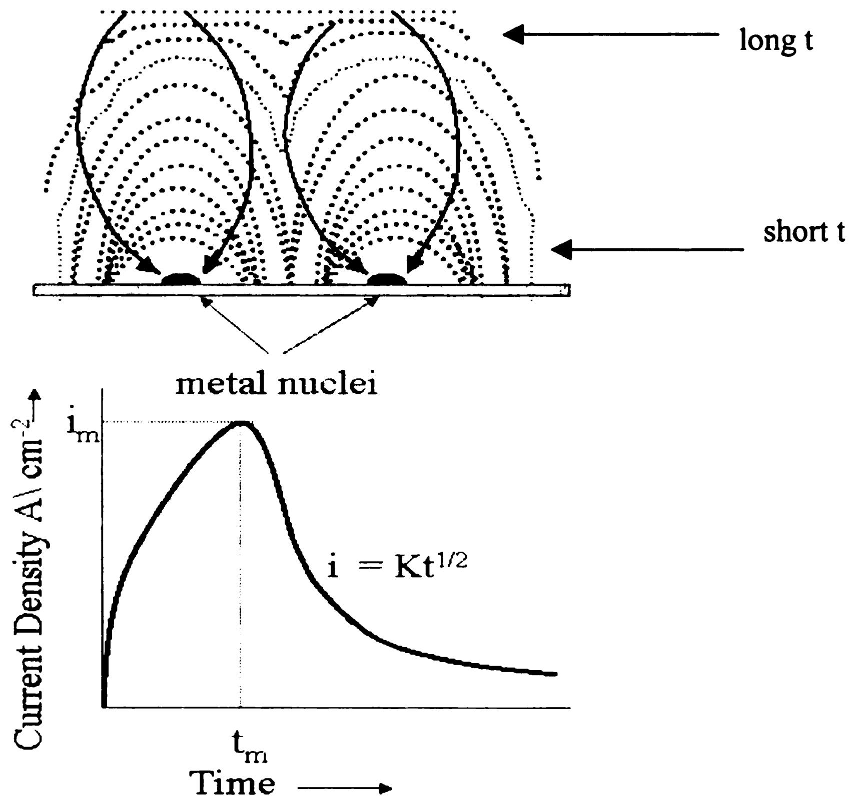

Figure 3.6 (A) Schematic diagram of the time-dependent growth of diffusion zones around forming metal nuclei on an electrode surface and their eventual overlap. The arrows indicate the directions of the diffusion fields during the growth of nuclei. (B) Expected current transient; K is constant given by $nFAD_o^{1/2}C_o^*/\pi^{1/2}$, the terms have their usual meanings.

Single-step chronoamperometric measurements were performed to investigate the metal nucleation growth process on diamond electrode surfaces.[23] Figure 3.7 presents a set of current-time transients recorded during the formation of Cu deposits on a microcrystalline diamond thin-film electrode from a solution of 1 mM $CuSO_4$ in 50 mM H_2SO_4. The measurements were performed by stepping the potential from 500 mV, where Cu(II) is stable, to different final potentials (-400, -500, -600 and –700 mV) past the $E^{o'}$. These potentials were sufficiently cathodic to induce nucleation and subsequent crystallite growth. The working electrode was kept at a positive potential of 0.6 V for 3 min after every potential step to completely oxidize the copper deposits. Transients obtained by stepping the potential to – 400 and –700 mV have been shown in the Figure, along with the theoretical curves (the cases for instantaneous and progressive nucleation). The plots are presented in dimensionless units, $(i/i_M)^2$ vs. t/t_M, facilitating comparison with the behavior predicted for each of these limiting nucleation mechanisms.

The current initially increases as a result of the formation of stable nuclei and growth of the metal deposits. The rising current eventually terminates in a broad maximum (i_M) as the individual hemispherical diffusion zones of the growing crystallites coalesce and give way to linear diffusion to a planar surface. After i_M has been reached, the current decays at a $t^{-1/2}$ rate predicted from the Cottrell equation, due to the formation of a depletion layer in the solution phase adjacent to the electrode that grows in thickness as a function of time.

As mentioned, the theoretical curves were constructed by plotting $(i/i_m)^2$ vs. t/t_m. At first the nucleation process was classified as "instantaneous" or "progressive". The expressions presented in non-dimensional form by plotting $(i/i_M)^2$ vs. t/t_M, for instantaneous (3.2) and progressive (3.3) nucleation are [8, 9]

$$(i/i_M)^2=1.9542(t_M/t)\{1-\exp[-1.2564(t/t_M)]\}^2 \qquad (3.2)$$

$$(i/i_M)^2=1.2254(t_M/t)\{1-\exp[-2.3367(t/t_M)^2]\}^2 \qquad (3.3)$$

The experimental data did not exactly fit the theoretical current transients, however, the nucleation of Cu on microcrystalline diamond appears to more closely track, the transient for progressive nucleation. The reason for the discrepancy in the experimental and theoretical curves maybe the fact that the diagnostic criteria for distinguishing between extreme cases of progressive and instantaneous nucleation they do not contain parameters related to physical or chemical properties of the system, such as molar volume, concentration, diffusion coefficient or kinetic constants.[23, 24]

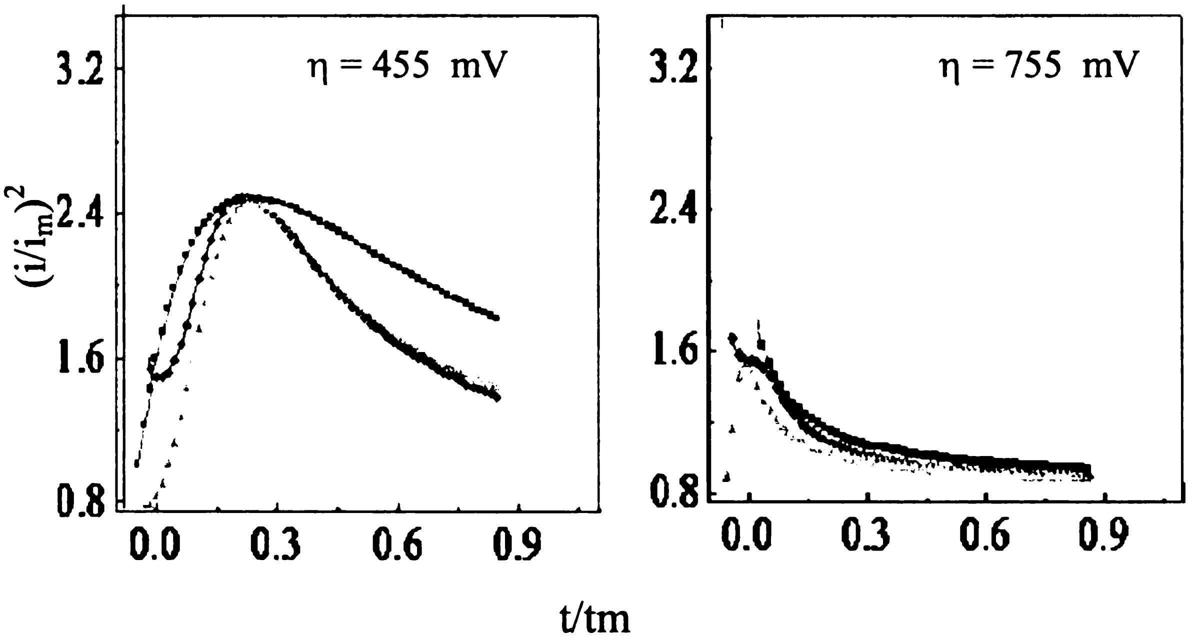

Figure 3.7 Comparison of experimental current-time transients with the theoretical transients corresponding to instantaneous and progressive nucleation at different overpotentials.

Once established that the nucleation is progressive at high supersaturation, the product AN_0 that defines the steady-state nucleation rate over the entire surface, was calculated from the current maxima, by means of the following equations,

$$t_m = (4.6733/ AN_0\pi kD)^{1/2} \text{ and } i_m = 0.4615zFD^{3/4}c(AN_0k)^{1/4} \qquad (3.4)$$

where D is the diffusion coefficient, zF the molar charge of the electrodepositing species and k is a numerical constant given by,

$$k = (8\pi cM/\rho)^{1/2} \qquad (3.5)$$

where M and ρ are the molecular weight and the density of deposited material, respectively. The values obtained appear in Table 3.3.

Table 3.3 Current-time transient data for copper electrodeposition on microcrystalline diamond.

$-\eta$(mV) (E – E^o)	i_m (mA.cm^{-2})	t_m(s)	N_o(cm^{-2})	A (s^{-1})
455	1.17	0.099	1.45×10^7	23.6
555	1.61	0.06	2.38×10^7	38.6
655	1.91	0.04	3.57×10^7	58.2
755	2.33	0.02	7.15×10^7	117

$D = 2.5 \times 10^{-5}$ cm^2/s. $E^{o'} = 55$ mV.

In all cases, the reaction rate, reflected by the current maximum, i_m, both of which increased with applied overpotential, whereas t_m decreased. In other words, the time required for the coalescence of the hemispherical diffusion zone for each mature nuclei, decreased with overpotential. This implies an increase in the number density of growth centers with overpotentials. The observation is consistent with the fact that the number density of sites, N_o and the rate constant, A, increases with overpotential. The electrodeposition of copper on boron-doped microcrystalline diamond films at these conditions is potential dependent and progressive in nature on microcrystalline diamond.

3.4.4 EC-AFM Study of Copper Deposition.

Electrochemical-atomic force microscopy (EC-AFM) was used to monitor copper electrodeposition on boron-doped, polycrystalline diamond thin-film electrodes with respect to time and overpotential. EC-AFM studies of copper stripping/deposition reactions on boron-doped diamond thin-film electrodes under potentiostatic control in solutions of different ability complexing ability such as sulfates and phosphates, have been previously reported.[25] The method proved useful for revealing the nucleation state and the early stages of complex formation when cations were released from the deposited metal.

Figures 3.8 and 3.9 show height mode images (5 × 5 μm) collected during copper deposition on microcrystalline diamond from a 50 ppm $CuSO_4$ in 0.1 M acetate buffer. The images were collected at the various overpotentials (vs. Ag/AgCl) and times as indicated. Images in Figure 3.8 were collected by stepping the potential from + 600 mV to the particular cathodic value indicated for ~ 60 s and then back to + 600 mV. The potential was then held at + 600 mV for at least 3 min. Multiple images collected at + 600 mV verified that the metal deposits were completely oxidized from the electrode surface. From Figure 3.8, new nuclei are observed to form with increasing overpotentials. Metal particles form at both the crystal facets and crystalline grains boundaries and defects. The greatest densities of particles seems to be present at the grain boundaries at lower overpotentials. The particles formed on the crystalline facets increase in number at the higher overpotentials. Notice the particle formed on the grain facet indicated by the arrow at the overpotential of – 866 mV. The growth on the facet surfaces initiates at defect sites. Another important factor with diamond in terms of location of the metal deposits is the local film conductivity.

In related work, Enea et al. electrochemically deposited Pt particles onto boron-doped (1 ppm of trimethyl boron in the source gas) diamond thin-films. Their study of the morphology and dispersion of Pt deposits by AFM (air, tapping mode) proved the existence of a small number of preferential diamond sites on which the Pt particles initially formed.[26] They reasoned that the behavior resulted from the higher electrical conductivity in some regions relative to others, presumably due to differences in boron-doping levels. From a manual count of the metal particles in multiple images, the particle density is estimated to be in the range of 6.0×10^{7} to 1.0×10^{8} cm^{-2}. The number of particles formed increased with the overpotential. These observations are also consistent with a progressive nucleation and growth mechanism. The particles broadly range in size from ~ 100 to 250 nm.

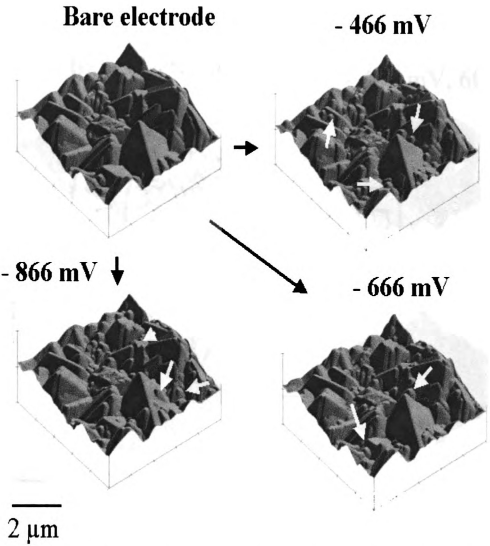

Figure 3.8 ECAFM images (height mode, 5 µm × 5 µm) collected during Cu deposition on microcrystalline diamond from a 50 ppm $CuSO_4$/0.1 M acetate buffer solution at different cathodic overpotentials. Arrows indicate the formation of new nuclei.

Figure 3.9 shows the ECAFM images (height mode, 5 μm × 5 μm) collected during copper deposition on microcrystalline diamond at one overpotential for various times. From a manual count, the particles density is in the range of 8.0×10^7 to 1.0×10^8 cm^{-2}. The particles broadly range in size from ~ 100 to 320 nm. The nucleation looks to be largely progressive as new nuclei are formed with time. The time dependent formation of nuclei is consistent with a progressive nucleation and growth mechanism.

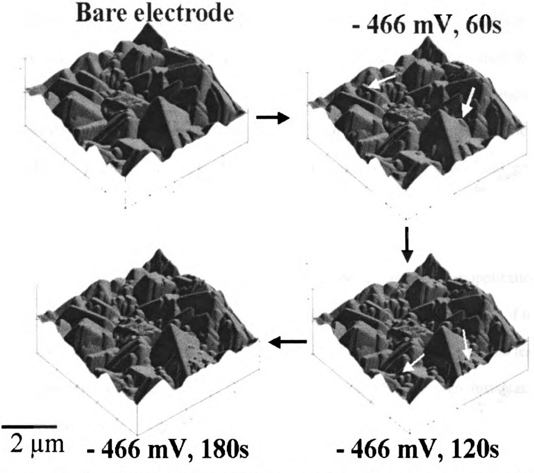

Figure 3.9 EC-AFM images (height mode, 5 μm × 5 μm) collected during Cu deposition on microcrystalline diamond from a 50 ppm $CuSO_4$ /0.1 M acetate buffer solution at various times at a fixed overpotential. Arrows indicate the formation of new nuclei.

3.5 Conclusions

The Chapter describes the theoretical aspects of the metal nucleation and growth on solid electrodes. Results from cyclic voltammetric, chronoamperometric and EC-AFM measurements demonstrated how these methods are useful for both the quantitative and qualitative study of the mechanisms governing metal phase formation on diamond. The experimental data reveal that the deposition of metal phases on boron-doped diamond electrodes occurs by the Volmer-Weber growth mode. No underpotential deposition of metal was observed for diamond, indicating a weak metal phase-substrate interaction. The analysis of current transients, under the framework proposed by Scharifker and Montany, was particularly useful since it allowed the determination of the values for the nucleation rate, A, and number density of nuclei, N_o, for Cu deposition on microcrystalline diamond. Results from cyclic voltammetric, chronoamperometric and EC-AFM measurements all are consistent with a progressive nucleation and growth mechanism.

Understanding metal phase formation on diamond is important for application of this new electrode in ASV. For instance, one ideally desires a high distribution of metal particles on diamond with a small and uniform particle size for ASV. This should lead to more narrow and intense oxidation and stripping peaks. Therefore, an instantaneous nucleation and growth mechanism would be ideal. As will be discussed in Chapters 5 and 6, the stripping peaks for Cu and the other metals are rather broad. This is presumably, due, in part to the fact that, at least for Cu, metal phase formation on diamond occurs via a progressive nucleation and growth mechanism.

3.6 References

(1) Henry, C. R. *Crystal Research and Technology* **1998,** *33,* 1119-1140.

(2) Gunawardena, G.; Hills, G.; Montenegro, I.; Scharifker, B. *Journal of Electroanalytical Chemistry and Interfacial Electrochemistry* **1982,** *138,* 225-239.

(3) Gunawardena, G.; Hills, G.; Montenegro, I. *Journal of Electroanalytical Chemistry and Interfacial Electrochemistry* **1982,** *138,* 241-254.

(4) Gunawardena, G.; Hills, G.; Montenegro, I.; Scharifker, B. *Journal of Electroanalytical Chemistry and Interfacial Electrochemistry* **1982,** *138,* 255-271.

(5) Wang, J.; Swain, G. M.; Tachibana, T.; Kobashi, K. *Journal of New Materials for Electrochemical Systems* **2000,** *3,* 75-82.

(6) Swain, G. M.; Wang, J. In *U.S. Pat. Appl. Publ.*; (Board of Trustees of Michigan State University, USA). Us, 2004, pp 13 pp.

(7) Awada, M.; Strojek, J. W.; Swain, G. M. *Journal of the Electrochemical Society* **1995,** *142,* L42-L45.

(8) Hyde, M. E.; Compton, R. G. *Journal of Electroanalytical Chemistry* **2003,** *549,* 1-12.

(9) Budevski, E.; Staikov, G.; Lorenz, W. J. *Electrochimica Acta* **2000,** *45,* 2559-2574.

(10) Pletcher, D., Ed. *First Course in Electrode Processes*; Alresford Press Ltd.: Alesford, Hants, Great Britain, 1991

(11) Abyaneh, M. Y. *Journal of the Electrochemical Society* **2004,** *151,* C737-C742.

(12) Budevski, E.; Staikov, G.; Lorenz, W. J.; Editors, Eds. *Electrochemical Phase Formation and Growth: An Introduction to the Initial Stages of Metal Deposition,* 1996

(13) Vinokur, N.; Miller, B.; Avyigal, Y.; Kalish, R. *Journal of the Electrochemical Society* **1999**, *146*, 125-130.

(14) Pitter, M.; Hugenschmidt, M. B.; Behm, R. J. *Applied Physics Letters* **1996**, *69*, 4035-4037.

(15) Wang, J.; Swain, G. M. *Journal of the Electrochemical Society* **2003**, *150*, E24-E32.

(16) A.J.Bard; L.R.Faulkner, Eds. *Electrochemical Methods, Fundamentals and Applications,*; John Wiley and sons, Inc: New York, 2001

(17) Berzins, T.; Delahay, P. *Journal of the American Chemical Society* **1953**, *75*, 555-559.

(18) Hyde, M. E.; Jacobs, R. M. J.; Compton, R. G. *Journal of Electroanalytical Chemistry* **2004**, *562*, 61-72.

(19) Adzic, G. D.; Drazic, D. M.; Despic, A. R. *Journal of Electroanalytical Chemistry and Interfacial Electrochemistry* **1988**, *239*, 107-111.

(20) Holt, K. B.; Bard, A. J.; Show, Y.; Swain, G. M. *Journal of Physical Chemistry B* **2004**, *108*, 15117-15127.

(21) Pitter, M.; Hugenschmidt, M. B.; Behm, R. J. *Applied Physics Letters* **1996**, *68*, 2508-2510.

(22) Scharifker, B.; Hill, G. *Electrochimica Acta* **1983**, *28*, 879-889.

(23) Wang, J. Dissertation, Michigan State University *Fabrication, characterization, and electrocatalyticactivity of metal/diamond composite electrodes,*2002.

(24) Palomar-Pardave, M.; Ramirez, M. T.; Gonzalez, I.; Serruya, A.; Scharifker, B. R. *Journal of the Electrochemical Society* **1996**, *143*, 1551-1558.

(25) Zak, J.; Kolodziej-Sadlok, M. *Electrochimica Acta* **2000**, *45*, 2803-2813.

(26) Enea, O.; Riedo, B.; Dietler, G. *Nano Letters* **2002,** *2*, 241-244.

CHAPTER 4

ANODIC STRIPPING VOLTAMMETRIC DETECTION OF TRACE METAL IONS: A PERFORMANCE COMPARISON OF BORON-DOPED DIAMOND THIN-FILM ELECTRODES AND SOME COMMONLY USED ELECTRODE MATERIALS

4.1 Introduction

The use of two different types of boron-doped diamond thin-film electrodes for the anodic stripping voltammetric detection of trace metal ions is described in this Chapter. Both microcrystalline and nanocrystalline morphologies were studied. Comparison of the two diamond electrode types revealed that both perform well for the detection of the metal ions and exhibit superb detection figures of merit. In general, the limit of quantitation was lower and the sensitivity was greater for nanocrystalline diamond. The nanocrystalline diamond morphology appears to aid in the formation of smaller metal particle sizes and higher particle densities during the deposition step. This leads to the improved figures of merit. Multielement analysis was also performed and the detection figures of merit are reported. There are some limitations with the use of diamond, specifically, interferences due to alloy and intermetallic compound formation between co-deposited metals. The response of diamond with bare and Hg-coated glassy carbon (GC) electrodes was compared. Scanning electron micrographs of the metal deposits, useful for the speculation about the nucleation and growth mechanism of each metal is presented.

4.2 Experimental

Diamond Film Deposition and Characterization of Metal Deposits. Boron-doped diamond thin films were deposited on p-type Si(100) substrates (~10^{-3} Ω-cm), using a commercial microwave-assisted chemical vapor deposition (CVD) system. Details regarding the growth conditions, as well as the follow-up material characterization, have been provided elsewhere and in Chapter 2.[1, 2] B_2H_6 was used for doping at a flow rate of 0.001 sccm (10 ppm). Scanning electron microscopy (JEOL-JSM-6400V) was used for imaging the metal deposits on the diamond surface.

Electrochemistry. Most of the electrochemical measurements were made using a CHI 650a or 900 - computerized potentiostat (CH Instruments Inc., Austin, TX) and a single compartment, three-electrode glass cell placed inside a Faraday cage for shielding. The diamond working electrode was pressed against a Viton® o-ring and clamped to the bottom of the cell. Either a bead of In/Ga alloy was placed on the backside of the scratched and cleaned substrate for ohmic contact or it was rubbed with a carbon rod. A graphite rod was used as the counter electrode and a Ag/AgCl electrode (3.5 M KCl) served as the reference ($E^0_{Ag/AgCl}$ = -0.045 V vs. SCE). The geometric area of the working electrode was ca. 0.163 cm^2. All measurements were made in solutions deoxygenated with nitrogen (99.99%) for at least 5 min. initially and then for 2 min after each anodic stripping or oxidation cycle. The solutions remained blanketed with the inert gas during a measurement. The electrolyte solution was 0.1 M acetate buffer, pH 4.5, unless otherwise stated. The reference electrode was placed inside a second cracked glass capillary (filled with the acetate buffer), which served as a double junction. All measurements were made in an unstirred solution. Typical differential pulse voltammetric settings were a 3 min deposition time, a 0.5 min "quiet" time at the deposition potential prior to initiation of the anodic sweep, a 100 mV pulse height, a 2 mV step height, a 100 msec pulse width (unless otherwise specified), a 100 msec cycle period, a 35 msec or less sampling time, and a constant potential of 600 mV for 120 s after completion of the anodic sweep to fully oxidize all metal deposits.

Prior to the deposition of the metal adlayer, the glassy carbon (Tokai, GC-30) was polished under very clean conditions using a series of alumina slurries (1.0, 0.3, and 0.05 μm). The electrode was rinsed and ultrasonicated with ultrapure water between each polishing step to remove polishing debris and clean the surface. For the comparison of diamond and Hg-coated GC, the concentration of $Hg(CH_3CO_2)_2$ in the Hg-containing solutions was 2×10^{-5} M. All the experiments comparing diamond and Hg-coated GC were conducted in acetate buffer of pH 5.2 with 30 ppm of Ca(II) and 5 ppm Mg(II) added. The geometric area of the working electrode was 0.222 cm^2. The other deposition and stripping conditions were same as above.

Chemicals. All solutions were prepared with ultrapure water (>17 MΩ-distilled, deionized and passed over activated carbon) from an E-pure water purification system (Barnstead). Silver nitrate (Fisher), cadmium nitrate (Aldrich), zinc acetate (Aldrich), cupric nitrate (Aldrich), lead nitrate (Aldrich) and mercuric acetate (Aldrich) were all reagent grade quality used without additional purification. 0.1 M acetate buffer was prepared by mixing appropriate amounts of 99% sodium acetate (Aldrich) and acetic acid

(Aldrich). All glassware was cleaned by a three-step procedure: ethanol/ KOH bath, alconox/ ultrapure water solution, and ultrapure water rinse. The glassware for the comparison of diamond and Hg-coated GC were cleaned by a three-step procedure consisting of: alconox/ ultrapure water solution, soaking for 10 min each in 1 M hydrochloric acid, and 1 M nitric acid, followed by ultrapure water rinse.

4.3 Results and Discussion

4.3.1 Comparison of Diamond and Glassy Carbon for the LSV Detection of Metal Ions. Comparison studies of the performance of microcrystalline diamond and GC were initially performed. A complete set of detection analytical figures of merit were obtained with both electrodes for three metal ions using linear sweep voltammetry (LSV): Ag(I), Cd(II) and Hg(II). Figure 4.1 shows the linear sweep voltammograms for the oxidation of Ag at microcrystalline diamond. The metal phase was formed at 0 V with a deposition time of 3 min. The peak current and charge increased with the solution concentration of Ag(I). The current rises sharply on the forward edge of the peak as the metal phase oxidizes. The peak then goes through a maximum followed by a slow decay on the trailing edge. This reflects diffusion of the oxidized metal ion away from the surface. As the concentration was increased from 0.001 to 1 mM, it was observed that E_p^{ox} for Ag shifted from 360 to 450 mV, for Cd from –700 to –610 mV and for Hg from 460 to 500 mV. The peak potential shifts positively because the surface coverage increases with increasing solution concentration and it takes longer to oxidize the metal deposits.[3] The limit of quantitation was found to be 107, 110 and 200 ppb for Ag(I),Cd(II) and Hg(II) respectively (S/N>3). Figure 4.1 also shows the log–log plots of ip^{ox} vs. the Ag(I) concentration at diamond. The plots were fairly linear, (BDD, r^2 = 0.985, 993, 0.939 and GC, r^2 = 0.998,0.9902, 0.977) for Ag(I), Cd(II) and Hg(II) respectively. It was found that plotting the peak charge (Q_p^{ox}) vs. the concentration generally gave better correlation coefficients and was used more frequently from this point on.

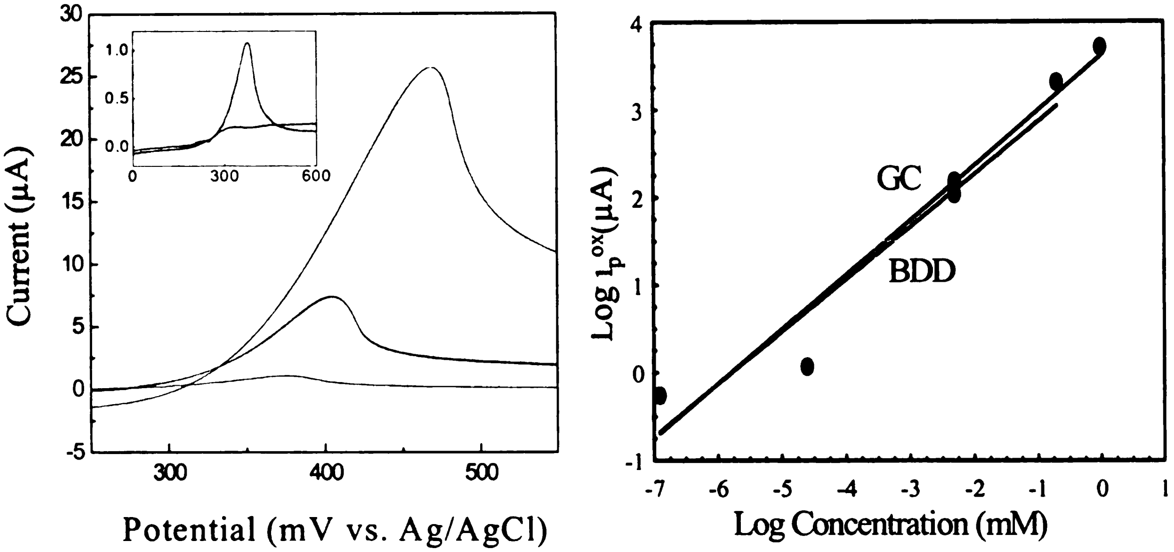

Figure 4.1 Linear sweep stripping voltammetric i-E curves for Ag(I) concentrations of 10 μM, 100 μM and 1 mM. Inset shows the i-E curves for the 1 and 10 μM Ag(I) concentrations. The solutions were prepared in 0.1 M acetate buffer, pH 4.5. The log-log current-concentration plots for the assays on BDD and GC are also presented.

Table 4.1 summarizes the analytical detection figures of merit for Ag(I), Cd(II) and Hg(II) for both electrodes. Microcrystalline diamond outperformed GC in terms of linear dynamic range, limit of quantitation, response precision and stability. The response precision was measured over 10 consecutive measurements of a 10 μM metal ion concentration. The response stability was measured over a three-day period with a total of 6 measurements of the solution of same concentration.

A reason for the superior performance of diamond could be the fact that these films exhibit voltammetric background currents and double-layer capacitances up to an order of magnitude lower than for glassy carbon.[4] The diamond surfaces are non-polar and relatively oxygen-free, with the surface carbon atoms terminated by hydrogen. Conversely, the GC surfaces are polar, with the exposed defect sites terminated by carbon-oxygen functionalities.[5] The surface carbon-oxygen functionalities promote strong dipole-dipole and ion-dipole interactions with polar and ionic molecules and the specific adsorption of electrolyte ions could occur. Another contributing factor may be a lower density of surface electronic states near the fermi level caused by the semimetal-semiconductor nature of boron-doped diamond. A lower surface charge carrier density at a given potential would lead to a reduced accumulation of counter-balancing ions and water dipoles on the solution side of the interface, thereby lowering the background current and capacitance.[6] Recently it has been proved that the diamond surface has "electrochemically active" sites separated by more insulating regions.[7] The reduced electrochemically active area of diamond would further account for low background currents observed.

Table 4.1 LSV analytical detection figures of merit for the detection of several metal ions at boron-doped microcrystalline diamond and glassy carbon electrodes.

	Microcrystalline Diamond			Glassy Carbon		
Parameter	Ag(I)	Cd(II)	Hg(II)	Ag(I)	Cd(II)	Hg(II)
Linear Dynamic Range, (mM)	0.001-1	0.001-1	0.001-1	0.01-1	0.001-1	0.01-1
Limit of Quantitation (S/N>3), (ppb)	107	112	200	1000	112	2000
Sensitivity, (μA/mM)	53	516	39	40	339	266
Precision, RSD, (%) (n = 10)	1.8	0.81	3.3	6.7	4.5	12
Stability, (%) (3 day test)	3.6	8.1	7.9	3.9	8.0	8.4

4.3.2 Comparison of Diamond and Hg-Film Electrodes for the DPASV Detection of Metal Ions

Awada et al. deposited Hg on polycrystalline diamond thin-films.[8] The Hg was deposited potentiostatically at –1.0 V vs. Ag/AgCl in a thin-layer flow cell during which time 5 injections (20 μL) of a 1 mM $Hg(CH_3CO_2)_2$ in 0.1 M sodium acetate buffer solution at pH 4.5 were made. The injections were carried out at a flow rate of 1.4 mL/min. A scanning electron micrograph of the Hg-coated diamond thin film (from their work) is presented in Figure 4.2. They observed that the Hg-film consists of individual droplets and tended to form spheres ranging from 0.5 to 3 μm on the surface of the electrode. Hg deposits on this diamond were found to be highly dispersed and existed almost exclusively at the intercrystalline grain boundaries between the larger diamond microcrystallites.

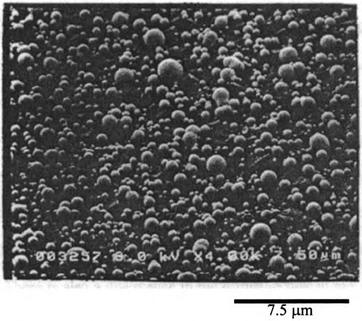

Figure 4.2 Electrochemically deposited Hg on the surface of a microcrystalline diamond thin-film electrode. The Hg tended to form spherical droplets on the substrate. (Adapted from reference 8)

The deposition and stripping process of metals from Hg electrodes is different from the metal nucleation and growth on a solid electrode. Foreign metals deposit within the Hg volume forming amalgams. On the other hand, foreign metals deposit as a metallic phase on solid electrodes. Figure 4.3 presents differential pulse anodic stripping voltammetric i-E curves for Cd at (A) nanocrystalline diamond and (B) Hg-deposited coated GC. The oxidation peak curents vary linearly from 10 to 1000 ppb for both electrodes. (r^2 = 0.997 and 0.994 for nanocrystalline diamond and Hg coated GC, respectively). The background noise is higher for the Hg-coated GC than for the nanocrystalline diamond. Typical values were 5.5 and 0.53 nA at E = - 750 mV, respectively. The increased noise is presumably due, in part, to the greater capacitance and more reactive surface of GC (electroinactive surface carbon-oxygen functionalities).

Further, the sensitivity is higher and the limit of quantitation (LOQ) slightly lower for the detection of Cd(II) at Hg-coated GC compared to the planar nanocrystalline diamond electrode. This can be explained due to the fact that the deposited metal is amalgamated within the individual drops of Hg. In considering the stripping of the metal from stationary Hg drop and film electrodes, the metal concentration in the Hg becomes important. A spherical correction term has to be applied to the Randles-Ševčík equation (used to describe the forward peak current for a reversible system using linear sweep voltammetry).[9] There is also a divergence in the diffusion flux in metal stripping from a drop electrode due to its spherical nature. The peak current is not proportional to the drop surface area as in the original Randles-Ševčík equation, but is proportional to the drop surface radius.[10] In general, the peak current increases with decreasing values of the drop radius and is proportional to the volume of Hg in the drop.

Peak potentials for the oxidation of Cd from the nanocrystalline film are observed to be more negative than those from Hg-coated GC. For instance at 100 ppb Cd(II), E_p^{ox} is observed to be -789 mV and -732 mV for nanocrystalline diamond and Hg-coated GC, respectively. A reason for this could be the fact that in the case of the amalgamated metal, the metal has to undergo diffusion to the surface of the Hg drop in order for it to be oxidized. This takes more time than in the case of the solid electrode where the deposited metal is readily available on the electrode surface. Also the recorded oxidation charge for metal oxidation from the diamond electrode is almost three times lower than the oxidation from Hg-coated GC, indicating a greater amount of total metal deposited inside the Hg droplet. The activity of the metal inside Hg is different from a pure metal phase. Therefore, the peak current for the oxidation of metal from the Hg-coated electrode appears at more positive potentials. The FWHM values of the peaks at the various concentrations for the Hg-coated GC were slightly lower (< 6 mV in most cases) than widths observed for nanocrystalline diamond. For instance at the 1000 ppb concentration, the FWHM for Hg-coated GC was 52 mV and for nanocrystalline diamond was 58 mV. However, the peaks were sharper at the Hg-coated GC surface, probably due to the more homogeneous nature of the surface (i.e., the Hg environment from which the metal was oxidizing).

In summary, the response of nanocrystalline diamond for Cd(II) was determined to be comparable to that of Hg-coated GC. Both electrode types yielded an analytically useful response for the metal ion. The sensitivity was higher for the Hg-coated GC and the limit of quantitation was slightly lower. On the other hand, the background current and noise were greater for Hg-coated GC.

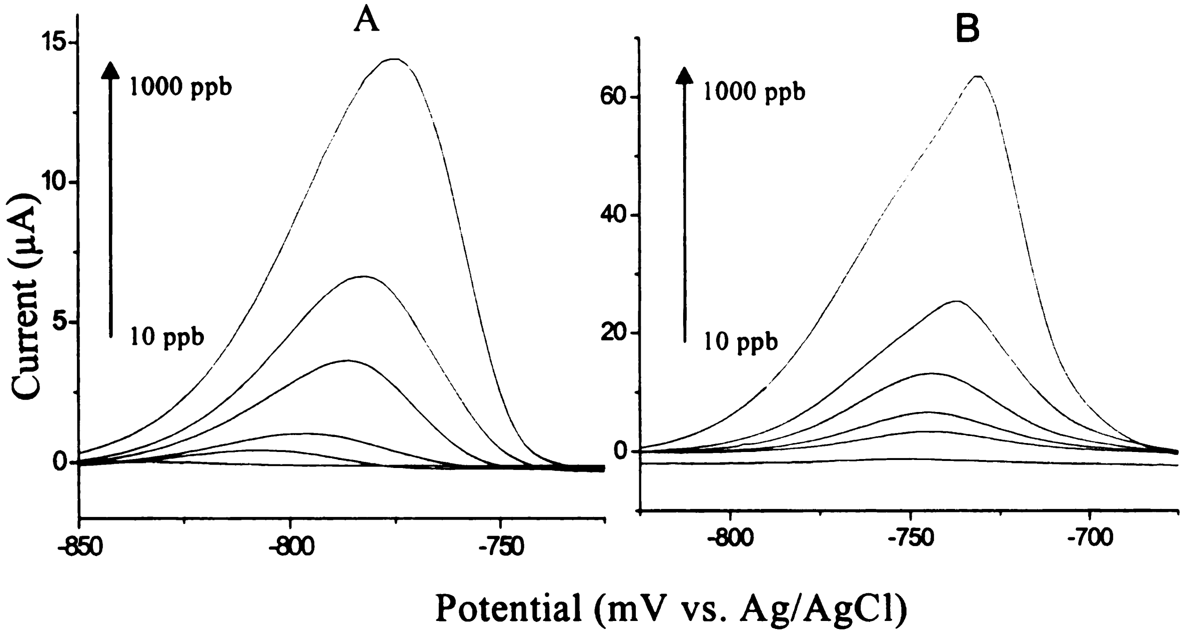

Figure 4.3 Differential pulse anodic stripping voltammetric (DPASV) i-E curves for standard solutions of Cd(II) ranging in concentration of 10 to 1000 ppb. The working electrodes were (A) nanocrystalline diamond and (B) Hg-coated GC. The supporting electrolyte was 0.1 M acetate buffer, pH 5.2. Deposition potential = -900 mV vs. Ag/AgCl. Deposition time = 3.5 min. The other DPASV conditions are described in experimental section. Geometric area = 0.222 cm^2. The peak areas were determined by integration between –700 mV and – 900 mV. (Data obtained by E.A. McGaw)

Table 4.2 Analytical detection figures of merit for the differential pulse anodic stripping voltammetric (DPASV) detection of the Cd(II) at a nanocrystalline diamond and Hg-coated GC electrodes. (Data obtained by E.A. McGaw)

Parameter	Cd(II)	
	Nanocrystalline Diamond	Hg-Coated GC
Background Signal (μA)	0.53	5.5
Limit of Quantitation (ppb) (S/N > 3)	5.0	1.0
Sensitivity (nA/ppb)	15	51
Linear Correlation Coefficient, r^2	0.997	0.994

4.3.3 Linear Sweep and Differential Pulse Voltammetry of the Individual Metals.

Figure 4.4 shows linear sweep stripping voltammetric i-E curves for 0.1 mM Cd in 0.1 M acetate buffer, pH 4.5 at a microcrystalline diamond electrode. The deposition time was varied from 30 to 180 s in 30 s increments. A linear dependence of the peak current with the time of deposition is observed ($r^2 = 1.00$). A similar trend was observed for both Ag and Hg ($r^2 = 0.997$ and 0.972, respectively). These results prove that the peak current increases in a proportional manner with the deposition time. A similar relationship was observed for the peak charge, Q_p^{ox}, and the time of deposition for all the three metal ions. The deposition time controls the amount of metal phase formed and therefore the oxidation response sensitivity. A lowering of the limit of quantitation can be achieved with longer deposition times.

In case of metallic films deposited on an inert solid electrode, the number of moles of metal, M, accumulated on the surface is given by:[11]

$$M = \frac{i_L t_d}{nF} \tag{4.1}$$

where, i_L is the limiting current for the deposition of the metal, F the Faraday, t_d the deposition time and n is the number of electrons transferred in the reaction. From the above relation the total amount of metal deposited on the solid electrode is a function of the total time of deposition, which in turn is related to the experimental peak current (equation 1.1).

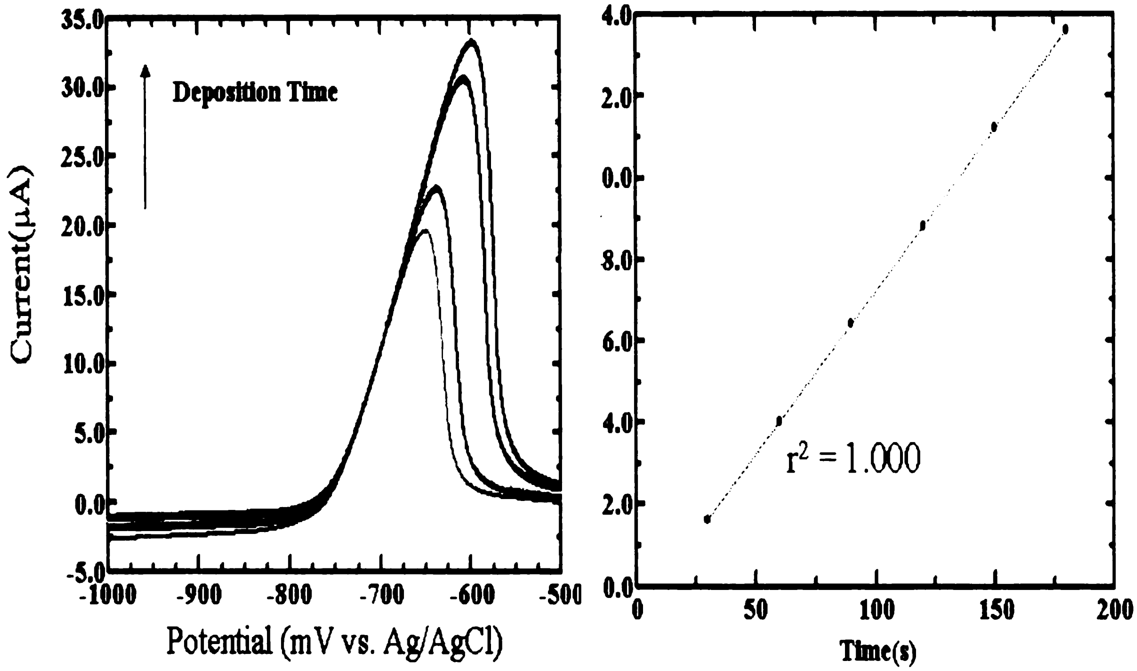

Figure 4.4 Linear sweep stripping voltammetric i-E curves for 0.1 mM Cd in 0.1 M acetate buffer, pH 4.5, at a microcrystalline diamond electrode, depicting the dependence of i_p^{ox} on deposition time. Deposition time was varied from 30 to 180 s (30 s increments). Deposition potential -1000 mV.

Figure 4.5 shows representative stripping voltammetric i-E curves for a 10 μM concentration of each metal ion at both microcrystalline and nanocrystalline diamond in 0.1 M acetate buffer, pH 4.5. All deposition and stripping conditions were maintained constant for the comparison. The curves reveal the complexity of metal deposition and stripping at diamond, as the stripping peak potential, current, charge and FWHM all very much depend on both the metal and the diamond film type. Metal deposition and stripping at diamond is more complex than the same processes at Hg-coated GC. For all the metals except Zn, the stripping peak width, FWHM, was slightly smaller for nanocrystalline diamond. This is consistent with a smaller nominal deposit size and narrower particle size distribution, as will be shown in scanning electron micrographs presented in Section 4.3.5. The i_p^{ox} and Q_p^{ox} values tended to be greater for nanocrystalline than for microcrystalline diamond. The same trends were observed at other metal ion concentrations of 100 and 1 μM. The greater peak current and charge for nanocrystalline diamond is consistent with more metal phase formation (preconcentration). There is also some variance in the E_p^{ox} values.

A summary of the analytical detection figures of merit for the five individual metal ions at both diamond types is presented in Table 4.3. Both electrodes exhibit a linear dynamic range of 4 to 5 orders of magnitude with a limit of quantitation in the low ppb range for all five metal ions. The limits of quantitation are generally lower for nanocrystalline than for microcrystalline diamond. Due to the morphological influences of the smaller grain size and higher fraction of grain boundary, a higher nucleation density and higher particle density is achieved on this surface. We are presently investigating the relative importance of the grain versus the grain boundaries in the metal nucleation and growth process. Except for Cu(II), the sensitivity for all the metal ions is slightly higher for nanocrystalline diamond. The coefficients of variation for all the metal ions are similar for both electrode types (1-4 %). The response precision was evaluated from 10 successive measurements of a 10 μM solution of each metal ion. The response stability was measured over a three-day period with a total of 6 runs of the same solution concentration. The sensitivity values were calculated from the slope of the charge vs. concentration plots and a minimum of five points was used in the statistical analysis.

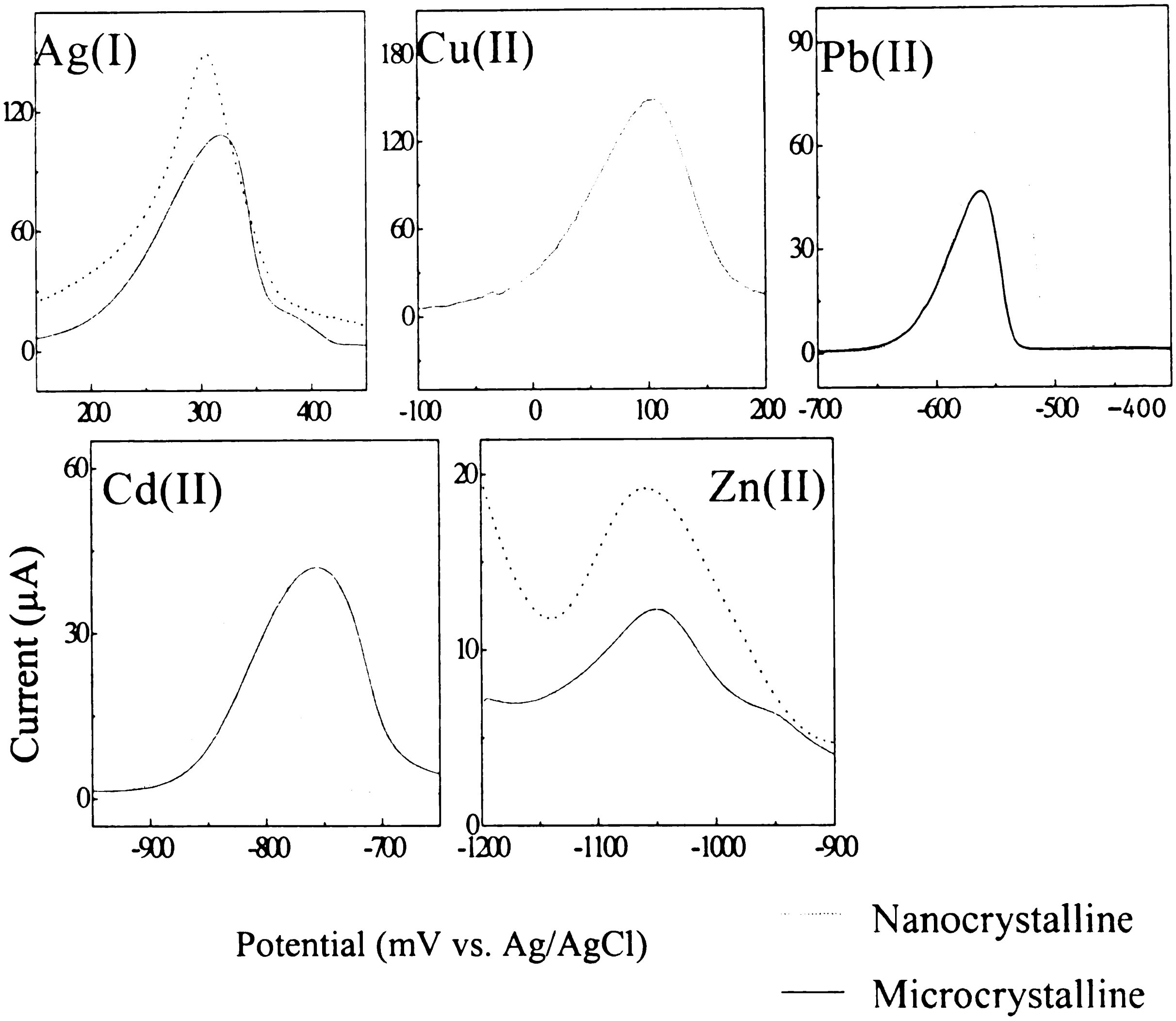

Figure 4.5 Representative differential pulse anodic stripping voltammetric (DPASV) i-E curves for a 10 μM concentration of each metal ion at both microcrystalline and nanocrystalline diamond thin-film electrodes. Supporting electrolyte = 0.1 M acetate buffer, pH 4.5.

The limit of quantitation is highest for Zn, and this is due, at least to some extent, to the hydrogen-evolution reaction interfering with the coulometric efficiency of the metal deposition. The stripping peak potential for each metal shifted positive with deposition of a metal from solutions of increasing metal ion concentration, consistent with an increased surface coverage. It, therefore, takes more time during the scan to completely oxidize the metal phase and the peak appears at more positive potentials. The response precision and stability of the measurement were generally < 5% for all the five metal ions tested at both diamond types.

Table 4.3 Summary of the differential pulse anodic stripping voltammetric (DPASV) detection figures of merit for the measurement of individual metal ions at microcrystalline (M) and nanocrystalline (N) diamond.

Parameter	Linear Dynamic Range(ppb) ($r^2 > 0.99$)		Limit of Quantitation (ppb)(S/N > 3)		Sensitivity (μC/ppb)		Response Precision (%)(n = 10)		Response Stability (%)(3 day test)	
Metal ion	M	N	M	N	M	N	M	N	M	N
Ag(I)	0.1-1000	0.1-10,000	0.11	0.11	0.098	0.111	1.1	0.91	2.6	3.7
Cu(II)	0.6-6400	0.6-6400	0.64	0.64	0.085	0.045	1.0	1.2	1.9	4.6
Pb(II)	20-20,000	2-20,000	20.1	2.07	0.045	0.050	1.6	0.41	2.9	1.7
Cd(II)	11-1100	1.1-11,000	11.2	1.12	0.072	0.099	0.7	1.2	4.6	3.9
Zn(II)	65-6500	6.5-6500	65.3	6.53	0.028	0.035	3.5	4.5	6.5	4.5

4.3.4 Differential Pulse Voltammetry of Mixtures of Metals Ions. The simultaneous analysis of three metal ions, Ag(I), Pb(II) and Cd(II) from a solution containing them all was investigated using nanocrystalline diamond.[2] Figure 4.6 shows the differential pulse anodic stripping voltammetric i-E curves for Ag, Pb and Cd for a boron-doped nanocrystalline diamond electrode in acetate buffer, pH 4.5. The concentration of the metal ions in each solution was (a) 5 (b) 1 (c) 0.5 (d) 0.1 μM. The deposition was performed at -1000 mV for 3 min. The peaks were identified by peak potential matching of the response for individual metal ions. The stripping peaks for the Cd, Pb, and Ag, deposited from 10 μM solution concentration, appear at -781 (106), -432(228), and 332 (116) mV. The FWHM values for each peak in mV are given in parentheses.

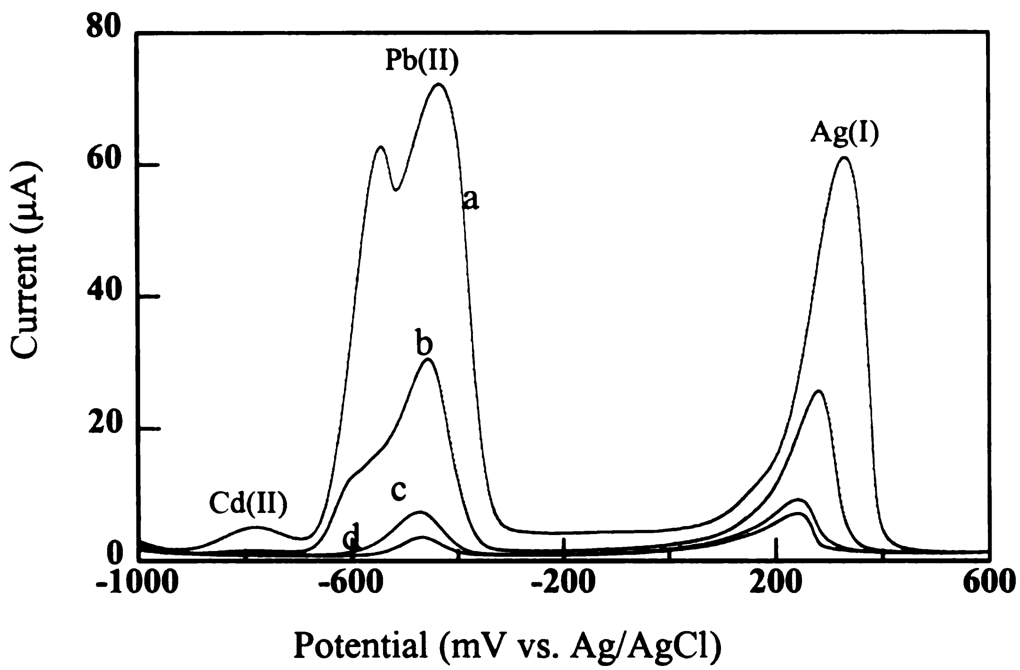

Figure 4.6 Differential pulse anodic stripping voltammetric (DPASV) i-E curves for Ag, Pb and Cd on boron-doped nanocrystalline diamond in acetate buffer, pH 4.5.The preconcentration was performed for 3.5 min. in quiescent solution at -1000 mV. The concentration of the metal ions in each solution was (a) 5 (b) 1 (c) 0.5 (d) 0.1 μM.

The stripping peaks all increased with the metal ion concentration in solution. The linear dynamic range for both electrodes was 4 to 5 orders of magnitude ($r^2 > 0.99$). The limit of quantitation for all three metal ions was 0.01 μM, or 1, 2 and 1 ppb for Cd(II), Pb(II) and Ag(I), respectively. The S/N ratio for Cd peak was 3 and for Ag and Pb was ca. 30 at this concentration. It can be seen that the Pb stripping peak formed a doublet when both Cd and Ag are co-deposited. In another series of experiments, it was observed that the standard additions of either Cu(II) or Ag(I) to a test solution containing just Pb(II) produced a Pb stripping peak doublet. Co-deposition of Cd or Zn did not influence the Pb peak. It was also observed that the Cd peak was suppressed in the mixture compared to the peak magnitude in the individual metal ion measurement. Experiments were conducted to ascertain the cause for the suppression. The addition of either Ag(I), Cu(II) or Pb(II) to the solution caused the suppression of the Cd peak. However, the effect was greatest with the addition of Ag(I). It seems from experiments involving standard additions of Cd(II) to the solution mixture that the ratio of Cd(II) to the rest of the metals ions is critical. At a ratio of 2:1, the ratio of the Cd stripping peak charge in the mixture to the peak charge for the individually stripped metal is approximately 1. When co-deposited with Cd, the stripping charge for Ag is enhanced suggesting that some of the deposited Cd is stripping at the Ag oxidation potential.[12]

Further, Figure 4.7 shows a example of a differential pulse anodic stripping voltammetric i-E curve for a mixture of Zn, Cd, Pb, Cu, and Ag at nanocrystalline diamond. The metal ion concentrations were all 10 μM. Quantifiable peaks are seen for Cd, Pb, Cu, and Ag. The peak for Zn is suppressed and is not distinguishable due to the intermetallic compound formation with Cu.[13-15] The peak for Cd is also suppressed, as observed in the three metal ion measurement. Further, at concentrations as low as 0.01 μM, the Ag peak also tended to form a doublet. The limit of quantitation of Ag(I) (S/N=7), Cu(II) (S/N=8), Pb(II) (S/N=3.2) and Cd(II) (S/N=3.1) in the mixture is 0.01

μM or 1, 0.6, 2 and 1 ppb, respectively. These data along with the other figures of merit for similar measurements using microcrystalline diamond are compiled in Table 4.4. The coefficients of variation for both kinds of diamond were generally less than 5 % for the mixture of these 5 metals. The stripping peaks for nanocrystalline diamond were observed at potentials 30-50 mV positive of those seen for microcrystalline diamond.

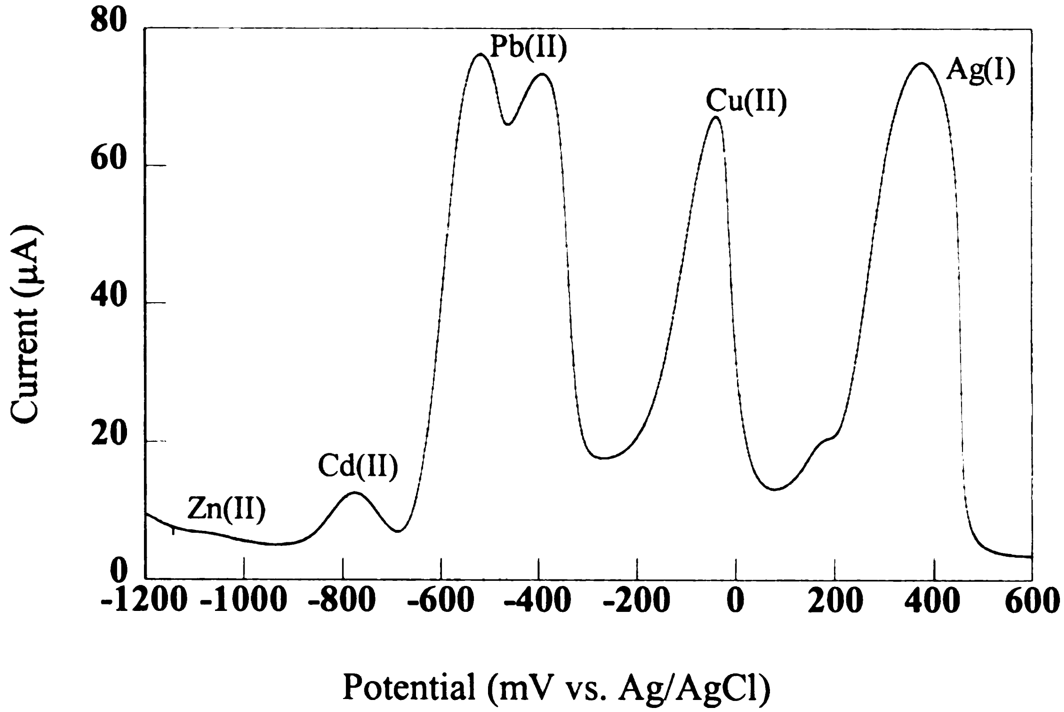

Figure 4.7 Differential pulse stripping voltammetric (DPASV) i-E curves for the detection of 10 μM solution concentrations of Ag, Cu, Pb, Cd and Zn for nanocrystalline diamond film in acetate buffer, pH 4.5.The preconcentration was carried out for 3.5 min in quiescent solution at -1200 mV.

Table 4.4 Summary of the differential pulse anodic stripping voltammetric detection figures of merit for mixtures of metal ions at microcrystalline (M) and nanocrystalline (N) diamond.

Metal	Linear Dynamic Range(ppb) ($r^2 > 0.98$)		Limit of Quantitation (ppb)(S/N > 3)		Sensitivity (μC/ppb)		Response Precision (%) (n = 10)		Response Stability(%) (3 day test)	
	M	N	M	N	M	N	M	N	M	N
Ag(I)	1-10000	1-10000	1.1	1.1	0.42	0.53	3.2	2.9	3.7	1.1
Cu(II)	0.6-6400	0.6-6400	0.6	0.6	0.22	0.47	3.5	1.2	4.5	2.3
Pb(II)	2-20000	2-20000	2.1	2.1	0.19	0.37	3.0	2.5	1.2	1.8
Cd(II)	1-11000	1-1100	1.1	1.1	0.01	0.02	4.2	3.1	5.3	3.0

As shown earlier, the simultaneous deposition and stripping of the metals leads to complex voltammograms. The Pb stripping peak splits into two components at higher concentrations when either Ag or Cd is co-deposited. One possible explanation for this is that the metal is depositing and stripping from two energetically distinct sites on the electrode surface. For example, the Pb may be oxidizing from a homogeneous Pb deposit on the diamond surface and from heterogeneous sites where multiple metals have co-deposited. Another possibility is the formation of an intermetallic compound. It is supposed that the dual Pb peaks observed presently are caused by the formation of Ag-Pb and Cu-Pb intermetallic compounds.[16]

The suppression of the Cd(II) peak may be partly attributed to the formation of an Ag-Cd complex. Voltammetric data showing the deposition of Ag-Cd alloys from mixtures of Cd(II) and Ag(I) have been reported.[16] The alloy was of a solid solution type at low concentration of Cd(II) and a mixture of phases at higher concentration. In alkaline media, several researchers have reported two distinct peaks for the transitions of silver to argentous oxide and argentous oxide to argentic oxide.[17] It is still uncertain whether silver is undergoing the same kind of transition on diamond at very low concentrations of metal in this relatively acidic media.

Further, the sensitivity readings for the five metal detection were greater than individual metal detection by a factor of approximately 4-10 for Ag(I), Cu(II), and Pb(II), however they were less by a factor of 2-5 for Cd(II). Zn(II) was not detected in the mixture. This could indicate that Cd(II) and Zn(II) are interacting with the other metals and getting stripped off as intermetallic compounds at the peak potentials of the other metals forming binary/ ternary compounds. See Chapter 6 for a detailed study of the Cu-Zn intermetallic compound formation.

4.3.5 Scanning Electron Microscopy (SEM) Studies of Metal Phase Formation. As described in Chapter 2, metal deposition on diamond surfaces is a complicated process and is not completely understood. The metal under study must nucleate and grow on the surface. The sites at which this occurs, as well as the nucleation and growth mechanism for many metals are not known. Cu deposits equally well on both the facets and the grain boundaries of highly boron-doped microcrystalline diamond.[2] The metal deposits by an instantaneous nucleation and growth mechanism at low overpotentials and progressive mechanism at high overpotentials. Ag deposits on microcrystalline diamond have also been studied.[18] At low overpotentials, an instantaneous nucleation and growth mechanism was observed, while at high overpotentials, a progressive mechanism was found. Zn deposits on microcrystalline diamond by a progressive mechanism at both low and high overpotentials.[19]

SEM was used to image the metal deposits formed on the diamond surface. Representative images of films containing different deposited metals are shown in Figure 4.8. The deposition, in each case, was for 3 min at –1.2 V (no stirring). The Cu deposits are small (mean diam. of 40 ± 13 nm), uniform across the surface, numerous, and well dispersed on the microcrystalline film. All the facets are decorated with deposits. The Ag deposits are also relatively small (mean diam. of 142 ± 73 nm) and well dispersed, but they have a wide range of particle diameters. The Cd deposits are fewer in number and larger (mean diam. 245 ± 211 nm). They appear to have distinct prismoidal geometries. The Pb deposits are fewer in number, small in diameter and scattered (mean diam. ~ 156 ± 21 nm). The Zn deposits (mean diam. ~ 138 ± 76 nm), do not appear to be well distributed and have a clustered appearance.

A similar trend is observed for the deposition of metals on the nanocrystalline diamond. Deposits of Ag are fairly spherical and well dispersed but differed in size (mean diam. ~ 82 ± 48 nm). The Cu deposits have a greater uniformity in size and are numerous and well distributed (mean diam. ~ 32 ± 11 nm). The Cd deposits are few and unevenly distributed, although did appear to have a somewhat geometrical shape (mean diam. ~ 115 ± 33 nm). Pb deposits were globular, and are not well dispersed over the surface. They possess a very large size (mean diam. ~ 481 ± 19 nm). The Zn deposits are also few in number and randomly dispersed (mean diam. of 137 ± 21 nm). The surface area of a film, which was covered by metal, was determined using software assisted image analysis. Table 4.5 shows a comparison of nominal particle size, particle density and fractional surface area of the metal deposits for both diamond types. Except for Pb, the nominal particle size was less and the particle density greater for nanocrystalline diamond. The fraction of the surface area of the diamond covered by metal deposits was larger in all cases (except on Cd where it was nearly equal) for nanocrystalline diamond. This means that more metal phase formation occurs on diamond during the preconcentration step and this translates into greater sensitivity and lower limits of quantitation in the DPASV measurements.

Table 4.5 Comparison of the nominal particle size, density and fractional surface area of the diamond film covered by the metal phase, as determined from scanning electron microscope (SEM) images.

	Microcrystalline Diamond			**Nanocrystalline Diamond**		
Metal	**Nominal Particle Diam. (nm)**	**Particle density (cm^{-2})**	**Fractional Surface Area**	**Nominal Particle Diam. (nm)**	**Particle density (cm^{-2})**	**Fractional Surface Area**
Ag	142 ± 73	3.0×10^{7}	0.019	82 ± 48	1.1×10^{8}	0.173
Cu	40.2 ± 13	1.1×10^{8}	0.040	32 ± 11	2.1×10^{8}	0.109
Cd	245 ± 211	4.0×10^{6}	0.037	115 ± 33	2.1×10^{7}	0.023
Pb	156 ± 21	7.0×10^{6}	0.040	481 ± 19	1.0×10^{6}	0.146
Zn	138 ± 76	7.0×10^{6}	0.027	137 ± 21	7.0×10^{6}	0.019

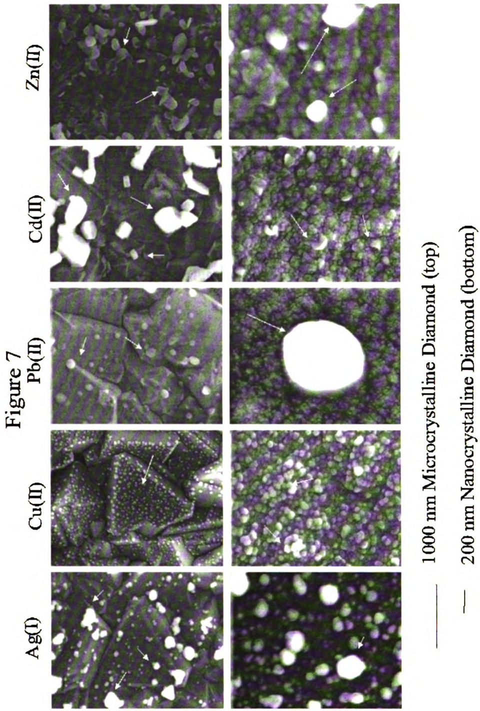

Figure 4.8 Scanning electron micrographs of metal phases deposited on microcrystalline (top) and nanocrystalline (bottom) diamond thin-film electrodes. The deposition, in each case, was for 3 min at –1.2 V (no stirring). Arrows indicate a few representative metal deposits.

4.4 Conclusions

The use of two types of diamond thin films for the detection of trace metal ions, individually and in mixtures, was demonstrated. The detection limits were lower or comparable to those mandated by EPA for the maximum allowable levels of these metal ions in drinking water (given in Chapter 1). The analytical detection figures of merit obtained with diamond compared well with those obtained using Hg-coated GC (the state of the art electrode material for this measurement).

Both diamond types functioned well for the detection of the metal ions and yielded compelling detection figures of merit. However, the limit of quantitation was slightly lower and the sensitivity greater for the detection of the metal ions, both individually and in mixtures, with nanocrystalline diamond. As an example, the linear dynamic range for the detection of Pb (II) at nanocrystalline diamond was four orders of magnitude from 2 to 20,000 ppb, the limit of quantitation was 2 ppb (S/N > 3), and the response precision was 0.4% (n=10). The linear dynamic range at microcrystalline diamond was from 20 to 20,000 ppb, the limit of quantitation was 20 ppb (S/N > 3), and the response precision was 1.6 % (n=10). The greater sensitivity and lower limit of quantitation for nanocrystalline diamond is due to the increased particle density and smaller particle diameter (i.e., increased metal phase formation) during the preconcentration or deposition step. It appears as though the surface morphology of the nanocrystalline diamond possesses a higher nucleation density for metal phase formation then does microcrystalline diamond. This may be caused by the higher fraction of grain boundary on the nanocrystalline film and or a higher fraction of electrically conducting regions. We conclude from this work that nanocrystalline diamond performs in a superior fashion to microcrystalline diamond for this measurement.

In comparison with LSV, the use of the DPASV technique enabled improved analytical detection figures of merit for the analysis of Ag(I), Cd(II) and Hg(II) (From Tables 4.3 and 4.1, respectively).

4.5 References

(1) Granger, M. C.; Xu, J.; Strojek, J. W.; Swain, G. M. *Analytica Chimica Acta* **1999**, *397*, 145-161.

(2) Show, Y.; Witek, M. A.; Sonthalia, P.; Swain, G. M. *Chemistry of Materials* **2003**, *15*, 879-888.

(3) Berzins, T.; Delahay, P. *Journal of the American Chemical Society* **1953**, *75*, 555-559.

(4) Xu, J.; Granger, M. C.; Chen, Q.; Strojek, J. W.; Lister, T. E.; Swain, G. M. *Analytical Chemistry* **1997**, *69*, 591A-597A.

(5) Xu, J.; Chen, Q.; Swain, G. M. *Analytical Chemistry* **1998**, *70*, 3146-3154.

(6) Alehashem, S.; Chambers, F.; Strojek, J. W.; Swain, G. M.; Ramesham, R. *Analytical Chemistry* **1995**, *67*, 2812-2821.

(7) Holt, K. B.; Bard, A. J.; Show, Y.; Swain, G. M. *Journal of Physical Chemistry B* **2004**, *108*, 15117-15127.

(8) Awada, M.; Strojek, J. W.; Swain, G. M. *Journal of the Electrochemical Society* **1995**, *142*, L42-L45.

(9) Reinmuth, W. H. *Analytical Chemistry* **1961**, *33*, 1793-1794.

(10) Vydra, F.; et al., Eds. *Electrochemical Stripping Analysis*; Ellis Horwood Ltd., 1976

(11) Wang, J., Ed. *Stripping Analysis: Principles, Instrumentation, and Applications*; VCH Publishers, Inc., 1985

(12) Temmerman, E.; Verbeek, F. *Analytica Chimica Acta* **1972**, *58*, 263-272.

(13) Copeland, T. R.; Osteryoung, R. A.; Skogerboe, R. K. *Analytical Chemistry* **1974**, *46*, 2093-2097.

(14) Stromberg, A. G.; Gorodovykh, V. E. *Zhurnal Neorganicheskoi Khimii* **1963**, *8*, 2355-2359.

(15) Marques, A. L. B.; Chierice, G. O. *Talanta* **1991**, *38*, 735-739.

(16) Bonfil, Y.; Kirowa-Eisner, E. *Analytica Chimica Acta* **2002**, *457*, 285-296.

(17) Clarke, T. G.; Hampson, N. A.; Lee, J. B.; Morley, J. R.; Scanlon, B. *Berichte der Bunsen-Gesellschaft* **1969**, *73*, 279-283.

(18) Vinokur, N.; Miller, B.; Avyigal, Y.; Kalish, R. *Journal of the Electrochemical Society* **1999**, *146*, 125-130.

(19) Wang, J.; Swain, G. M. *unpublished results* **2002**.

CHAPTER 5

TRACE METAL ANALYSIS IN CONTAMINATED WATER SAMPLES USING ANODIC STRIPPING VOLTAMMETRY AND A NANOCRYSTALLINE DIAMOND THIN-FILM ELECTRODE

5.1 Introduction

There is emphasis for the use of diamond electrodes in stripping voltammetric detection of metal ions due to their favorable properties for this application.[1-3] Recently, cathodic stripping voltammetry at a bare boron-doped diamond electrode was shown to be a reliable and selective method to evaluate the Mn content of marine sediments with a limit of detection of 7.4×10^{-7} M (41 ppb) with a deposition time of 60 s.[4] The electroanalytical determination of Pb(II) by ASV at in-situ-formed, bismuth-film-modified, boron-doped diamond electrodes was also demonstrated. Detection limits in 0.1 M nitric acid of 9.6×10^{-8} M (0.2 ppb) and 1.1×10^{-8} M (2.3 ppb) were obtained after 60 and 300 s deposition times, respectively. [5]

In this Chapter, results from analysis of Ag(I), Cu(II), Pb(II), Cd(II), and Zn(II) in "real world" water samples by DPASV are presented.[6] Chapter 4 showed that nanocrystalline diamond typically outperformed microcrystalline diamond in DPASV of metal ions. Therefore, nanocrystalline diamond films were used to conduct the measurements described herein. Good analytical detection figures of merit were observed with limits of quantitation in the low ppb range, good sensitivity, and excellent response precision and stability (~ 4 %). Data for the detection of these metal ions in four sample types are presented: lake water, tap water, wastewater treatment sludge, and soil. The goals for this work were (i) to investigate the feasibility of detecting trace metal ions in "real-world" water samples using diamond electrodes, (ii) to obtain detection figures of merit for metal ions in several types of contaminated water samples, and (iii) to validate the method through comparison measurements with inductively coupled plasma mass-spectrometry (ICP-MS) and or atomic absorption spectrometry (AAS).

5.2 Experimental

Diamond Film Deposition. The boron-doped nanocrystalline diamond thin film was deposited on a p-type Si(100) substrate (~10^{-3} Ω-cm), using a commercial microwave-assisted chemical vapor deposition (CVD) system. Details of the growth conditions, as well as the follow-up material characterization, were given in Chapter 2. Ultrahigh-purity CH_4, Ar, and H_2 (99.999%) were used as the source gases. The gas flow rates were 1, 94, and 5 sccm, respectively, for CH_4, Ar, and H_2. B_2H_6 was used for doping at a flow rate of 0.001 sccm (10 ppm). The microwave power and deposition pressure were maintained at 800 W and 140 torr, respectively. The substrate temperature was estimated to be around 800 °C using an optical pyrometer. The deposition time was 2 h. The diamond thin film was approximately 4 μm thick, as estimated from the weight change after growth, the density of diamond (3.52 g/cm^3), and the geometric area of the Si substrate. The apparent resistivity was 0.1 Ω-cm, or less, as determined using the four-point probe method.

Inductively Coupled Plasma Mass Spectrometry (ICP-MS Analysis). An inductively coupled plasma mass spectrometer (Micromass Platform ICP-MS) fitted with a hexapole collision cell was used. A Meinhard concentric nebulizer was used for sample introduction. Before data acquisition, the performance of the ICP-MS was optimized using a

and U

the ma

concen

standa

HNO

conce

soluti

conce

samp

to ea

conce

samp

the

resul

curv

CA).

Pb (I

were

proce

in cor

using a standard solution containing 10 μg/L of Be (II), Co (II), In (III), Ce (III), Bi (III), and U (II). Parameters, such as the torch position and gas flow rates, were adjusted until the maximum and most stable signal was observed for each element. The metal-ion concentrations in the unknown samples were determined from the calibration curves for standard solutions. 1 ppm commercial stock solutions of the individual metal ions in 2% HNO_3 were diluted with 2% HNO_3 to prepare six standard solutions over a wide concentration range. For multiple metal-ion analysis, the individual metal ion stock solutions were mixed together to prepare standard mixed-metal solutions of different concentration. For analysis, 1 mL of the standard solution was pipetted into a separate sample tube. 1 mL of an internal standard solution of In (III) and Bi (III) was then added to each tube. The standard solutions were analyzed first, in order of increasing concentration, and this was followed by analysis of the unknowns. The response for each sample was acquired over a one-minute period. The system was thoroughly rinsed with the blank solution (2% HNO_3) after each measurement. The peak intensities of the resultant spectra recorded for the standard solutions were used to construct calibration curves.

1 ppm stock solutions of Cu (II) (CPI, Santarosa, CA), Zn (II) (CPI, Santarosa, CA), Cd (II) (Spex Certiprep, Metuchen, NJ), Ag (I) (Spex Certiprep, Metuchen, NJ), and Pb (II) (Spex Certiprep, Metuchen, NJ) in 2% HNO_3 were used. Nalgene sample bottles were used for solution storage and were first cleaned in a clean room, using the following procedure: (i) degreasing with VersaClean soap, (ii) washing with acetone, (iii) soaking in conc. HCl, (iv) soaking in conc. HNO_3, (v) soaking in warm (40-50°C) 2 M HNO_3,

(vi) soaking in 0.5% HNO_3, and (vii) rinsing with Milli-Q water (Steps 5 and 6 done in Class 100 lab).

Atomic Absorption Spectrometry (AAS) Analysis. Wastewater samples were analyzed for Cu(II), Cd(II), Zn(II), Ag(I), and Pb(II), using a Hitachi Z-9000 Atomic Absorption Spectrophotometer with a graphite tube furnace attachment. The instrument possessed a diffraction grating monochromator, which could be set to the desired wavelength for monitoring the absorbance by a particular metal ion. Cd, Cu, Pb, Ag, and Zn hollow cathode lamps were used with excitation wavelengths of 228.8, 324.8, 283.3, 328.1, and 213.9 nm, respectively. The lamp currents were set at 7.5 mA. The sheath gas used was argon, and its flow was maintained at 200 mL/min. A 20 µL sample volume was introduced into the furnace via an autoinjector. The sample was dried and ashed at pre-specified temperatures and times. Standard solutions containing known concentrations of Cd(II), Cu(II), Pb(II), Ag(I), and Zn(II) were prepared and response curves constructed for each.

Differential Pulse Anodic Stripping Voltammetry (DPASV) Analysis. A single-compartment glass cell was used for all the electrochemical measurements, along with a computer-controlled potentiostat (Model 650a CH Instruments Inc., Austin, TX)[9]. The electrochemical cell was placed inside a Faraday cage for shielding. The diamond thin-film working electrode was pressed against a Viton® o-ring and clamped to the bottom of the cell. A bead of an In/Ga alloy was placed on the backside of the scratched and cleaned Si substrate to ensure good ohmic contact with a copper current-collector plate. A graphite rod was used as the counter electrode, and a commercial Ag/AgCl electrode (saturated KCl) served as the reference ($E^o_{Ag/AgCl}$ = -0.045 V vs. SCE). The geometric area of the working electrode was ca. 0.2 cm^2. All measurements were made in solutions deoxygenated with N_2 for at least 10 min initially, and then for 2 min after each anodic stripping or oxidation cycle. The solutions were blanketed with the gas during all measurements. The electrolyte solution was 0.1 M acetate buffer, pH 4.5. The reference electrode was placed inside a cracked-glass capillary (double junction) that was filled with the acetate buffer. All measurements were made in an unstirred solution. The typical differential pulse voltammetric settings were (i) a 3 min deposition time, (ii) a 0.5 min. "quiet" time prior to initiation of the anodic sweep, (iii) a 50 mV pulse height, 2 mV step height, 50 msec pulse width, 100 msec cycle period, and 35 msec sampling time during the stripping step, and (iv) a constant potential of 600 mV for 120 s after completion of the anodic sweep to fully oxidize all metal deposits prior to the next measurement.

NIST Standard Solution. A standard reference material® (1640, henceforth referred to as SRM 1640) was procured for testing from the National Institute of Standards and Technology (NIST). The aqueous sample contained certified amounts of Ag(I), Cu(II), Pb(II), Cd(II), and Zn(II), in addition to at least 24 other dissolved elements. The certified values of Cd(II), Pb(II), and Ag(I) were 22.79 ± 0.96, 27.89 ± 0.14, and 7.62 ± 0.25 ppb, respectively. The reference values of Cu(II) and Zn(II) were given as 85.2 ± 1.2 and 53.2 ± 1.1 ppb, respectively. According to NIST, the sample was prepared in the following manner. About 3500 L of natural (fresh) water was obtained by U.S.

Geological Survey personnel at Clear Creek, CO. It was filtered through a 0.1 μm ultra filter and acidified with nitric acid. Analysis of the water by ICP-MS, before and after the stabilization process, showed that arsenic, beryllium, cobalt, selenium and zinc decreased in concentration during the stabilization process. These elements were adjusted to their original concentrations by the addition of the appropriate salts. The stabilized solution was then pumped through an ultra filter, past a UV light source (for sterilization purposes), and then to a bottling station. At the bottling station, the bottles were first rinsed with the sample and then filled.

Protocols for Field Sampling. The river, lake, and well water samples were obtained using a homemade (~ 1 meter) sampling rod with an attached 250 mL ultrapure Nalgene bottle. The bottle was filled and rinsed three times with the sample water before collecting a sample for analysis. The bottle was then capped, labeled, and stored in an acid-washed bag for return to the laboratory. Prior to analysis, the sample was filtered to remove solid particulates using a syringe filter (ACRODISC® Syringe Filter, 0.2 μm, Tuffryn Membrane, low protein binding, non-pyrogenic, hydrophilic and bi-directional), and transferred into a 125 mL Nalgene bottle. 20 μL of acid (70% Seastar HNO_3) was then added. The sample was thoroughly mixed and stored in the refrigerator until use. The acidified water samples were analyzed by DPASV, AAS, and or ICP-MS.

Wastewater and Soil Samples. A heavy wastewater sludge sample was obtained from the East Lansing Water Treatment Facility. The heavy sludge solution (50 mL) was acid digested for several hours after adding 100 mL of ultrapure, concentrated HNO_3.

The solution was then decanted and centrifuged for several minutes at ca. 3200 rpm. The supernatant was decanted and then analyzed by DPASV and AAS.

Three contaminated soil samples were procured from a former manufactured-gas plant (MGP) facility located near downtown Grand Ledge, Michigan. The soil samples were obtained using geo-probes that were sent down 10-11 (sample 1), 4-6 (sample 2), and 8-10 (sample 3) feet into the ground. The collected soil samples were acid digested following EPA Method 3050A. This involved the digestion of 1g of soil (wet weight) in 25 mL of 1M nitric acid and 10 mL of 30% hydrogen peroxide. The resultant digestate was reduced in volume by solvent evaporation and then diluted to a final volume of 100 mL using ultrapure water. Particulates in the digestate were removed by filtration (Whatman No. 41 filter paper). The resultant soil extract was tested for Zn(II), Pb(II) and Cu(II) using DPASV and AAS.

Chemicals (AAS and DPASV). All solutions were prepared with ultrapure water (>17 MΩ-cm) from an E-pure purification system (Barnstead). Silver nitrate (Aldrich), Cadmium nitrate (Aldrich), zinc acetate (Aldrich), cupric nitrate (Aldrich), and lead nitrate (Aldrich) were all reagent- grade quality and used without additional purification. 0.1 M acetate buffer was prepared by mixing appropriate amounts of sodium acetate (99%, Aldrich) and acetic acid (99%, Aldrich) solutions. All solutions were prepared fresh daily from their stock solutions and purged with N_2 (99.99%) for 10 min prior to any electrochemical measurement. All glassware was cleaned by a three-step procedure: ethanol/KOH bath, alconox/ultrapure water solution, and ultrapure water rinse.

5.3 Results and Discussion

5.3.1 Analysis of a NIST Standard Solution

Figure 5.1 shows a differential pulse stripping voltammetric i-E curve for the NIST sample, as well as the curves for standard solutions of Pb, Cu, and Ag at equal concentrations ranging from 10 to 90 ppb. The curves are all background corrected. The background was an differential pulse stripping voltammtric i-E curve of the electrolyte solution under the same experimental conditions. The NIST sample has peaks for Pb, Cu, and Ag at potentials of ca. –450, –80 and 280 mV. The peak for Pb in all the solutions is nearly symmetric with a base width of 150 mV. The peak for Cu, particularly for the NIST sample, is asymmetric with a secondary stripping current about 100 mV positive of the main peak. As a result, the base width of the peak is about 300 mV for this sample. The peak width for the standard solution is ca. 150 mV. The peak for Ag for the NIST sample, as well as the standard solutions, is symmetric with evidence for two current maxima. The base width is about 150 mV. In all cases, the peak current and charge increase proportionally ($r^2 > 0.99$) with the solution concentration of each metal ion. Table 5.1 presents DPASV and AAS and ICP-MS determined concentration data for all five metal ions. The concentrations were determined by the standard addition method. As an example, a plot of peak charge versus the concentration of Ag(I) added is shown in Figure 5.2. The concentration of the unknown is determined from the intercept on the negative x-axis, which in this case is 7.3 ppb. There is good agreement between the AAS and DPASV data for all the metal ions, except Cd(II). The response precisions for the measurements with diamond are very good as the coefficients of variation range from 3-4 %. The percent differences between the values for the two methods range from a low of 2.7 % for Zn(II) to high of 11.1 % for Cd(II). The percent differences for some of the elements (e.g., Cd and Cu) are higher than desired. It appears that the large differences seen for Cd(II) and Cu(II) are due, at least in part, to the complexity of the NIST solution as such large differences for these two metal ions were not observed for other real world samples, as is reported below. The data indicate that diamond electrodes provide an analytically useful response for these metal ions that is comparable to other established methods.

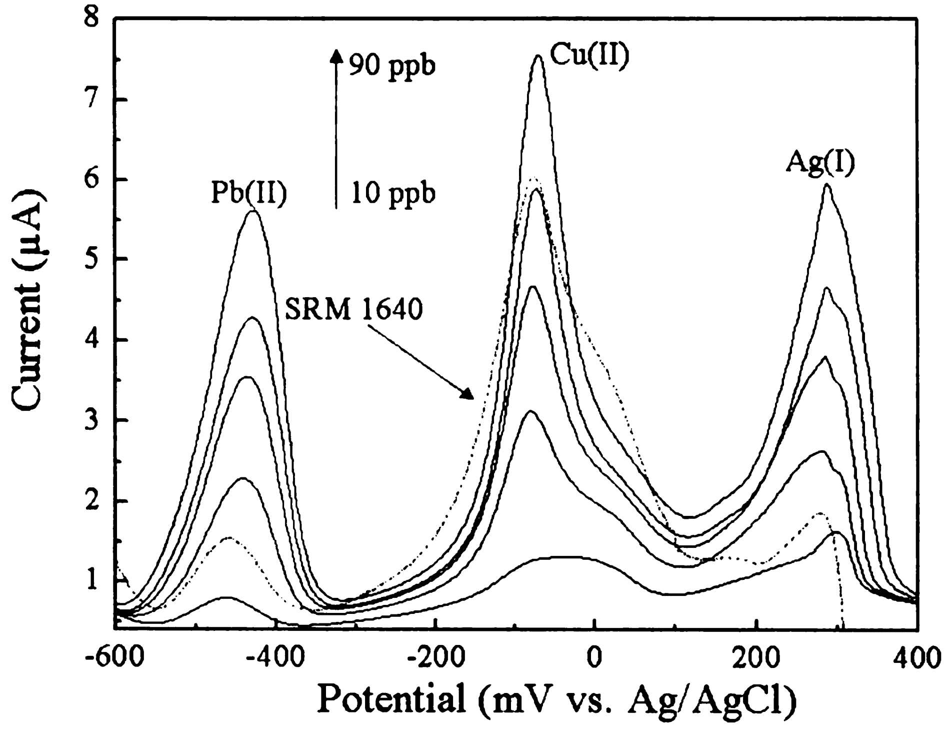

Figure 5.1 Differential pulse anodic stripping voltammetric (DPASV) i-E curves for a standard solution (SRM 1640) and known solutions of Pb, Cu and Ag using a boron-doped nanocrystalline diamond electrode. Deposition potential = - 900 mV. The DPASV conditions are described in the Experimental section. Geometric area = 0.2 cm^2. Peak area integration range = 200 to 370 mV for Ag(I), -200 to 100 mV for Cu(II), and -550 to -380 mV for Pb(II).

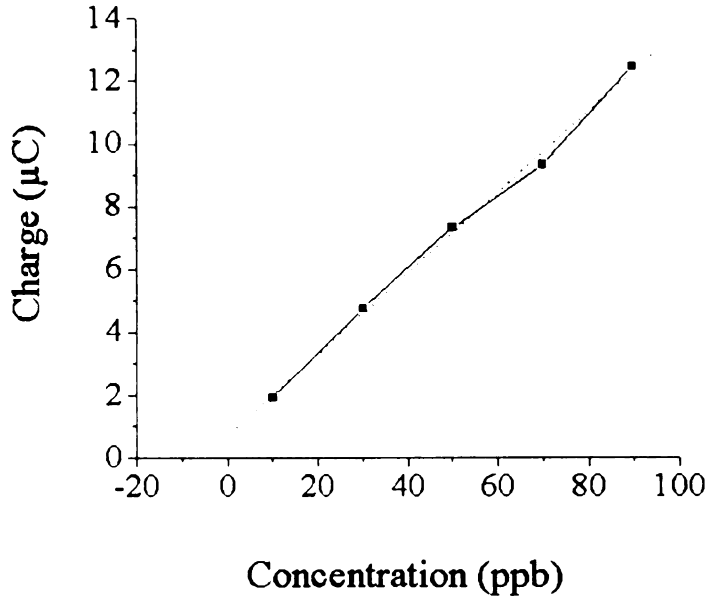

Figure 5.2 Standard addition plot of charge vs. concentration for the addition of solutions containing Ag(I) in increasing concentrations ranging from 10 ppb to 90 ppb to a solution of the SRM diluted in acetate buffer (1:9). All concentrations reported have been corrected for dilution.

Table 5.1 Concentration and percent error data for Ag(I), Cu(II), Cd(II), Pb(II) and Zn(II) in the SRM 1640 water samples.

Results	Ag(I)			Pb(II)			Cd(II)		
Conc.(ppb), $r^2 > 0.98$	ICP	AAS	ASV	ICP	AAS	ASV	ICP	AAS	ASV
SRM 1640	7.01	8.04 ±0.73	7.32 ±0.56	28.3	25.1 ±1.6	30.2 ±0.8	23.7	26.5 ±1.2	25.3 ±1.5
Error %	8.0	5.0	4.2	1.4	10.0	8.4	4.03	16.3	11.1

Results	Cu(II)			Zn(II)		
Conc. (ppb), $r^2 > 0.98$	ICP	AAS	ASV	ICP	AAS	ASV
SRM 1640	80.9	89.3 ±0.6	76.5 ±3.1	57.6	57.0 ± 3.7	51.8 ±2.8
Error %	5.1	4.8	10.2	4.4	7.1	2.7

5.3.2 Drinking Water Analysis

Our first attempt to employ diamond electrodes for metal ion detection in "real world" samples was in the analysis of tap water. Two different samples from the MSU campus were analyzed by DPASV and ICP-MS. Cu(II) was the only metal ion found at detectable concentrations in either water sample. Figure 5.3 shows differential pulse stripping voltammetric i-E curves for the two tap-water samples, and for standard solutions of Cu ranging in concentration from 30 to 130 ppb. The curves shown are all background corrected. Unlike in the voltammetric i-E curve for the NIST sample (see Fig. 5.1), the stripping peak for Cu in these solutions is nearly symmetric, even though the electrode was the same in both cases. The more asymmetric peak shape for the NIST sample is probably caused by the complex nature of the solution from which the Cu(II) is being analyzed (25+ elements present in addition to Cu(II)). The base peak widths in Figure 5.3 range from 150 to 300 mV, with the width widening with increasing concentration of Cu(II) (i.e., increasing surface coverage). The peak current and charge both increase proportionally with the solution concentration of Cu. Based on the peak charge, tap-water sample #2 has a lower Cu(II) concentration than does sample #1. The peak charge was used for quantitation via the standard addition method. The standard addition curve of the peak charge versus the added Cu(II) solution concentration was linear over two orders of magnitude (1-130 ppb) with a least squares correlation coefficient of >0.990. This does not represent the full linear dynamic range for the assay, but rather is only the range of concentrations used in the measurement.[7] Table 5.2 presents the concentration of Cu(II) in the two samples, as determined by DPASV and ICP-MS. The Cu(II) concentration in samples #1 and #2 was determined by DPASV to be 91.2 ± 3.5 and 29.1 ± 1.3 ppb, respectively. At least three measurements were made to evaluate the precision of the DPASV technique. The coefficients of variance were 3.8 and 4.5% ($n \geq 3$), respectively, meaning that the measurements with diamond are very reproducible. Only one ICP-MS measurement was made on each sample so the precision of the measurement cannot be assessed. The ICP-MS measurements revealed a Cu(II) concentration of 87.3 and 26.1 ppb, respectively, for the two samples. Table 5.2 also presents percent difference data between the two methods. For both samples, the DPASV value is larger than the ICP-MS one, with a difference of 4.5% in the values for sample #1 and 11.4% for sample #2. These numbers indicate a good agreement between the values determined by DPASV and ICP-MS, especially for sample #1. The difference in the values for sample #2 is larger than one would like, but since we do not know the variance of the ICP-MS measurement, we cannot be certain that this difference is really this large. The results reveal that diamond provides an analytically-useful response for Cu(II) in these tap water samples, in terms of the sensitivity, response reproducibility and accuracy, at least to the extent that we can evaluate the latter.

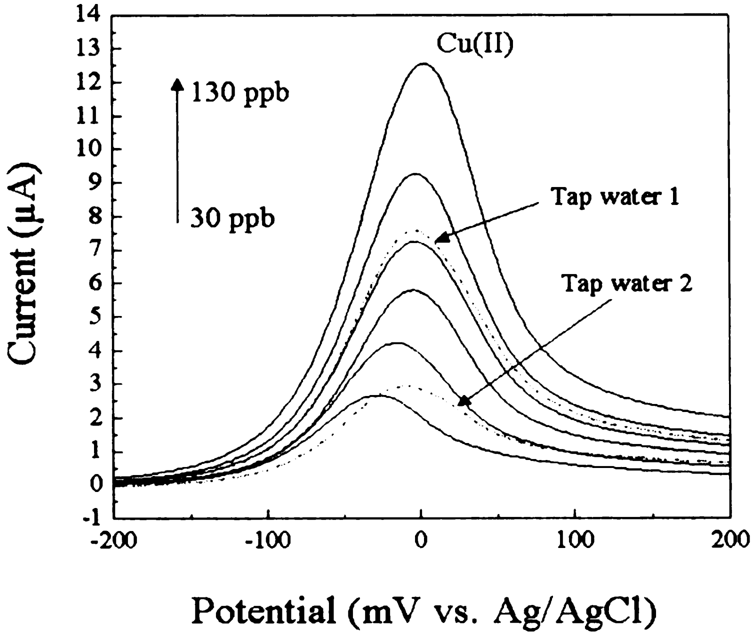

Figure 5.3 Differential pulse anodic stripping voltammetric (DPASV) i-E curves for Cu in tap-water samples #1 and #2 using a boron-doped nanocrystalline diamond electrode. Deposition potential = -200 mV. The DPASV conditions are described in the experimental section. Geometric area of electrode = 0.2 cm^2. Peak area integration range = -100 to 100mV for Cu(II).

Table 5.2 Concentration and percent difference data for Cu(II) in two different tap water samples from the MSU campus as determined by DPASV and ICP-MS.

	Cu(II)		
Concentrations in ppb, $r^2 > 0.98$	ICP-MS	ASV	Difference%
Tap Water 1 (Spartan Village sample, MSU campus)	87.3	91.3 ± 3.5	4.5
Tap Water 2 (University Village sample, MSU campus)	26.1	29.1 ± 1.3	11.4

Lake, Well and River Water Analysis. The nanocrystalline diamond electrode was also used to assay for metal ions in lake (Lake Lansing), well, and river water (Red Cedar) samples. The lake, well and river water samples were from the East Lansing, MI area. Surprisingly, none of the metal ions probed for (Ag(I), Cu(II), Pb(II), Cd(II), and

Zn(II)) were detected in the river water sample. On the other hand, Zn(II) and Cu(II) were found in both the well and lake water samples. The samples were analyzed by both DPASV and AAS, for comparison. The stripping peaks for Zn(II) and Cu(II) (data not presented) were symmetric and easily quantifiable. Quantitation was accomplished from the peak charge via the standard addition method. The concentrations of Cu(II) and Zn(II) in the well water sample were determined to be 28.4 ± 1.4 and 64.1 ± 0.4 ppb, respectively. At least three measurements were made on the sample, with a resulting coefficient of variance of 4.8 and 0.68% for Cu(II) and Zn(II), respectively. The accuracy of the electrochemical method was assessed by analyzing the same sample using AAS. The concentrations of Cu(II) and Zn(II) were determined to be 26.7 ± 2.9 ppb and 63.0 ± 0.3 ppb), respectively. The response coefficient of variance was found to be 11% for Cu(II) and 0.54 % for Zn(II) ($n \geq 3$). The data obtained by DPASV are in good agreement with the AAS results, reflecting the accuracy of the method. In the lake-water sample, only Cu (II) was detected by DPASV at a concentration of 6.30 ± 2.8 ppb. This value is in good agreement with the AAS value of 7.29 ± 2.8 ppb.

5.3.3 Wastewater Treatment Sludge Analysis

Figure 5.4 shows differential pulse stripping voltammetric i-E curves for a wastewater treatment sludge sample, as well as the curves for standard solutions of Cd(II) and Pb(II) ranging in concentration from 50 to 1000 ppb. The curves are all background corrected. Sludge is the solid residue generated during the treatment of wastewater. Heavy metal ions tend to collect in this medium along with poorly biodegradable organic compounds and potentially pathogenic organisms (viruses, bacteria, etc). There is great interest in analyzing wastewater and sewage sludge because of the potential for contamination of surface and groundwater supplies, if inadequately processed.[8]

Pb(II) and Cd(II) are the two metal ions detected in the sludge extract. The sample preparation is described in the Experimental section. Stripping peaks for Cd (ca. –750 mV) and Pb (ca. –525 mV) are present. The peaks for both elements in the standard solutions are symmetric with base peak widths of approximately 150 mV each; However, the peaks in the curve for the sludge extract are broader, particularly for Pb. The peak current and charge for both elements increase proportionally with the solution concentration ($r^2 > 0.99$). The standard addition curves of peak charge versus the concentration of added Pb(II) and Cd(II) were linear over at least two orders of magnitude (10-1000 ppb) with a correlation coefficient ≥0.990. Again, this does not represent the full linear dynamic range of the assay but rather is only the range of concentrations used for the calibration. The concentrations of Cd(II) and Pb(II) were determined by DPASV to be 145 ± 3.2 and 124 ± 4.9 ppb, respectively, with coefficients of variance of 2.2 and 3.9 % (n≥3). The solution was also analyzed by AAS, and concentrations of 156 ± 5.3 and 134 ± 1.6 ppb, respectively, were determined for Cd(II) and Pb(II). The DPASV concentrations are lower by 7-8 % than those determined by AAS. This relatively small percent difference reflects the accuracy of the DPASV method. The results reveal that diamond provides a sensitive, reproducible and accurate response for Cd(II) and Pb(II) in this somewhat complex sample.

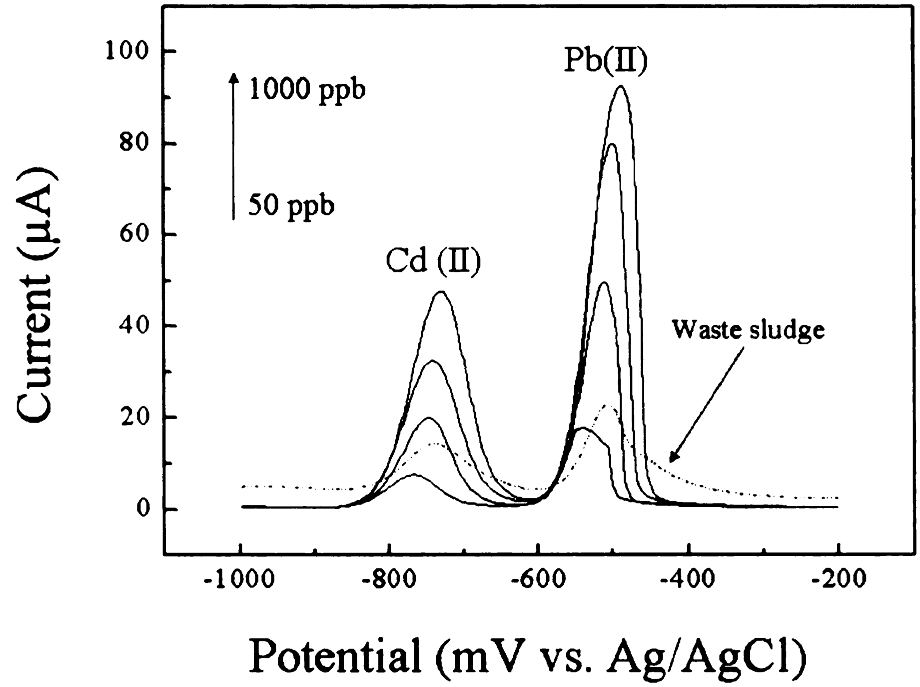

Figure 5.4 Differential pulse anodic stripping voltammetric (DPASV) i-E curves for Cd and Pb in acid-digested waste sludge using a boron-doped nanocrystalline diamond thin-film electrode. Deposition potential = -1000 mV. The DPASV conditions are described in the experimental section. Geometric area = 0.2 cm^2. Peak area integration range = -600 to -450 mV for Pb, and -850 to -650 mV for Cd.

Table 5.3 Concentration and percentage difference data for Cd(II) and Pb(II) in a wastewater treatment sludge extract as determined by DPASV and AAS.

	Cd(II) (ppb)	Pb(II) (ppb)
DPASV	145 ± 3	124 ± 5
AAS	156 ± 5	134 ± 2
Difference %	7.5	8.1

5.3.4 Contaminated Soil Analysis

Figure 5.5 shows differential pulse stripping voltammetric i-E curves for an acidified extract from a contaminated soil sample, as well as the curves for standard solutions of Cd(II) and Pb(II) ranging in concentration from 5 to 120 ppb. Again this does not represent the full dynamic range of the assay but rather only the concentration range used for calibration. The curves are background corrected. Details regarding the soil sample preparation are reported in the experimental section. The results reveal that the soil is contaminated with Cu(II) (ca. 46 mV) and Pb(II) (ca. -482 mV). The peaks for Cu are reasonably symmetric at all solution concentrations with base widths of ca. 100-200 mV, depending on the solution concentration (i.e., surface coverage of Cu). The single peak for Pb at ca. -550 mV is symmetric at low solution concentrations. However, a second peak forms at ca. -410 mV at higher solution concentrations. Both Pb stripping peaks grow larger in amplitude and area with increasing solution concentration. If these peaks are associated with oxidation from two different sites, then these sites do not saturate in coverage during the deposition step. One possibility for the development of the more positive stripping peak is that some Pb is oxidizing from a site that is a little bit less active kinetically. This double stripping peak is something we have seen for some contaminated samples but not all. The stripping peak current and charge for both elements increase proportionally with the solution concentration with a correlation coefficient ≥ 0.99. Table 5.4 presents the concentration of each element in the two different soil samples, as determined by DPASV and AAS. The concentrations of Pb(II) and Cu(II) in soil sample 1 were determined by DPASV to be 97.6 ± 3.1 and 74.5 ± 2.7 ppb, respectively. The precision of the measurement was good with coefficients of variance of 3.1 and 3.6 % (n≥3), respectively. The concentrations of Pb(II) and Cu(II) in soil sample 2 were determined by DPASV to be 272.5 ± 5.6 and 995 ± 14 ppb, respectively. Again the precision was good with coefficients of variance of 2.1 and 1.4% (n≥3), respectively. There was good agreement between the AAS and DPASV results as the percent differences range from 2 to 7 %.

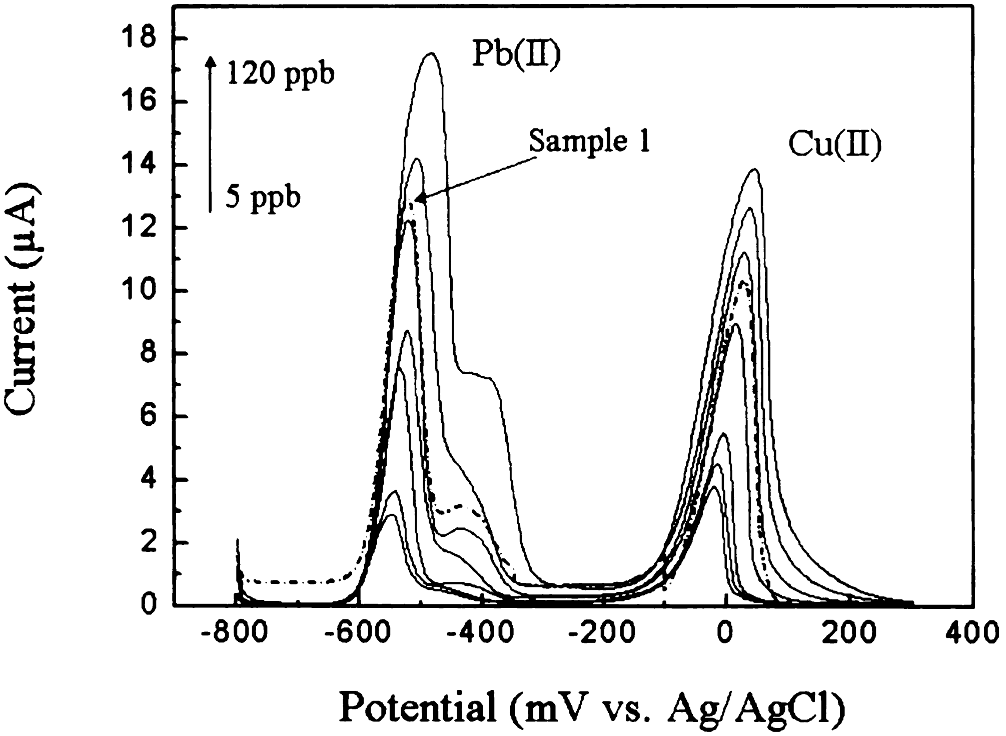

Figure 5.5 Differential pulse anodic stripping voltammetric (DPASV) i-E curves for Pb and Cu in MGP contaminated soil extracts using a 10 ppm boron-doped nanocrystalline diamond thin-film electrode. Deposition potential = - 1000 mV. The DPASV conditions are described in the experimental section. Geometric area = 0.2 cm^2. Peak area integration range = -50 to 80 mV for Cu(II), and -525 to -425 mV for Pb(II).

Table 5.4 Concentration and percent difference data for Pb(II) and Cu(II) in contaminated soil extracts as determined by DPASV and AAS.

		DPASV	AAS	Difference %
Pb(II) (ppb)	Sample 1	97.6 ± 3.1	92.9 ± 4.5	5.1
	Sample 2	272 ± 6	259 ± 12	5.0
Cu(II) (ppb)	Sample 1	74.5 ± 2.7	69.5 ± 1.5	7.2
	Sample 2	995 ± 14	972 ± 21	2.4

5.4 Conclusions

Boron-doped diamond thin film is a viable alternate electrode material for anodic stripping voltammetry. The material possesses many of the same properties as Hg but is non-toxic. For Ag(I), Cu(II), Pb(II), Cd(II) and Zn(II), the electrode provides good sensitivity, low limits of detection, good response precision, and response stability for several "real-world" sample types: lake and well water, tap water, wastewater treatment sludge, and contaminated soil.

Even with the favorable detection figures of merit, research remains to be conducted in order to further optimize the electrode performance. First, the stripping peaks are rather broad (ca. 100-150 mV). This is due, at least in part, to the wide range of metal particle sizes on diamond when using fixed potential deposition. The heterogeneity of the electrode surface also plays a role. Our initial efforts for the investigation of pulsed galvanostatic deposition as a means to reduce the nominal particle size are presented in Chapter 6. Second, although not a significant problem in the present analyses, intermetallic compound formation remains an issue to be addressed when using non-Hg alternate electrodes. Several researchers have observed reduced intermetallic compound formation with electrodeposited Ga.[9] Third, the issue of electrode fouling needs to be further explored. Specifically, the roles of the diamond surface chemistry, the deposited metal, and the type of organic matter on the electrode response stability needs to be further elucidated. In one study reported, the presence of cationic, anionic, and neutral surfactants and humic substances affected the peak heights of Cu, Pb, and Cd in synthetic seawater analyzed by differential pulse anodic-stripping voltammetry.[10] At surfactant concentrations of less than 0.1 ppm, the effect was insignificant, but at higher concentrations the peak heights usually decreased, although for Cu(II) an increase in the peak height was also observed.

5.5 References

(1) Zhang, Y.; Yoshihara, S. *Journal of Electroanalytical Chemistry* **2004,** *573*, 327-331.

(2) Manivannan, A.; Kawasaki, R.; Tryk, D. A.; Fujishima, A. *Electrochimica Acta* **2004,** *49*, 3313-3318.

(3) Chatterjee, A.; Wiltshire, R.; Holt, K. B.; Compton, R. G.; Foord, J. S.; Marken, F. *Diamond and Related Materials* **2002,** *11*, 646-650.

(4) Banks, C. E.; Kruusma, J.; Moore, R. R.; Tomcik, P.; Peters, J.; Davis, J.; Komorsky-Lovric, S.; Compton, R. G. *Talanta* **2005,** *65*, 423-429.

(5) Kruusma, J.; Banks, C. E.; Compton, R. G. *Analytical and Bioanalytical Chemistry* **2004,** *379*, 700-706.

(6) Sonthalia, P.; McGaw, E.; Show, Y.; Swain, G. M. *Analytica Chimica Acta* **2004,** *522*, 35-44.

(7) Show, Y.; Witek, M. A.; Sonthalia, P.; Swain, G. M. *Chemistry of Materials* **2003,** *15*, 879-888.

(8) Farre, M.; Barcelo, D. *TrAC, Trends in Analytical Chemistry* **2003,** *22*, 299-310.

(9) Copeland, T. R.; Osteryoung, R. A.; Skogerboe, R. K. *Analytical Chemistry* **1974,** *46*, 2093-2097.

(10) Sagberg, P.; Lund, W. *Talanta* **1982,** *29*, 457-460.

CHAPTER 6

CHALLENGES AND SOLUTIONS: TOWARDS GAINING BETTER SELECTIVITY AND RESOLUTION DURING THE ANODIC STRIPPING VOLTAMMETRY OF METAL IONS USING BORON-DOPED DIAMOND THIN-FILM ELECTRODES

6.1 Introduction

Intermetallic Compound Formation. An intermetallic phase is defined as a "compound or intermediate solid that contains two or more metals, which has characteristic properties and a crystal structure different from those of the pure metals or the terminal solid solution."[1] Intermetallic compound formation can be a complicating factor in ASV. When an intermetallic compound forms, the stripping peaks for the constituent metals can be attenuated, shifted or enhanced.[2] Intermetallic compound formation is known to cause peak suppression and multiple stripping peaks due to the formation of a new phase that may not oxidize at the same potentials as the individual metals. Some of the more common intermetallics are Ag-Cd, Ag-Zn, Cu-Cd, and Cu-Zn.[3, 4]

A large amount of recent research on the formation of intermetallic compounds in ASV has focused on the Cu-Zn complex.[5-9] This is because of the co-existence of these metals in a diverse number of environmental samples and the fact that the response of each significantly affects that of the other. The simultaneous deposition of Cu and Zn results in the formation of three compounds, CuZn, $CuZn_2$ and $CuZn_3$, at least with an HMDE. These compounds oxidize near the $E^{o'}$ for Cu, resulting in an enhanced Cu peak and a diminished Zn peak.[10] When a Hg-film electrode and a Cu(II)/Zn(II) ratio of 2.0 were used, the Zn peak completely diminished.[11] The formation of CuZn (insoluble) and

$CuZn_2$ (soluble) compounds were also reported for the simultaneous deposition of Cu and Zn at a Hg thin-film electrode. The electrodeposition potential of - 0.85 V (vs. SCE) was determined as the potential for the reduction of Cu in presence of Zn.[8] In this Chapter, we have used the Cu-Zn intermetallic complex to illustrate the challenges and proposed technical solutions for the anodic stripping voltammetric detection of these metal ions using diamond thin-film electrodes.

Increasing the Peak Currents and Reducing the Peak Widths in the Voltammograms. The activity of metal deposit depends not only on the surface coverage but also on the interaction of the metal with the electrode material. The quality of the DPASV measurement could be improved if the relatively large peak widths seen in most of our presented data were reduced. There are several causes of the broad peaks. First, if the metal deposits are not of a small nominal diameter with a narrow size distribution, then the stripping peaks will be broadened due to the wide range of times required for the metal phase to oxidize and the metal ions to diffuse away. Second, if there are activity differences across the diamond surface, specifically variations in the electrode conductivity, then broadened peaks will result due to variable rates of reaction. From results presented in Chapter 2, we have observed that such heterogeneity, although present, is minimized at the high doping level of the films being used in this work. Further, it is speculated that if the metal deposits are well dispersed over the electrode surface and of small nominal diameter, then the probability of a physical/chemical interaction of the surface ad-atoms is reduced, thereby reducing intermetallic complex formation.

In this Chapter, we demonstrate the use of pulsed galvanostatic deposition to produce metal deposits that are nominally smaller in size and more uniformly dispersed over the diamond surface than what is achieved using either constant potential or constant current deposition.[12] Pulsed galvanostatic deposition produces highly dispersed metal deposits of a small nominal diameter, which in turn leads to relatively sharp and narrow stripping peaks. An advantage of the galvanostatic method is that the metal nucleation and growth can be forced to take place at a pre-determined rate.[13] This Chapter includes: (a) a comparison of differential pulse stripping voltammetric i-E curves for Cu and Zn with the metal deposition accomplished by pulsed current, constant current and constant potential deposition, (b) scanning electron micrographs showing a comparison of the metal deposit size and dispersity for the pulsed and constant current deposition methods, (c) analytical detection figures of merit for Cu(II) when using pulsed galvanostatic deposition to preconcentrate the metal, and (d) a study of how intermetallic compound formation between Cu and Zn is affected by the use of constant potential and pulsed current deposition.

6.2. Experimental

Diamond Film Deposition. Boron-doped diamond thin films were deposited on p-type Si(100) substrates (~10^{-3} Ω-cm) using a commercial microwave-assisted chemical vapor deposition (CVD) system.[14, 15] Details regarding the growth conditions, as well as the follow-up material characterization, have been provided in Chapter 2. B_2H_6 was used for doping at a flow rate of 0.001 sccm (10 ppm). In order to provide a reproducible hydrophobic surface, the diamond thin-films used in this work were all freshly acid-washed and rehydrogenated. Acid washing involved soaking the films in warm aqua-regia and then in warm 30% hydrogen peroxide for 30 min each. The films were rehydrogenated by exposing them to a hydrogen plasma for 30 min.

Electrochemistry. Most of the electrochemical measurements were made using either a CHI 650a or a CHI 900 computerized potentiostat (CH Instruments Inc., Austin, TX) and a single compartment, three-electrode glass cell placed inside a Faraday cage for shielding. The diamond working electrode was pressed against a Viton® o-ring and clamped to the bottom of the cell. The backside of the cleaned substrate was scratched with a carbon rod for ohmic contact with a metal plate current collector. A graphite rod was used as the counter electrode and a home-made Ag/AgCl electrode (4 M KCl) served as the reference ($E^0_{Ag/AgCl}$ = -0.045 V vs. SCE). The geometric area of the working electrode was 0.163 cm^2 (intermetallic study) and 0.222 cm^2 (pulse deposition study). All measurements, unless otherwise noted, were made in solutions deoxygenated with nitrogen (99.99%) for at least 2 min initially and then for 3 min after each anodic stripping or oxidation cycle. The solutions were blanketed with the inert gas during a measurement. The electrolyte solution was 0.1 M acetate buffer, pH 5.2. 30 ppm of calcium acetate and 5 ppm of magnesium acetate were added to the electrolyte solution. The reference electrode was placed inside a cracked glass capillary, filled with the acetate buffer, which served as a double junction. All measurements were made in an unstirred solution. The electrode was left mounted in the electrochemical cell, and covered with water, for the duration of the pulse deposition experiments reported. This allowed for the same area of the electrode to be used in all the experiments. Typical differential pulse voltammetric settings were a (i) 3 min deposition time without stirring, (ii) a 0.5 min "quiet" time at the deposition potential prior to initiation of the anodic sweep, (iii) a 50 mV pulse height, a 2 mV step height, a 50 msec pulse width, a 100 msec cycle period, a 35 msec sampling time, and (iv) a constant potential of 600 mV for at least 120 s and up to 300 s after completion of the anodic sweep to oxidize all metal deposits.

Chemicals. All solutions were prepared with ultra-pure water (>17 MΩ-cm, deionized and passed over activated carbon) from an E-pure water purification system (Barnstead). Silver nitrate (Fisher), cadmium nitrate (Aldrich), zinc acetate (Aldrich), cupric nitrate (Aldrich) and lead nitrate (Aldrich) were reagent grade quality used without additional purification. 0.1 M acetate buffer was prepared by mixing appropriate amounts of sodium acetate (99%, Aldrich) and acetic acid (Aldrich) in water. All glassware and nalgene storage bottles were cleaned by a three-step procedure: thorough rinsing with an alconox and ultra-pure water solution, soaking in 1 M hydrochloric and nitric acid for at least 10 min. each, and a final ultrapure water rinse. The cleaned item was then dried in an oven at ~55° C.

Physical Characterization of the Metal Deposits. The metal deposits on diamond were characterized using a JSM-6400V scanning electron microscope (JEOL LTD., Tokyo, Japan). Micrographs were recorded using both secondary and backscattered electrons generated with an accelerating voltage of 20 kV. The presence of Cu and Zn was verified by energy dispersive x-ray (EDX) analysis (Noran Instruments Inc., Middleton, WI) in conjunction with the JSM-6400V. The usual parameters were an integration time of 100 s and a take off angle of 30°. Particle analysis was performed with the AnalySIS imaging software (Software Imaging System Corp., Lakewood, CO).

Scanning electron micrographs and energy dispersive spectra were recorded for Cu and or Zn deposited onto microcrystalline diamond for 3 min at a deposition potential of -1.3 V. The applied potential was cathodic of both $E^{o\prime}$ values so that the reduction reactions occurred at a mass-transfer limited rate. The solutions were deoxygenated for 3 min in the electrochemical cell prior to the application of the deposition potential. Metal deposition was accomplished using solutions of different Cu(II) and Zn(II) concentration.

Scanning electron micrographs of Cu deposited from a 10 ppm solution of Cu(II) in pH 5.2 acetate buffer on nanocrystalline diamond films were also acquired after galvanostatic deposition at 15 mA/cm^2 using the constant current and pulsed current deposition conditions. The solutions were degassed in the electrochemical cell for 3 min prior to the deposition.

Pulsed Galvanostatic Deposition. The hardware for the pulsed current deposition consisted of a homemade galvanostat, configured from an OMNI 90 potentiostat (Cypress Systems, Inc., Lawrence, KS), that was interfaced with a PCI-5401E controller and data acquisition board (National Instruments, Austin, TX). The pulse generation was computer-controlled using National Instruments LabVIEW software (version 5.1 or 6.0). The scheme of the electrical set-up used has been described by Countanceau et al. and it is shown in Figure 6.1.[16] A resistor was placed in between the working and the reference output leads from the potentiostat in order to generate the desired current. The current was generated as a function of the applied potential. Cu was galvanostatically deposited from a 100 ppb Cu(II) solution by varying the pulse conditions (current density, pulse width, pulse number and duty cycle). The metal was then oxidized potentiostatically by applying a DPASV potential scan, in most cases, from -300 to 300 mV. An Ag/AgCl reference electrode kept in a cracked capillary junction containing the electrolyte was introduced into the cell during the potentiostatic oxidation step. The reference electrode was removed from the cell during the galvanostatic step to minimize short-term potential fluctuations and instabilities.

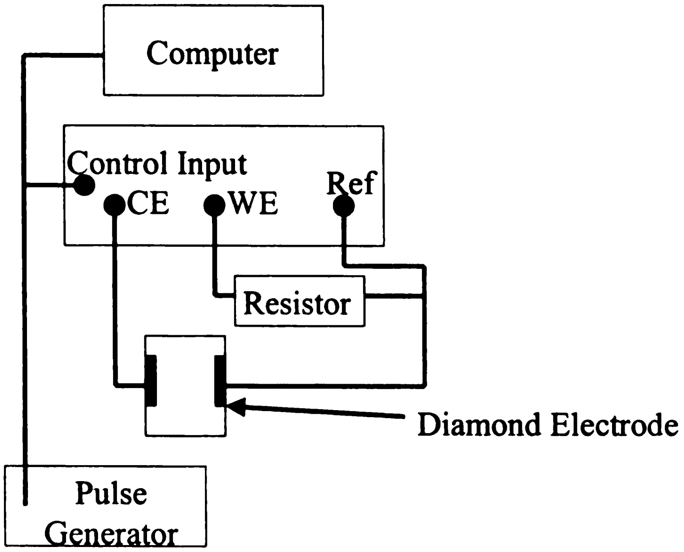

Figure 6.1 The electrical set-up used for the galvanostatic pulse electrodeposition. (Adapted from Reference 15). CE – counter electrode, WE – working electrode and Ref – reference electrode.

The current density, pulse width, pulse number and duty cycle were systematically investigated for their effect on minimizing the stripping peak widths and maximizing the peak amplitude. The goal was to obtain intense and narrow peak shapes and to maximize the ratio i_p^{ox}/FWHM . After some study, the optimized pulse conditions were found to be a 0.5 s width with a 0.5 s delay time between each pulse, and a current density of 15 mA/cm^2. The deposition period was 180 s with a total of 180 pulses. The effective deposition time was therefore 90 s.

6.3 Results and Discussion

6.3.1 Intermetallic Compound Formation

DPASV Interference Studies of Binary Metal Ion Solutions. These experiments revealed at what solution concentrations of the constituent metal ions intermetallic compound formation is most problematic at diamond electrodes, if at all. The possibility of the formation of Cu-Zn complexes was investigated by recording the stripping voltammetric i-E curves for a solution containing a fixed concentration of Cu(II) and as a function of the concentration of added Zn(II), and vice-versa.

Zn-Cu binary solutions. Figure 6.2 shows the background-subtracted differential pulse stripping voltammetric i-E curves for Zn and Cu at a boron-doped nanocrystalline diamond thin-film electrode. Cu(II) was added in increments of 20 ppb to a solution containing 100 ppb Zn(II). The supporting electrolyte was 0.1 M acetate buffer at pH 5.2. The Zn stripping peak initially appears as a broad curve with a maximum around – 915 mV (bold solid line). Notice that the peaks have shifted below the zero line. This effect is occasionally observed at low concentrations of Zn(II). At these potentials there is a substantial amount of charge passed for the hydrogen evolution due to the reduction of water. This means that the background current associated with hydrogen evolution, is larger in the absence of Zn. In other words, the deposition of Zn makes the surface less active for hydrogen evolution. Further, this particular voltammetric i-E curve for the 100 ppb Zn(II) solution is less well defined than was normally seen for the same solution concentration of Zn(II) in previous work. It is possible that there was some Cu(II) contamination in the system. Suppression of the Zn stripping peak current by co-deposited Cu is widely known.[3]

With the addition of Cu(II), there is an increase in the area under the Zn stripping peak and it transitions to a well defined peak shape. Although enhancement in the peak current and charge occur with each added aliquot of Cu(II), the maximum enhancement occurs after the addition of the first aliquot. There are two possible explanations for the observation. Some of the deposited Cu may be oxidizing off at the potentials of Zn. This could indicate the formation of an electroactive intermetallic phase between Cu and Zn with $E^{o\prime}$ close to that of Zn, at these experimental conditions. However, it is also possible that Cu is deposited preferentially as opposed to Zn and the deposition of Zn takes place on the already formed Cu deposits. The deposition of Zn on Cu may have a larger metal loading than on the bare diamond surface yielding the enhanced peaks for Zn. From the literature, thermodynamic considerations and from scanning electron microscopy data, this is the more plausible explanation for enhancement of the Zn peak.[4, 17]

The Cu stripping peak between -200 to 100 mV was also studied as a function of the added Zn(II). With only the Zn(II) initially present in the solution, the i-E curve for

Cu is flat and featureless (no Cu phase formed). After addition of 20 ppb Cu(II) to the 100 ppb Zn(II) solution, two Cu stripping peaks initially appear at -5 mV and - 105 mV. With increasing amounts of Cu(II), the peak at – 105 mV grows in intensity and the peak at –5 mV somewhat merges into and broadens this peak. A possible reason for the observation of the dual peaks could be the oxidation of Cu from two energetically different sites on the diamond surface. Another possibility is that the peak at -5 mV is a result of the oxidation of a Cu-Zn complex that was formed between the two metals. This theory is strengthened by the fact that there is a limited amount of Zn(II) initially present in the solution and this peak does not track the solution concentration of Cu(II). When only Cu(II) is present in solution, it was uncommon to observe the dual/multiple peaks.

Cu-Zn binary solutions. Figure 6.3 shows the background-subtracted differential pulse stripping voltammetric i-E curves for Zn and Cu recorded to test the effect of making standard additions of Zn(II) to a solution containing Cu(II). The area under the i-E curve with no Zn(II) present represents the charge generated due to hydrogen evolution. Cu is known to catalyze this reaction and shift the hydrogen evolution positive.[18] On the addition of aliquots of Zn(II) to the solution, the total area under the Zn peak somewhat increased. However, as observed from the Figure, there is no clear trend of increase of current magnitude for the Zn peak with Zn(II) concentration. This is probably due to some of the Zn interacting with the Cu and oxidizing at the potentials close to that for Cu.

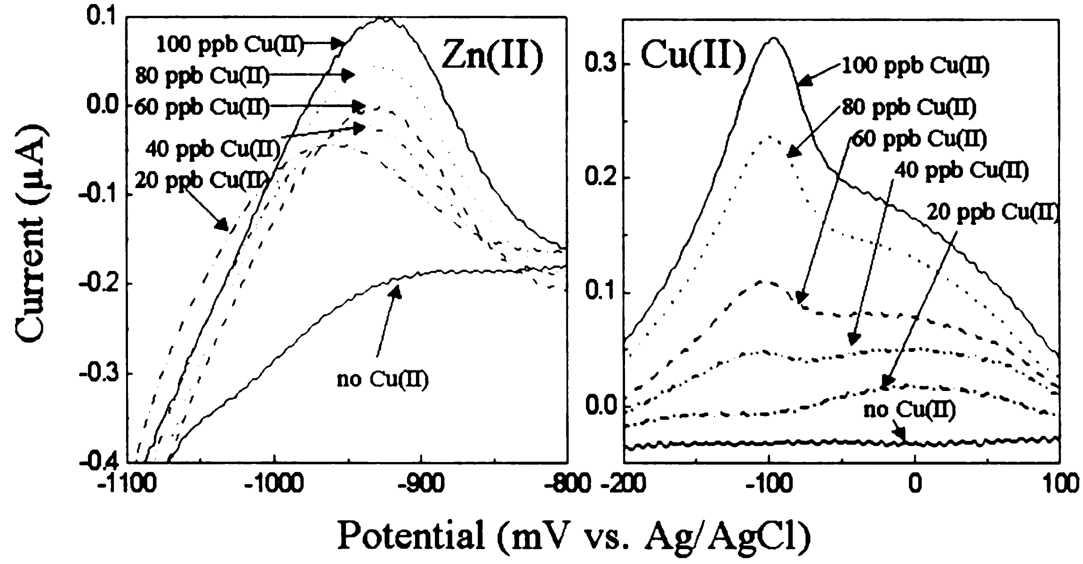

Figure 6.2 Differential pulse anodic stripping voltammetric (DPASV) i-E curves for Cu and Zn. Standard additions of solutions containing Cu(II) were made in increments of 20 ppb to a solution of 100 ppb Zn(II) in pH 5.2 acetate buffer. Deposition potential = - 1300 mV. The DPASV conditions are as described in the experimental section. Electrode geometric area = 0.163 cm^2.

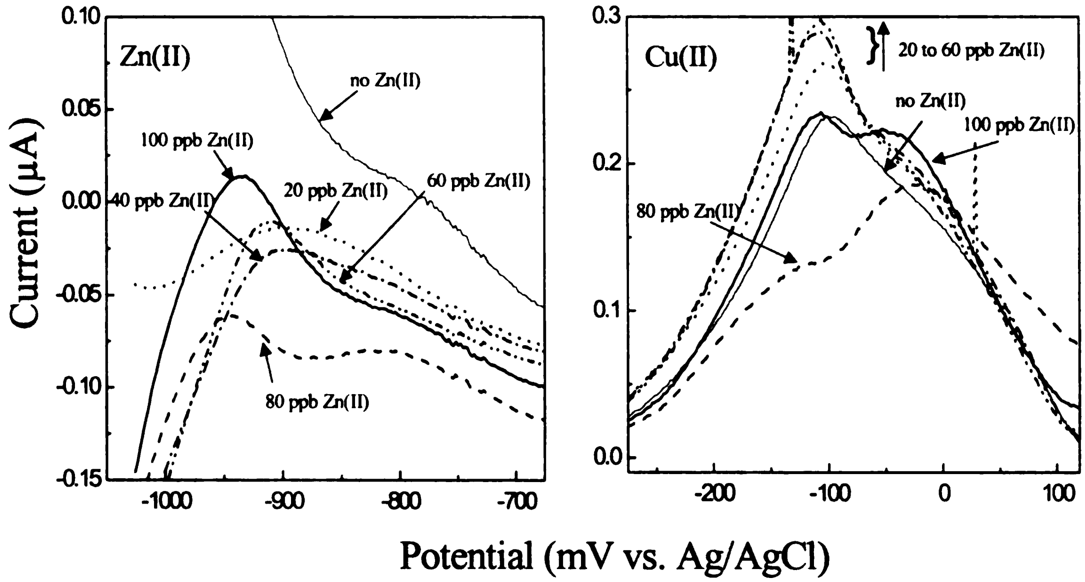

Figure 6.3 Differential pulse anodic stripping voltammetric (DPASV) i-E curves for Cu and Zn. Standard additions of solutions containing Zn(II) were made in increments of 20 ppb to a solution of 100 ppb Cu(II) in pH 5.2 acetate buffer. Deposition potential = - 1300 mV. The DPASV conditions are as described in the Experimental section. Electrode geometric area = 0.163 cm^2.

The intensity of the Cu peak at about – 100 mV is slightly enhanced with the addition of Zn(II); however, it decreases at concentrations of 80 ppb Zn(II) and higher. A sister peak at about – 31 mV gets prominent at higher concentrations of Zn(II). It is possible that this peak is formed due to the oxidation of a product of the Cu-Zn interaction.[10]

Overall, the co-deposition of Cu and Zn significantly affected the response of the other. The addition of a metal ion to the solution in the presence of the other resulted in an increase in peak charge at or near the $E^{o\prime}$ of the added metal ion, in both cases. Presence of Cu(II) shifted the hydrogen evolution positive, making the analysis of Zn(II) challenging. Evidence of Cu and Zn forming a new phase that that undergoes oxidation near the $E^{o\prime}$ for Cu was observed. A generalized standard addition procedure could be useful for the determination of the metal ion of interest nullifying matrix effects for the other.[19]

The oxidation of a metal system depends on various factors, information on which is available in phase diagrams. The electronic work function, ϕ, can serve as an important quantitative characteristic of the electrochemical behavior of a metal.[20] Brainina and Neyman have compared the electronic work function of metals and the interaction type (phase diagrams) of binary systems.[21] Table 6.1 (adapted from their book) shows an arrangement of selected metals in descending order of the electronic work function ϕ horizontally and general data on the character of the phase diagrams in each box that corresponds conventionally to the system $E_2 - E_1$. The table specifies groups of elements forming continuous solid solutions and intermediate phases and chemical compounds as well as the number and kinds of voltammetric peaks expected. According to the phase diagrams, Cu is most prone to the formation of intermetallic compounds, and this is the case both from our experimental results and also from reported literature. As predicted from the table, peaks of Zn(II) are experimentally observed to be suppressed in the presence of Cu(II). In contrast, Pb-Zn, Pb-Cd, Cd-Zn and Zn-Ag are systems without mutual interaction, both from the table as well as experimental results. Overall, it may be inferred that for some binary metal systems the character of interaction and the properties of the phases being formed are determined by the values of the electronic work functions of the corresponding metals.

There are several ways to minimize intermetallic compound formation. One approach is the preferential formation of another intermetallic compound.[4] This approach is based on the addition of a "third" element that forms a more stable intermetallic compound with one component of the binary system. For example, adding an excess of Ga(III) to the sample solution usually solves the Cu-Zn intermetallic problem, as the Cu-Ga complex has a larger formation constant than Cu-Zn and the Zn(II) solution concentration can then be determined without any interference.[22] Another approach to solving this problem was proposed by Heineman and coworkers.[11] Using a twin electrode thin layer cell, they selectively plated Cu at one electrode and measured Zn(II) by ASV at the other electrode. In another report, the addition of CN^- and Triton X-100 was shown to suppress the formation of the Cu-Zn intermetallic compound in ASV making it possible to determine trace levels of Zn(II) in the presence of an excess of Cu(II).[7]

Table 6.1 Work functions, Kinds of Interactions in Binary Systems and Types of Anodic Voltammetric i-E curves of Electrochemically Formed Deposits. (Adapted from Ref 21)

ϕ	4.55	4.30	4.30	4.24	3.97	
E_1	Cu	Ag	Zn	Pb	Cd	
		▥ 2	◼ 3	◼ 2	◼ 3	Cu
			▥ 1	▥ 2	▥ 3	Ag
				◻ 1	◻ 1	Zn
					◻ 1	Pb
						Cd
						E_2

▥ solid solution

◼ intermetallic compound

◻ system without interaction

Kinds of anodic voltammograms:
1 - peaks of E1 and E2
2 – one additional peak
3 – peak of E1 disappears while E2 is in excess
4 – several additional peaks

Our approach, at present, is to limit the surface concentration of the metals by maintaining nominally small and highly dispersed deposits over the electrode surface. This is discussed below. Wise et al. studied conditions to avoid intermetallic compound formation between Cu and Zn at Hg electrodes. The use of shortened preconcentration times helped reduce errors for Cu(II) and Zn(II) concentrations in the ppb range.[3] This may be attributed to reduced interaction between the metals as decreased amounts of metal would get deposited at shorter preconcentration times.

6.3.2 Characterization of the Cu-Zn metals deposited on diamond

Figure 6.4 and 6.5 show scanning electron micrographs and energy dispersive x-ray spectra recorded for Cu/Zn metal deposits on a microcrystalline diamond thin-film electrode. The deposit was formed for 3 min at -1300 mV. Deposition was performed from solutions of Cu(II) and or Zn(II) in the following proportions: (A) 100 ppm Cu(II); (B) 100 ppm Cu(II) + 10 ppm Zn(II); (C) 100 ppm Zn(II); and (D) 100 ppm Zn(II) + 10 ppm Cu(II). The purposes for conducting these experiments at varying concentration ratios of the two metal ions were: (i) to ascertain if there were any differences in the shape, size, density and location of the metal deposited on the diamond surface, individually and from their mixtures; and (ii) to determine if one or both the metals were being deposited on the diamond surface at various experimental conditions.

As can be seen from the micrographs in Figure 6.4, the metal particles are well dispersed and present on both the grains and the boundaries in all four cases. The Cu-only deposits are large in number, uniform in size and well dispersed. The average particle size is ~85 nm and the particle density is ~ 2.3×10^8 cm^{-2}. The deposits formed from the 10:1 Cu(II):Zn(II) ratio are aggregated and several new particles appear to form on existing deposits. The average particle size is ~125 nm and the particle density was found to be ~ 3.4×10^8 cm^{-2}. It is possible that Cu deposits first because its $E^{o\prime}$ is almost 1000 mV positive of the applied potential, and the Zn deposits on the Cu more easily than on the bare diamond. The deposits of only Zn are uniform in size, evenly distributed and possess a relatively small nominal diameter of about 100 nm and the particle density is ~ 1.6×10^7 cm^{-2}. In comparison, particles deposited from the 10:1 Zn(II):Cu(II) ratio are greater in number, evenly distributed and of nominal diameter similar to the deposits of pure Zn (~ 100 nm). The particle density was found to be ~ 5.8×10^{7} cm^{-2}. There is evidence of new metal formation on existing metal phases.

It appears that Cu deposits form in large number over the entire diamond surface whereas Zn deposits are fewer in number and more isolated. A greater number of particles are expected to form at a faster rate for Cu than for Zn, due to the differences in applied overpotential. When low concentrations of Zn(II) are present in a Cu(II) solution, it is likely that a new metallic phase is getting formed because of the larger particle density and clustered nature of the resultant particles. Further, Zn appears to be preferentially deposited on Cu deposits.

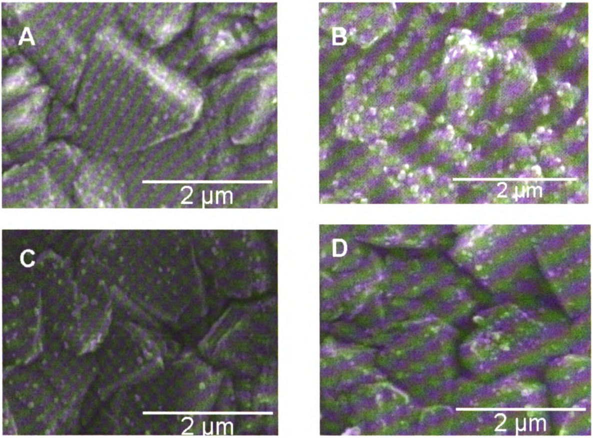

Figure 6.4 SEM images (secondary electron) of Cu and or Zn metal deposits on a microcrystalline diamond electrode formed at -1.3 V for 3 min from varying ratios of the metal ions in solution: (A) 100 ppm Cu(II); (B) 100 ppm Cu(II) + 10 ppm Zn(II); (C) 100 ppm Zn(II); and (D) 100 ppm Zn(II) + 10 ppm Cu(II).

Figures 6.5 A and B show the corresponding energy dispersive spectra for the metal deposits in images B and D of the previous figure. All experimental conditions (e.g., image magnitude, accelerating voltage etc.) were the same. The C Kα (0.275 KeV), O Kα (0.531 KeV), Si Kα (1.747 KeV), Cu lα1 (0.933 KeV), Cu kα1 (8.037 KeV) and Zn α1 and α2 around 1.0117 KeV, are observed in both spectra.[20] The relative intensities, however, are much greater for the solution with larger proportion of Cu(II). This is consistent with more metal coverage and with the SEM images of surfaces with metal deposited from Cu(II):Zn(II) containing solutions with a 10:1 ratio (6.4.B). The EDX results prove that both metals were deposited on diamond from their binary metal ion solutions.

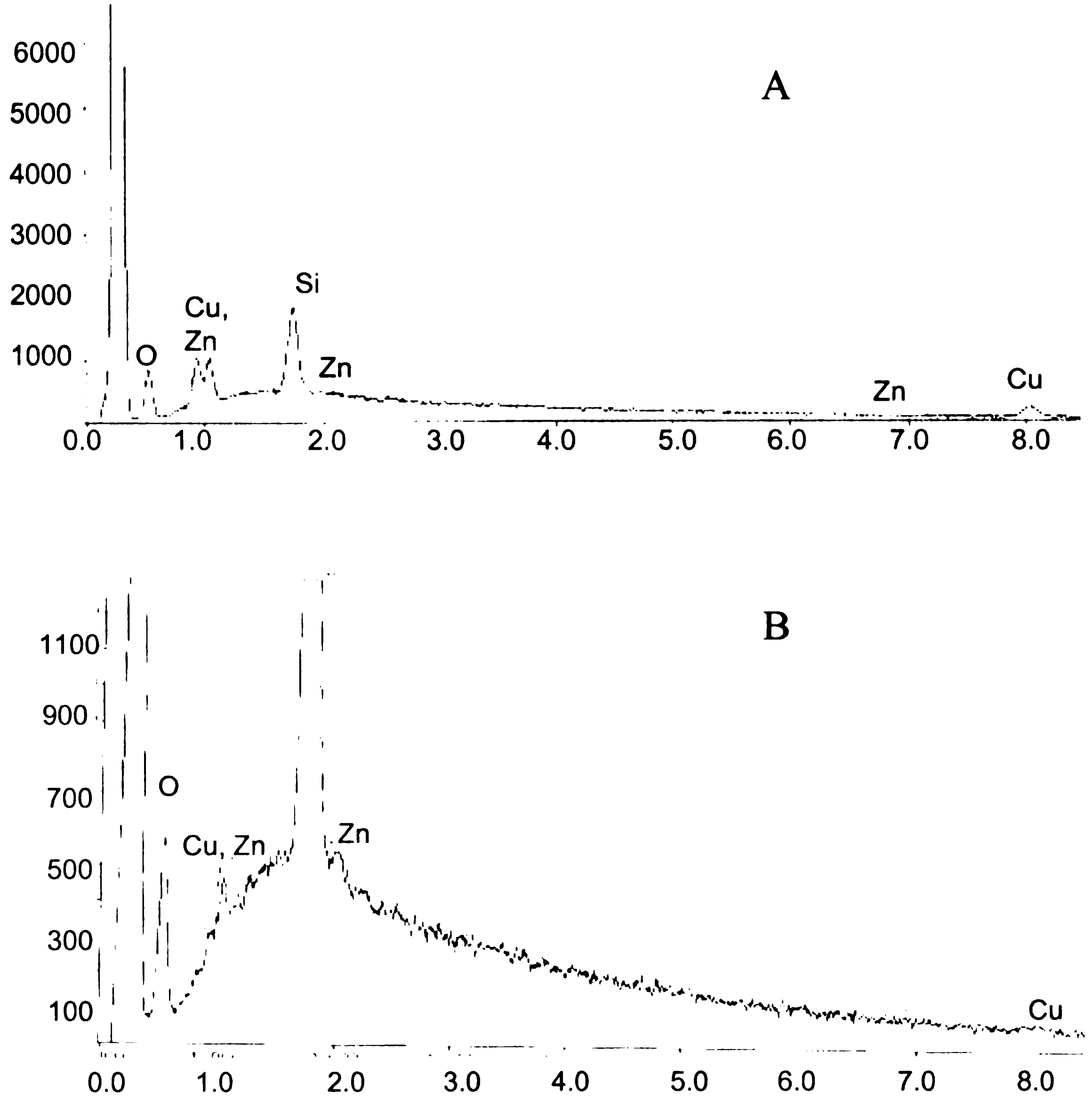

Figure 6.5 Energy dispersive x-ray analysis spectrum for Cu and or Zn deposited on microcrystalline diamond electrodes at -1300 mV for 3 min at metal ion concentrations of: (A) 100 ppm Cu(II) + 10 ppm Zn(II) and (B) 100 ppm Zn(II) + 10 ppm Cu(II).

6.3.3 Pulsed Galvanostatic Deposition

Figure 6.6 shows a comparison of the differential pulse voltammetric i-E curves for the stripping of metal phases deposits formed from 100 ppb Cu(II) in pH 5.2 acetate buffer using four different methods: (a) constant current deposition at 15 mA/cm^2 for 90s, (b) pulsed current deposition at 15 mA/cm^2 with 0.5 s pulses at a 50 % duty cycle for a total of 180s, (c) constant potential deposition at – 400 mV for 90s, and (d) pulsed potential deposition at - 400 mV with 0.5 s pulses at 50 % duty cycle for a total of 180 s. The charge passed during the galvanostatic deposition was kept constant at 0.3 C. The pulsed deposition parameters used in this comparison were found to be optimum as shown in the next section.

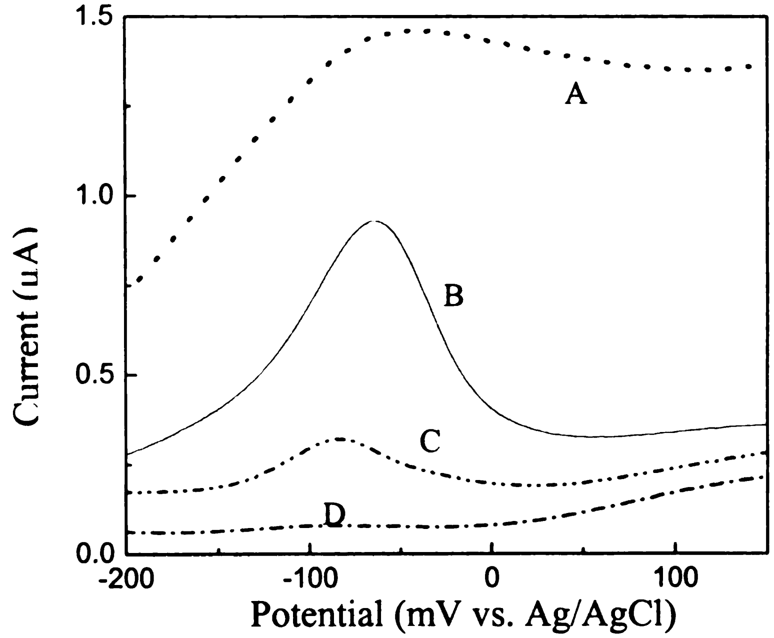

Figure 6.6 Differential pulse stripping voltammetric i-E curves for Cu on nanocrystalline diamond deposited at (A) constant current deposition at 15 mA/cm^2 for 90s, (B) pulsed current deposition at 15 mA/cm^2, 0.5 s pulses at a 50% duty cycle for a total time of 180 s, (C) constant potential step deposition at – 400 mV for 90s, and (D) pulsed potential deposition at - 400 mV with 0.5 s pulses at a 50% duty cycle for a total time of 180 s.

The two largest currents are seen for the metal deposits formed under galvanostatic conditions. This results from the fact that more charge is passed during the galvanostatic than the potentiostatic deposition. The most well defined and narrow peak is seen for the pulsed galvanostatic method. This is attributed to the formation of well dispersed metal deposits during the pulse sequence due to avoidance of inter-particle coupling.[23] This occurs because of the replenishment of the individual metal ion depletion layers around each of the growing metal particles during the pulse "off" stage. This prevents the metal centers from coalescing and forming large area deposit clusters. Pulsed electrodeposition approaches are known to offer advantages in terms of controlled particle size, stronger adhesion, more uniform electrodeposition etc.[24] Some of the particles are more closely spaced than the diffusion layer thickness, as evidenced by SEM given below. Therefore, hemispherical diffusion is maintained at some particles while semi-infinite linear diffusion occurs at other closely spaced particles and clusters. In a separate set of potential step experiments, the resultant charge passed during a potential step to -400 mV for 180 s was measured for 100 ppb Cu(II). The magnitude of the charge was 7.5×10^{-5} C. This is much less than the charge passed during the galvanostatic deposition and is the reason for the low signal intensities seen in Figures 6.6.C and D. The above results suggest that the use of pulsed current deposition is favorable for the DPASV detection of metals with diamond.

Optimization of Various Pulse Parameters. There are several parameters that can be varied to optimize the metal deposit: pulse current, pulse time, duty cycle and pulse number.

a) Optimization of the current density. Choi et al. found that the pulsed current deposition of Pt on carbon electrodes to be optimum at 25 mA/cm^2. At higher current densities, the performance dropped sharply because of the growth of dendritic crystals and the displacement of deposited metal particles due to hydrogen generation.[24] However, at lower current densities the nucleation and growth mechanism can be charge controlled where the growth of the already formed nuclei is preferred whereas at higher current densities the mechanism is likely mass transport controlled. It seems that an optimum applied current density would be a trade-off between obtaining a large metal loading on the electrode versus the other competing reactions like hydrogen evolution becoming dominant. Current densities ranging from 2 to 21 mA/cm^2 were used with a deposition time of 180 s and 1-s pulse length at a 50% duty cycle.

Natter and Hempelmann deposited Au from a commercial sulfite bath onto stainless steel and titanium electrodes, and tested current densities in the range from 50 to 500 mA/cm^2. They observed that the smallest crystallite size of 12 nm was formed at 50 mA/cm^2.[25] At higher current densities, powder formation occurred on the electrode surface. Figure 6.7 shows a few representative differential pulse stripping voltammetric i-E curves for Cu deposited by pulsed galvanostatic deposition at different current densities. The peak intensity initially increases with applied current density as expected, until the highest current density is reached 15 mA/cm^2, at which point the peak current decreases some. Analyses of the peak charge reveals that, the decrease in peak current may be due to the dislodging of metal deposits by hydrogen evolution reaction as gas bubbles were observed at the electrode surface at current densities higher than 15 mA/cm^2. The resultant electrode potential measured at the working electrode, at these current densities, was between –2.7 to –3.2 V versus an Ag/AgCl reference electrode. Dual peaks at ~ -100 and 100 mV are observed. These may be due to the oxidation of metal deposited at two different sites on the electrode surface. The current density of 15 mA/cm^2 (total charge passed: 0.3 C) was accepted as optimum based on the peak shape and intensity.

b) Optimization of duty cycle. The duty cycle is the percentage of the time the pulse is in the "on" state (t_{on}) relative to the total time that also includes a dead time. The duty cycle can be an important factor because the properties of metal deposits can be influenced by both the on-time, during which nuclei formation and growth occur, and the off-time or dead time, during which replenishment of the depletion layer around each particle(s) occurs.[26] Figure 6.8.A shows representative differential pulse stripping voltammetric i-E curves for the stripping of Cu from deposits formed as a function of the duty cycle. The deposition charge passed was kept constant at 0.3 C. The total time of deposition was 120 s (75 % duty cycle, 90 1-s pulses), 180 s (50 % duty cycle, 90 1-s pulses) and 360 s (25 % duty cycle, 90 1-s on pulses). As can be observed from Figures 6.8.A and 6.8.B, the peak parameter (current/FWHM) increases with decreasing duty cycle. The optimum duty cycle from the few tests was found to be 25 %; however 50 %

was used because the total analysis time for a 25 % duty cycle is 360 s and this is too long for practice.

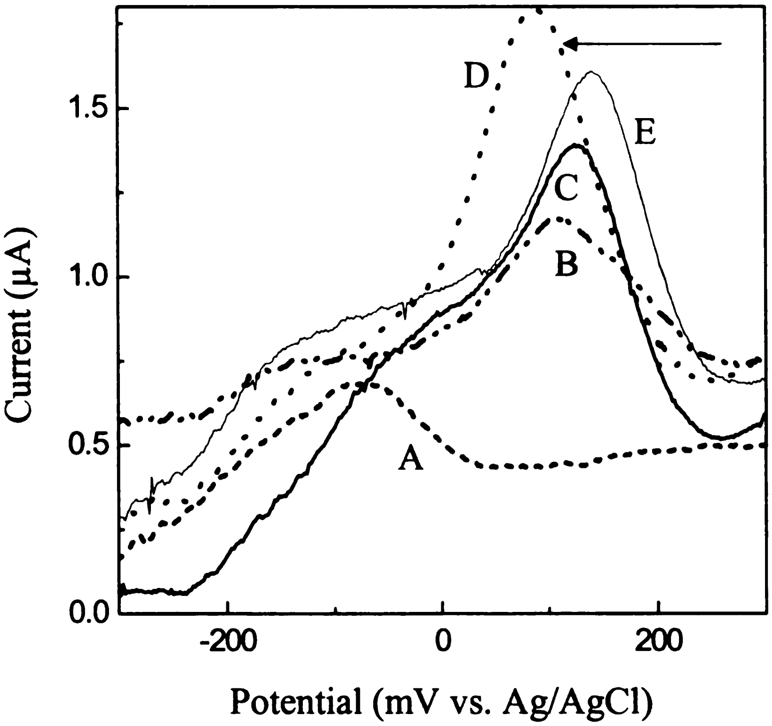

Figure 6.7 Differential pulse anodic stripping voltammetric i-E curves for Cu from a nanocrystalline diamond surface using pulsed galvanostatic deposition at (A) 2.7, (B) 5.5, (C) 12, (D) 15, and (E) 21 mA/cm^2. The solution was 100 ppb Cu(II) in 0.1 M acetate buffer, pH 5.2. Total deposition time = 180 s. Pulse width = 1 s. Duty cycle = 50%. Arrow indicates the optimum current density.

According to Natter and Hempelmann, for a constant t_{on}-time and current density, the crystallite size increases for long t_{off}-times due to Ostwald ripening.[25] Ostwald ripening is a spontaneous process that is said to be occurring when initially formed smaller crystals in a system merge to form larger crystals. This happens because larger crystals are more energetically favored than smaller crystals.

This is contrary to what we infer from the voltammetric curves. They were found to be the broadest for lowest t_{off} (75 %) duty cycle, consistent with large particle sizes. A reason for this disagreement could be that Natter and Hempelmann tested the variance of t_{off} in the milli-second regime. The variation of the electrode potential during the current pulse leads to a non-faradaic current due to the charging of the double layer, so that only a part of the overall applied current is involved in the electrochemical reaction.[16] The charging of the double layer is typically in the milli-second regime. It is possible that the duration of pulses in their experiments were too short for the bulk of the applied current to be used for metal deposition.

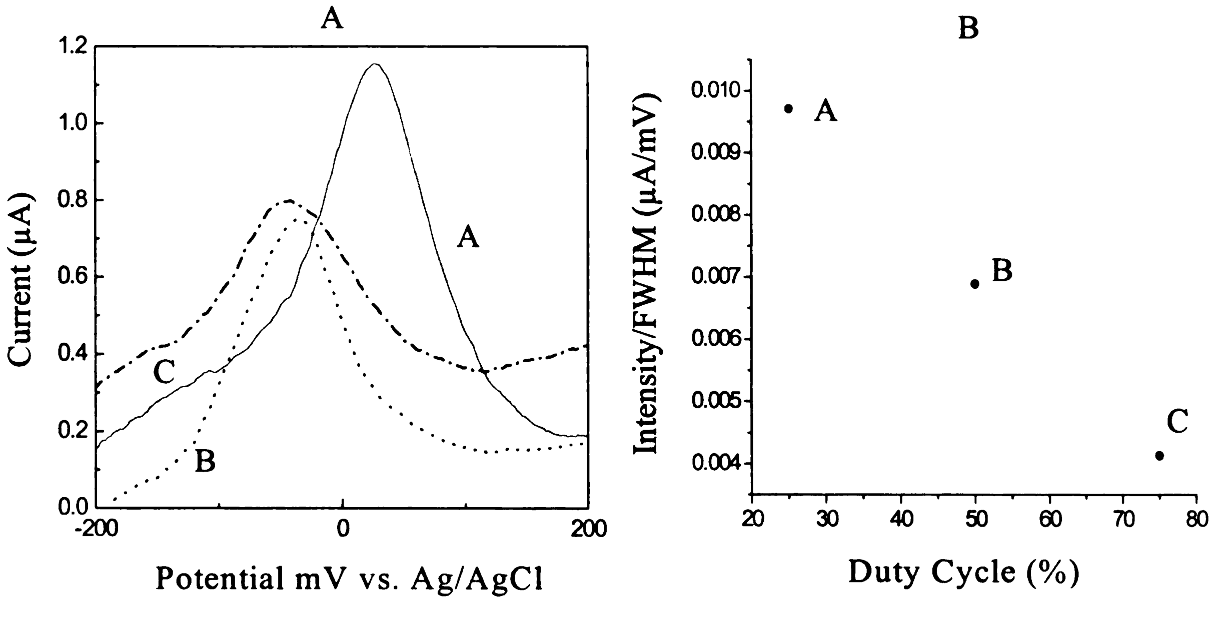

Figure 6.8 Differential pulse anodic stripping voltammetric i-E curves for Cu from a nanocrystalline diamond surface using pulsed galvanostatic deposition at effective deposition times of (A) 360s (25 % duty cycle, 90, 1-s on pulses), (B) 180s (50 % duty, 90, 1-s on pulses), and (C) 120s (75 % duty, 90, 1-s on pulses). The solution was 100 ppb Cu(II) in 0.1 M acetate buffer, pH 5.2. Current density = 15 mA/cm^2.

c) Optimization of pulse width. Figure 6.9 shows representative differential pulse stripping voltammetric i-E curves for Cu from a nanocrystalline diamond surface as a function of the pulse width (t_{on}). The total galvanostatic charge passed was kept constant at 0.3 C. The pulse widths tested were: (A) 3.0, (B) 1.5, (C) 1.0, (D) 0.5, (E) 0.25, and (F) 0.1 s. The plot of peak current/FWHM (μA/mV) vs. the pulse width shows that at 0.5 s pulse width, this ratio is a maximum. The peak current/FWHM (μA/mV) parameter was chosen as an indicator of peak shape. Intense narrow voltammetric peaks are desired as this could enable (i) quantitation using peak currents rather than peak charge, and (ii) the simultaneous assay of metal ions having relatively close $E^{o'}$ values.

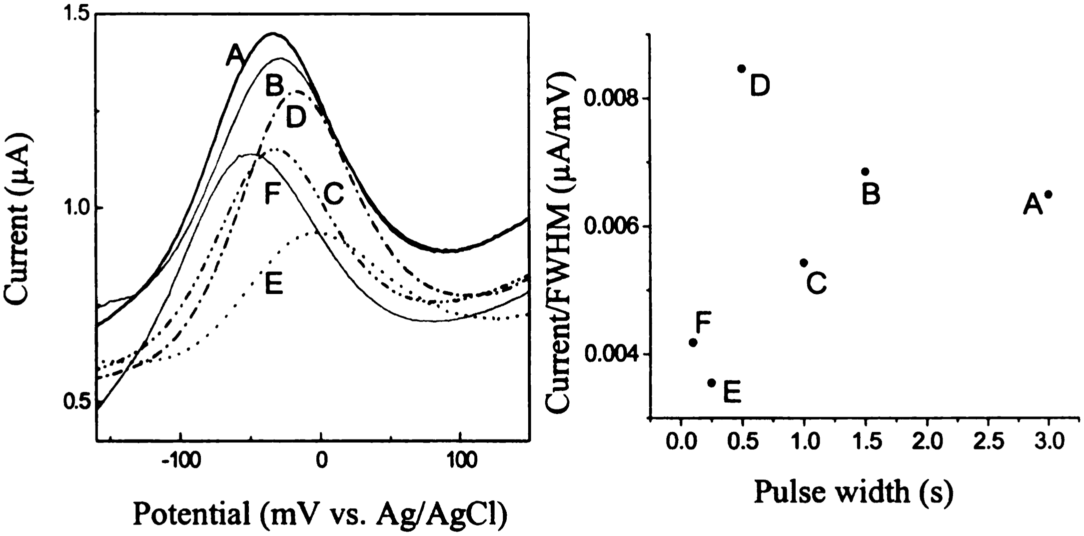

Figure 6.9 Differential pulse anodic stripping voltammetric i-E curves for Cu from a nanocrystalline diamond surface using pulsed galvanostatic deposition at pulse widths of (A) 1.5, (B) 3, (C) 0.5, (D) 1.0, (E) 0.1, and (F) 0.25 s. The solution was 100 ppb Cu(II) in 0.1 M acetate buffer, pH 5.2. Current density = 15 mA/cm^2. Duty cycle = 50%. Total deposition time = 180 s.

Scanning Electron Micrographs of Cu Deposits on Nanocrystalline Diamond. Scanning electron micrographs of Cu deposited from a 10 ppm solution of Cu(II) in 0.1 M acetate buffer, pH 5.2, at 15 mA/cm^2 using both the constant and pulsed conditions are presented. The deposition charge passed was constant at 0.3 C. The films used were acid-washed and rehydrogenated boron-doped nanocrystalline diamond thin-films. Figure 6.10 shows the back-scattered electron images for (A) a 90 s constant current deposition and (B) pulsed current deposition using 0.5 s pulses for 180 s (180 pulses). Analysis of the Cu deposits on at least two nanocrystalline films at four different spots each film for each set of deposition conditions revealed mean particle diameters of 109 ± 87 nm and 34 ± 60 nm, respectively, for the constant and pulsed current deposition. The particle density was 1.5×10^9 and 1.1×10^{10} cm^{-2}, respectively, for the constant current and pulsed deposition conditions.

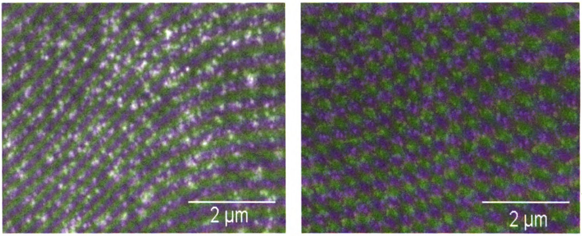

Figure 6.10 Scanning electron micrographs (back scattered images) of Cu deposited on nanocrystalline diamond at 15 mA/cm^2 in the form of a (A) constant current applied for 90 s and (B) a pulsed current applied for 180 s using 0.5 s pulse width. Other conditions have been provided in the experimental section.

The fractional surface coverage is 0.1386 and 0.1058 respectively, for the constant current and pulsed deposition conditions. These data show that in comparison to the constant current deposition, the pulsed deposition yields well dispersed particles of smaller nominal diameter and lower metal surface coverage. Although, the particle size deviation was large using both the deposition protocols, it was larger for the constant current approach.

Analytical Detection Studies. Studies were performed to determine if there was a concentration dependence on the response for Cu(II) using the pulse galvanostatic deposition method. Figure 6.11.A depicts background-subtracted differential pulse stripping voltammetric i-E curves for deposits from Cu(II) solutions of increasing concentrations ranging from 1 to 1000 ppb. The peak current and charge increase with increasing solution concentration. The E_p^{ox} shifts positive with increasing solution concentration due to the greater surface coverage. The baseline peak widths are ca. 150 mV and the FWHM values are ca. 75 mV. Figure 6.11.B shows a plot of peak charge vs. the Cu(II) concentration. The S/N for the 1 ppb run is 10/1.

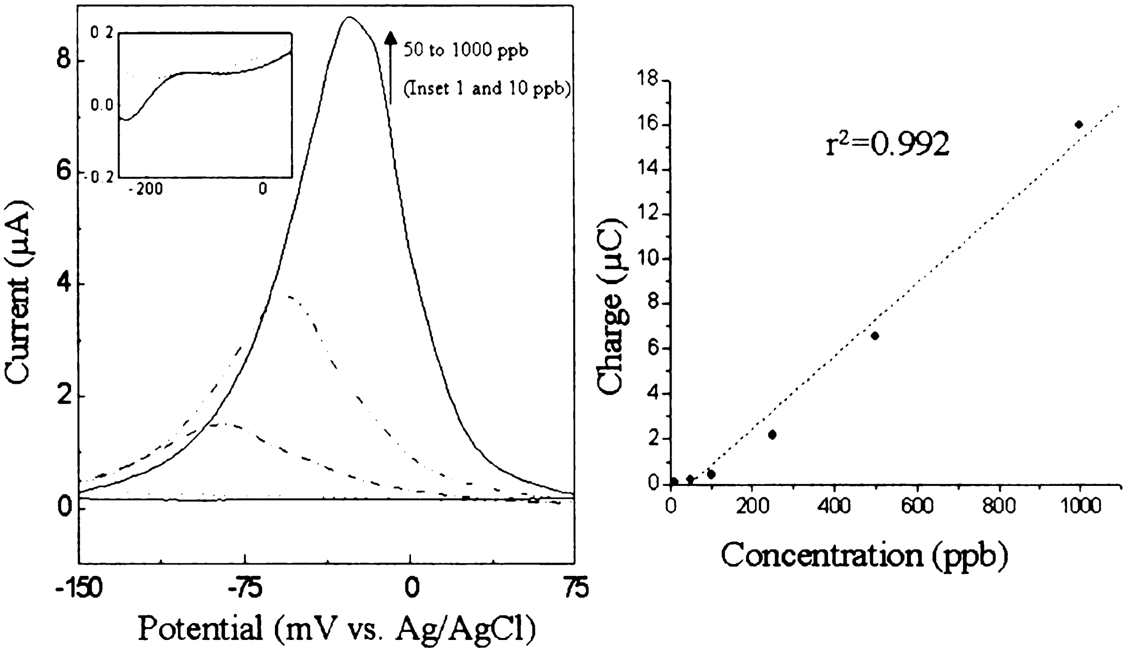

Figure 6.11 (A) Background-subtracted differential pulse stripping voltammetric i-E curves for metal deposits formed from 50, 100, 250, 500 and 1000 ppb of Cu(II) solution in 0.1 M acetate buffer, pH 5.2. The inset shows the stripping voltammetric i-E curves for the 1 ppb (dashed line) and 10 ppb Cu(II) solutions.(B) Plot of charge vs. concentration for the data in 6.11.A. The integration range was 100 mV (potential limits for integration varied with concentration).

Comparison of Cu-Zn Voltammetric i-E Curves for Pulsed Constant Current and Constant Potential Deposition Methods. Figure 6.12 shows a comparison of representative background-subtracted differential pulse anodic stripping voltammetric i-E curves for 100 ppb Cu(II) and 100 ppb Zn(II) in pH 5.2 acetate buffer recorded from -1200 mV to 200 mV. Curve 6.12.A. was recorded for metal phase formation using pulsed current deposition of both Cu(II) and Zn(II) at 15 mA/cm^2 with a 0.5 s pulse width and a 50 % duty cycle for a total time of 180 s, while curve 6.12.B was recorded for metal phase formation at constant potential at - 1200 mV for 90 s.

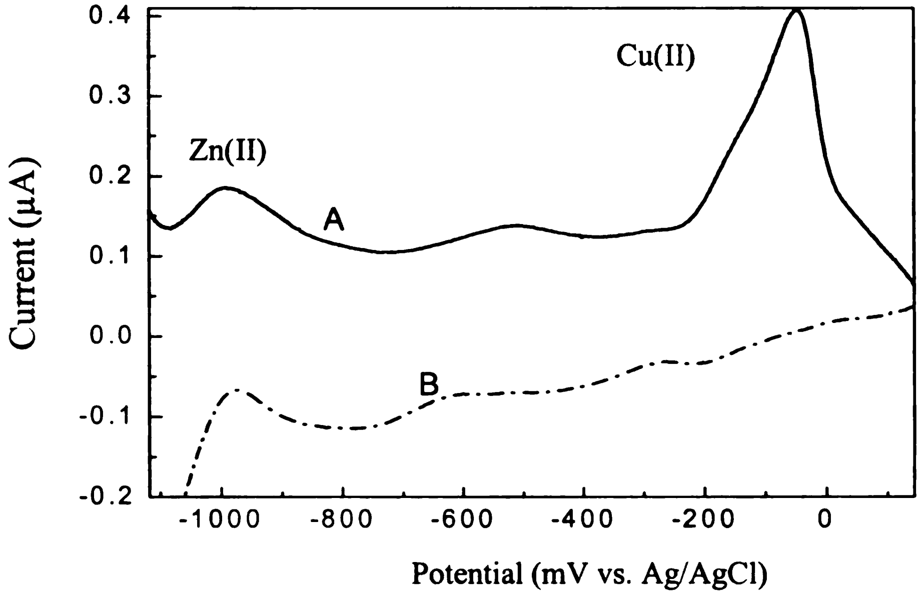

Figure 6.12 Comparison of representative background subtracted differential pulse anodic voltammetric i-E curves for 100 ppb Cu(II) and 100 ppb Zn(II) in 0.1 M acetate buffer, pH 5.2. Preconcentration was performed by (A) pulsed current deposition at 15 mA/cm^2 with a 0.5 s pulse width and a 50% duty cycle and a total time of deposition of 180 s, and (B) constant potential deposition at - 1200 mV for 90 s.

Discernible peaks for Cu (-90 mV) and Zn (-1000 mV) are observed for the pulsed current deposition. In contrast, only a weak Zn peak is seen and the curve is shifted below the zero line for the constant potential deposition. This could be attributed to the difference in charge for the hydrogen evolution reaction on the bare electrode versus the electrode containing metal deposits. During the potential scan in regions cathodic of ~ -1 V, a significant amount of charge is passed due to hydrogen evolution reaction. These results indicate that small amounts of metal were deposited even at 90 s effective time of application of constant potential in pH 5.2 acetate buffer, however the amount of metal deposited by galvanostatic deposition for the same effective times was much higher.

6.3.4 Observation of Voltammetric i-E curves of Narrow FWHM

The DPASV procedure used a "cleaning step" in between runs. This step typically involved poising the working electrode at + 0.6 V for 3 min with the N_2 line placed in close proximity. The N_2 purge aid in the solution mixing of metal ions from the vicinity of the electrode. An unusual observation was occasionally made when solutions were not purged with N_2 in between runs during the "cleaning" step. Figure 6.13 shows voltammetric i-E curves recorded for a (A) 100 ppb solutions of Ag(I) and (B) 100 ppb solution of Cd(II), both in 0.1 M acetate buffer, pH 4.5 (with added 30 ppm Ca(II) and 5 ppm Mg(II) salts). In all cases, an N_2 purge was not performed during any of the procedural steps.

The voltammetric i-E curves (solid lines) were first recorded after deposition of the metal ions for 3.5 min at 0 and – 1 V for Ag and Cd respectively. The cell potential was then poised at 0.6 V for 3 min and the deposition and stripping steps repeated and the voltammetric i-E curves (dashed lines) recorded. It was observed that the Ag peak shifted negative by about 20 mV and became narrow (FWHM ~ 20 mV) and relatively intense. A similar observation was made for Cd, as the peak shifted negative by about 150 mV and also became narrow (FWHM ~ 45 mV) and relatively intense. The intense narrow peaks persisted in subsequent scans. The total area was greater in both cases for the second run (dashed lines).

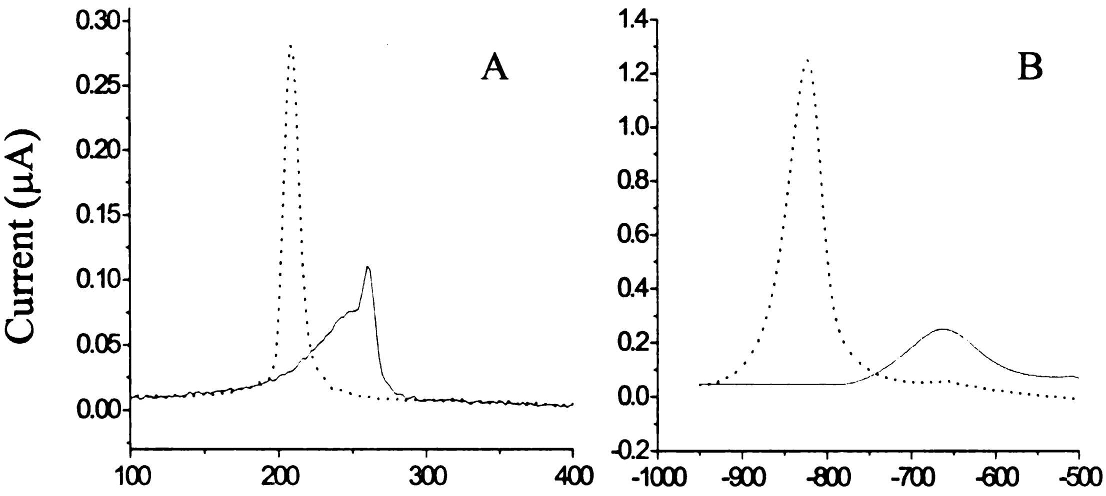

Figure 6.13 Background-subtracted stripping voltammetric i-E curves recorded for (A) 100 ppb Ag(I) and (B) 100 ppb Cd(II) in 0.1 M acetate buffer, pH 5.2 (with added 30 ppm Ca(II) and 5 ppm Mg(II) salts). The solid lines depict the first recorded i-E curves and the dashed lines depict subsequent i-E curves (no purging with N_2 undertaken).

These results suggest that incomplete removal of the remnant metal deposits takes place when the solution is not purged with a gas in between runs. The fact that the peaks moved negative and became intense could be explained by the fact that when there were favorable sites in the form of remnant metal already present on the diamond surface, the new metal phase formation would take place on these sites. The oxidation of metal from these sites would require less driving force or overpotential and would also take place with a more uniform rate than oxidation from the relatively heterogeneous diamond surface, making the peaks appear intense. It is possible that more metal gets deposited on the remnant metal centers due to faster charge transfer and or radial flux of depositing species. This would explain the greater charge under the voltammetric i-E curves (dashed lines). From chronocoulometric measurements (Chapter 3), the typical ratio of the Q_p^{ox}/Q_p^{red} for the metal oxidation and deposition was found to be in the range of 0.65-0.75 for Ag(I) on diamond. This indicated that all the deposited metal is not oxidized.

The above theory was strengthened by the fact that previous electrode response (denoted by solid lines in Figure 6.13) could be regained by bubbling with N_2 and that a background voltammetric i-E curve recorded after the "cleaning" step without the N_2 purge showed an oxidation peak for the metal ion. The same effect was observed when purging with O_2 instead of N_2, proving that the observed response may not necessarily be due to the nature of the gas. Recent results from our laboratory have also shown that dissolved O_2 does not affect the stripping voltammetric response for Ag(I).

Another approach to explaining the observation could be to model the metal phase formation chemistry on diamond surfaces. The Nernst equation dictates the position of the peak potential, E_p. Changes in surface chemistry of diamond (e.g., surface oxygen content) can decrease the concentration of the adsorbed ad-atom. This would shift the observed E_p negative. Although these results are preliminary, they could open the door for a new method of obtaining narrower peaks in ASV. Experimental conditions for reproducibly obtaining the intense narrow ASV peaks observed above need further study. If the first explanation is valid, metals with positive $E^{o'}$ such as Pt, Pd or Au could be plated onto diamond prior to its use for assaying for metal ions for obtaining narrower stripping peaks.

6.4 Conclusions

The electroreduction of the metal ions via potential step deposition produces considerable nucleation and growth of metal deposits. This approach, however, led to peak broadening, multiple peaks, suppression of peaks etc. during the electrooxidation step because the deposition process was not controlled. The experiments conducted by co-depositing the metal ions provided valuable insight into the complexity of this problem and the possibility of interference by intermetallic complex formation between them. It was observed that Cu(II) and Zn(II) significantly affected the voltammetric response for the other. It is possible that Cu-Zn intermetallic complexes are formed on diamond.

Scanning electron micrographs of the Cu and Zn deposits demonstrated that the morphology of the deposits formed when the metals were simultaneously deposited is different from the morphology of the individually deposited metals. The energy dispersive x-ray spectra of the deposits showed that both Cu and Zn are deposited from their mixtures. The difference in morphology could be due to the formation of a complex between the metals or deposits of Zn forming on the already formed deposits of Cu.

Pulsed galvanostatic deposition lead to highly dispersed Cu deposits of a small nominal diameter. It is felt that with the further optimization of experimental conditions this approach could be useful for producing sharp and narrow stripping voltammetric peaks. Results presented in this Chapter indicated that constant current pulsed deposition of metal ions was useful in increasing the S/N ratio and improving peak shape, even at effective deposition times of only 90 s. Discernible peaks for 100 ppb Cu(II) and Zn(II) were observed after their pulsed current deposition for 90 s, whereas potentiostatic deposition did not yield such peaks after 90 s deposition time.

A shifting of the voltammetric peaks to negative potentials and improved peak shapes was observed occasionally, speculated to be caused by remnant metal on the surface of the diamond. It might be worthwhile to explore this phenomemon further.

6.5 References

(1) Eckerlin, P.; Kandler, H., Eds. *Structure Data of Elements and Intermetallic Phases (Landolt-Boernstein Numerical Data and Functional Relations in Science and Technology, Group III: Crystal and Solid-State Physics, Vol. 6)*, 1971

(2) Wang, J., Ed. *Stripping Analysis: Principles, Instrumentation, and Applications*; VCH Publishers, Inc., 1985

(3) Wise, J. A.; Roston, D. A.; Heineman, W. R. *Analytica Chimica Acta* **1983,** *154*, 95-104.

(4) Copeland, T. R.; Osteryoung, R. A.; Skogerboe, R. K. *Analytical Chemistry* **1974,** *46*, 2093-2097.

(5) Lastres, E.; De Armas, G.; Catasus, M.; Alpizar, J.; Garcia, L.; Cerda, V. *Electroanalysis* **1997,** *9*, 251-254.

(6) Lau, O.-W.; Cheng, O.-M. *Analytica Chimica Acta* **1998,** *376*, 197-207.

(7) Marques, A. L. B.; Chierice, G. O. *Talanta* **1991,** *38*, 735-739.

(8) Piccardi, G.; Udisti, R. *Analytica Chimica Acta* **1987,** *202*, 151-157.

(9) Scollary, G. R.; Cardwell, T. J.; Cattrall, R. W.; Nan, C. G.; Vicente-Beckett, V. A.; Hamilton, I. C.; Roden, S. *Electroanalysis* **1993,** *5*, 685-689.

(10) Stromberg, A. G.; Gorodovykh, V. E. *Zhurnal Neorganicheskoi Khimii* **1963,** *8*, 2355-2359.

(11) Roston, D. A.; Brooks, E. E.; Heineman, W. R. *Analytical Chemistry* **1979,** *51*, 1728-1732.

(12) Bennett, J. A.; Show, Y.; Swain, G. M. *In preparation, Journal of the Electrochemical Society* **2004.**

(13) Gunawardena, G.; Hills, G.; Montenegro, I.; Scharifker, B. *Journal of Electroanalytical Chemistry and Interfacial Electrochemistry* **1982**, *138*, 225-239.

(14) Granger, M. C.; Xu, J.; Strojek, J. W.; Swain, G. M. *Analytica Chimica Acta* **1999**, *397*, 145-161.

(15) Show, Y.; Witek, M. A.; Sonthalia, P.; Swain, G. M. *Chemistry of Materials* **2003**, *15*, 879-888.

(16) Coutanceau, C.; Rakotondrainibe, A. F.; Lima, A.; Garnier, E.; Pronier, S.; Leger, J. M.; Lamy, C. *Journal of Applied Electrochemistry* **2004**, *34*, 61-66.

(17) Shuman, M. S.; Woodward, G. P., Jr. *Analytical Chemistry* **1976**, *48*, 1979-1983.

(18) Behzadian, B.; Piron, D. L.; Fan, C.; Lessard, J. *International Journal of Hydrogen Energy* **1991**, *16*, 791-796.

(19) Gerlach, R. W.; Kowalski, B. R.; Lab. Chemometrics,Univ. Washington,Seattle,WA,USA. :, 1981, pp 23 pp.

(20) Kolb, D. M.; Przasnyski, M.; Gerischer, H. *Journal of Electroanalytical Chemistry and Interfacial Electrochemistry* **1974**, *54*, 25-38.

(21) Brainina, K.; Neyman, E., Eds. *Electroanalytical stripping methods*; John Wiley and Sons, 1993

(22) Brett, C. M. A.; Beatriz Quinaz Garcia, M.; Lima, J. L. F. C. *Analytica Chimica Acta* **1997**, *339*, 167-172.

(23) Liu, H.; Penner, R. M. *Journal of Physical Chemistry B* **2000**, *104*, 9131-9139.

(24) Choi, K. H.; Kim, H. S.; Lee, T. H. *Journal of Power Sources* **1998**, *75*, 230-235.

(25) Natter, H.; Hempelmann, R. *Electrochimica Acta* **2003**, *49*, 51-61.

(26) Ibl, N. *Surface Technology* **1980**, *10*, 81-104.

CHAPTER 7

SUMMARY

The answers to several research questions were sought at the outset of this effort. The first answer sought was the viability of using boron-doped diamond as an electrode material for trace metal ion analysis using DPASV. As mentioned, this new electrode material has very favorable attributes for this electroanalytical application, that include a large working potential window, a chemically inert surface and electrical conductivity. Data presented in this dissertation reveals that diamond electrodes are useful for the trace analysis of dissolved metal ions. Diamond electrodes yielded favorable analytical detection figures of merit for five priority metal ions with very low limits of detection, and a stable and accurate response. The electrode surface could be regained by a simple oxidation procedure and the electrodes were used for months at a time with no response degradation. The analytical performance of diamond compared well with the historically-used Hg thin-film electrode and was better than that for the commonly-used GC electrode.

The performance of two morphologically and microstructurally different diamond electrodes was compared. Both types of diamond showed very favorable analytical detection figures of merit, although the nanocrystalline film had a slight edge in terms of sensitivity and limit of detection for some metal ions. This observation is due to the increased particle density (i.e., increased metal phase formation) and smaller particle diameter during the preconcentration or deposition step. This could be both due to the smaller feature size, and the fact that a larger fraction of the surface, compared to the microcrystalline diamond, was electrically conducting (i.e., electrochemically active). The results obtained with the nanocrystalline diamond and DPASV compared favorably with results from other more established methods, such as AAS and or ICP-MS. The method was applied to the analysis of several types of contaminated samples.

An understanding of the metal nucleation and growth phenomenon on diamond is important for determining of the optimum experimental parameters for preconcentration in the DPASV method. For instance, when using solid electrodes for ASV, like diamond, one ideally desires a high distribution of metal particles with a small and uniform particle size. This should lead to more narrow and intense oxidation or stripping peaks. Therefore, conditions under which an instantaneous nucleation and growth of the metal deposits occur should be selected. As discussed in Chapters 5 and 6, the stripping peaks for Cu, and the other metals, were observed to be rather broad. This is presumably due to the fact that, at least for Cu, metal phase formation on diamond occurs via a progressive nucleation and growth mechanism. Results from cyclic voltammetric, chronoamperometric and EC-AFM measurements presented in Chapter 3 demonstrated the utility of these methods for both the quantitative and qualitative study of the mechanisms governing metal phase formation on diamond. Further, the experimental data revealed that the deposition of metal phases on boron-doped diamond electrodes occurs by the Volmer-Weber growth mode. No underpotential deposition of metal was observed indicating a weak metal phase-substrate interaction.

The quality of the DPASV measurement could be improved if the relatively large peak widths seen in most of our presented data were reduced. In Chapter 6 we demonstrated the use of pulsed galvanostatic deposition to produce Cu deposits that were nominally smaller in size and more uniformly dispersed over the diamond surface than was achieved using constant potential or constant current deposition. Resultant stripping voltammetric i-E curves indicated that the constant current pulsed deposition of metal ions was useful in increasing the S/N ratio and improving peak shape, even at effective deposition times of only 90 s.

Intermetallic compound formation can be a complicating factor in ASV. When an intermetallic compound forms, the stripping peaks for the constituent metals can be attenuated, shifted or enhanced. Some of the more common intermetallics are Ag-Cd, Ag-Zn, Cu-Cd, and Cu-Zn. From results presented in Chapter 6, intermetallic compound formation on diamond was found to be problematic in the simultaneous assay of Cu(II) and Zn(II). It was further shown that the selectivity, and the peak shape and intensity could be improved through the use of pulsed galvanostatic deposition rather than the conventional constant potential deposition for this measurement.